

Virtual and Physical Prototyping

ISSN: 1745-2759 (Print) 1745-2767 (Online) Journal homepage: www.tandfonline.com/journals/nvpp20

Hybrid manufacturing and mechanics of architected interpenetrating phase composites: review and perspectives

Qinze Song, Agyapal Singh & Nikolaos Karathanasopoulos

To cite this article: Qinze Song, Agyapal Singh & Nikolaos Karathanasopoulos (2025) Hybrid manufacturing and mechanics of architected interpenetrating phase composites: review and perspectives, *Virtual and Physical Prototyping*, 20:1, e2505992, DOI: [10.1080/17452759.2025.2505992](https://doi.org/10.1080/17452759.2025.2505992)

To link to this article: <https://doi.org/10.1080/17452759.2025.2505992>



© 2025 The Author(s). Published by Informa UK Limited, trading as Taylor & Francis Group



Published online: 26 May 2025.



Submit your article to this journal 



Article views: 948



View related articles 



View Crossmark data 

Hybrid manufacturing and mechanics of architected interpenetrating phase composites: review and perspectives

Qinze Song^{a,b}, Agyapal Singh^a and Nikolaos Karathanasopoulos^{a,b}

^aDepartment of Engineering, New York University Abu Dhabi, Abu Dhabi, UAE; ^bDepartment of Mechanical and Aerospace Engineering, New York University, Tandon School of Engineering, Brooklyn, NY, USA

ABSTRACT

Characterized by their unique topological and mechanical metrics, interpenetrating phase composites (IPCs) have emerged as a versatile class of materials with advanced performance, garnering significant interest across academia and industry. This work comprehensively investigates the manufacturing methods and mechanical properties of IPCs, with a focus on metal-metal, ceramic-metal, polymer-metal, and polymer-ceramic architected interpenetrating phase designs. The state-of-the-art hybrid techniques typically employed in their manufacturing are critically examined—including additive manufacturing, casting, electrodeposition, and dealloying processes—highlighting their similarities, novelties, and limitations associated with each co-continuous composite class. A large body of experimental data is collected and comparatively analysed, summarising primal physical metrics. The inner design is associated with the arising effective mechanical performance, comparatively quantifying Young's moduli, yield and ultimate strengths, critical densification or fracture strains, and specific energy absorptions. The extended datasets form the basis for the creation of comprehensive Ashby plot representations of the aforementioned performance metrics, offering unique insights into their mechanical performance. As such, this work provides a foundational understanding of the IPC manufacturing processes and resulting mechanics, identifying gaps in current knowledge and suggesting avenues for future exploration in this rapidly evolving field.

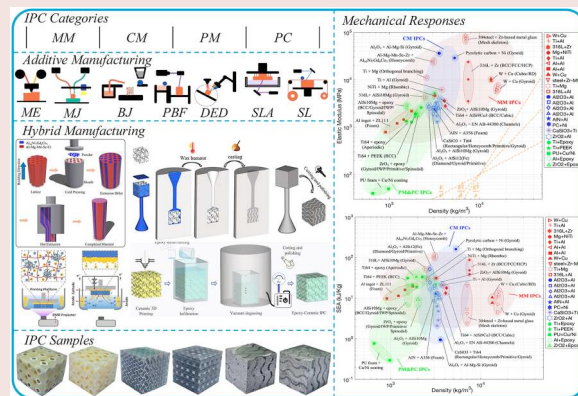
ARTICLE HISTORY

Received 14 March 2025

Accepted 5 May 2025

KEYWORDS

Additive manufacturing; hybrid methods; architected materials; IPCs; mechanical properties; strength; specific energy absorption



Nomenclature and abbreviations

Abbr.	Definition	FCC	Face-Centred Cubic
AM	Additive Manufacturing	HCP	Hexagonal Close-Packed
IPC	Interpenetrating Phase Composite	OB	Orthogonal Branching
TPMS	Triply Periodic Minimal Surface	ME or MEX	Material Extrusion
IWP	I-graph and wrapped package-graph	MJ or MJT	Material Jetting
RD	Rhombic Dodecahedron	BJ or BJT	Binder Jetting
BCC	Body-Centred Cubic	PBF	Powder Bed Fusion
		SLS	Selective Laser Sintering

CONTACT Nikolaos Karathanasopoulos n.karathanasopoulos@nyu.edu Department of Mechanical and Aerospace Engineering, New York University, Tandon School of Engineering, Brooklyn, NY 11201, USA

© 2025 The Author(s). Published by Informa UK Limited, trading as Taylor & Francis Group

This is an Open Access article distributed under the terms of the Creative Commons Attribution-NonCommercial License (<http://creativecommons.org/licenses/by-nc/4.0/>), which permits unrestricted non-commercial use, distribution, and reproduction in any medium, provided the original work is properly cited. The terms on which this article has been published allow the posting of the Accepted Manuscript in a repository by the author(s) or with their consent.

SLM	Selective Laser Melting
EBM	Electron Beam Melting
DED	Direct Energy Deposition
VP or VPP	Vat Photopolymerization
SLA	Stereolithography Appearance
SL or SHL	Sheet Lamination
M	Metal
C	Ceramic
P	polymer
MM	Metal-Metal
CM	Ceramic-Metal
PM	Polymer-Metal
PC	Polymer-Ceramic
ROM	Rule of Mixture
AF	Aluminum Foam
PU	Polyurethane
PEEK	Polyetheretherketone
316L	Stainless Steel 316L
NiTi	Nitinol
Cu	Copper
W	Tungsten
Mg	Magnesium
Ni	Nickel
MG	Metal Glass
S-S Curve	Stress-Strain Curve
UCS	Ultimate Compressive Strength
YS	Yield Strength
E	Elastic Modulus
EA	Energy Absorption
SEA	Specific Energy Absorption
σ_{ys}	Yield Strength (In Plot)
$\sigma_{0.2}$	0.2% Yield Strength
σ_u	Ultimate Compressive Strength (In Plot)
σ_f	Fracture Strength
ϵ_u	Strain at Ultimate Compressive Strength
ϵ_d	Strain at Densification Region
ϵ_f	Fracture Strain

1. Introduction

Humanity has a long history of exploring and expanding the possibilities of material utilisation, dating back to the earliest civilisations. Initially, bulk materials were machined and employed, primarily gaining their properties out of their chemical composition [1]. However, with the recent advancements in Additive Manufacturing (AM) [2], material properties appeared as a result of intentional inner structural design. This marked the emergence of state-of-the-art architected materials, whose properties can be designed through the tailoring of their inner architecture [3–5]. Under the broad category of architected materials, one of the most significant classes is the one of metamaterials, engineered to

exhibit outstanding properties not typically found in nature [3,4,6,7].

The concept of metamaterials was first reported in the 1960s by Viktor Veselago [8], exploring materials with a negative refractive index (NRI). His work laid the foundation of metamaterials, suggesting that materials engineered with specific structural designs could exhibit extraordinary behaviours. Based on their applications, metamaterials can be categorised into 4 major types: electromagnetic, acoustic, thermal, and mechanical metamaterials [7,9]. Among these, mechanical metamaterials are specifically engineered structures designed to achieve unique mechanical properties, including negative Poisson's ratio [10,11], high stiffness-to-weight ratio [12,13], vanishing shear modulus [14], properties that arise primarily from their internal geometries, rather than the specific material attributes from which they are made [15,16]. More recently, aperiodic configurations have been introduced as a new class of architected geometries that avoid translational symmetry while remaining fully space-filling. For instance, inspired by the so-called Einstein tile, these modified structures employ deterministic, non-repeating arrangements of a single unit cell to achieve highly uniform stress distributions and enhanced damage tolerance under load. Unlike stochastic or periodic designs, aperiodic microlattices offer customisable global behaviour through local geometric diversity, making them particularly attractive for mechanical metamaterials.

In this context, several novel topologies have been developed [17]. Examples of commonly observed structures are illustrated in Figure 1-Design. Strut-based structures such as Octet and Kelvin truss architectures are formed as a network of interconnected beams [25], providing high stiffness and strength [26,27]. Triply Periodic Minimal Surfaces (TPMS) form another broad class of periodic structures. Characteristic examples constitute the Schwarz P (Primitive), Schwarz D (Diamond), Schwarz H (hexagonal), I-Wrapped Package (IWP), and Gyroid surface topologies [28]. Beyond periodically ordered patterns, stochastic and spinodal surface topologies have been developed, the latter arising from the spatial separation of phases characterised by the Cahn-Hilliard equation [29] and defined by Gaussian random fields for simplified and practical control [30,31]. More recently, aperiodic configurations have been introduced as a new class of architected geometries that avoid translational symmetry while remaining fully space-filling. For instance, inspired by the so-called Einstein tile, these structures employ deterministic, non-repeating arrangements of a single unit cell to achieve highly uniform stress distributions and enhanced damage tolerance under load

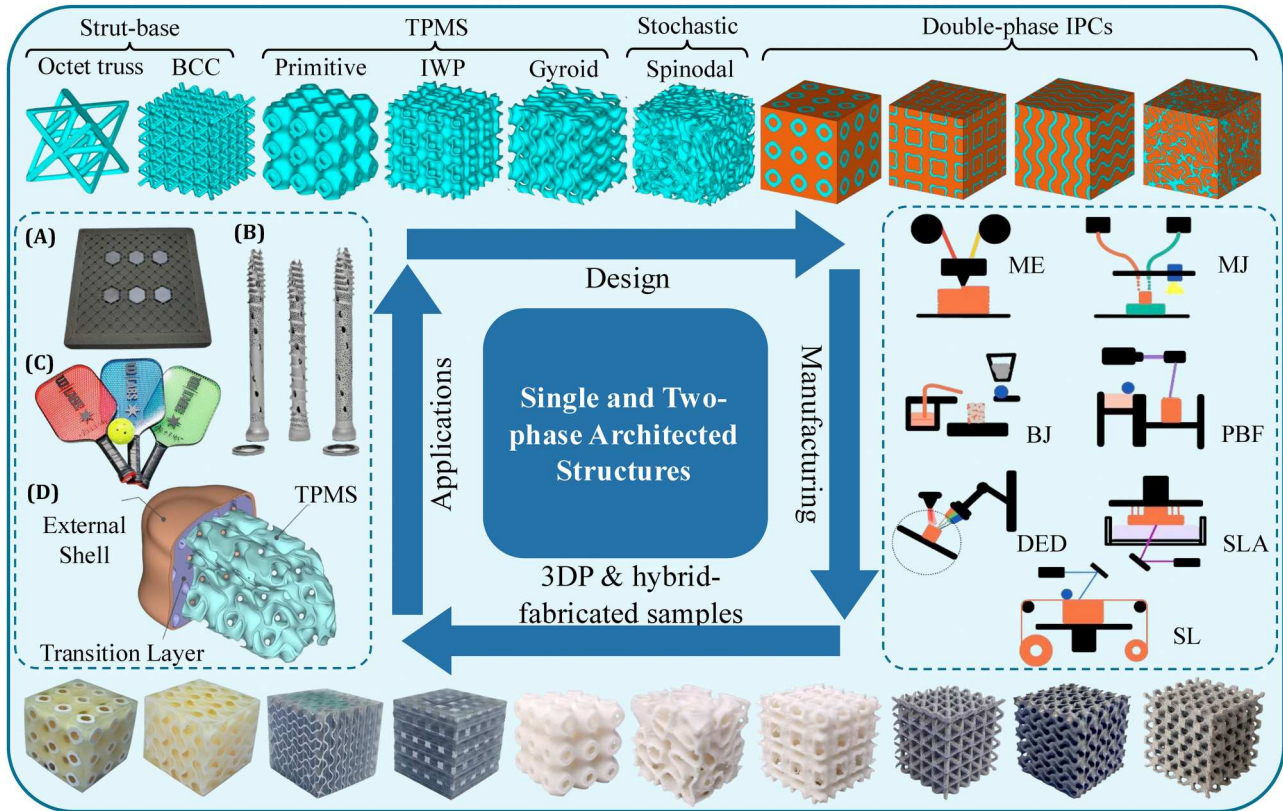


Figure 1. The design of topology, manufacturing, manufactured samples and application of architected materials and their IPCs. In topology design, structures of strut-base, TPMS and stochastic are listed, followed by double-phase IPC models. In manufacturing methods, the schematics of the 7 types of AM are shown, their mechanisms and applicable materials can be found in Table 1. Empirically fabricated scaffolds and IPCs are listed below the figure. In applications, (A) penetration test sample for armour design with excellent projectile resistance and light weight [21], (B) orthopaedic implants that promote bone growth and accelerates patient rehabilitation, (C) pickle ball paddle with lattice core for sound and energy absorption, (D) customised biological implant with Gyroid inner structure, allowing modification of the overall modulus and strength of the implant for better biocompatibility with surrounding bioenvironment [22,23]. More applications can be found in the summary by Nazir et al. [24].

[32,33]. Unlike stochastic or periodic designs, aperiodic microlattices offer customisable global behaviour through local geometric diversity, making them particularly attractive for mechanical metamaterials. A detailed discussion can be found in Section 3.3.

Surface-based, rather than strut-based architectures can enhance certain mechanical properties such as the specific energy absorption and damage resistance [34]. This has been one of the primal motivations for the investigation of TPMS architectures [35], whose distinctive zero-mean curvature and design have been shown to allow for superior strength-to-weight ratios, energy absorption capacities, and thermal conductivity attributes [36–38]. Among them, different architectures, such as the Primitive and IWP designs exhibit inherent symmetries which contribute to a balanced distribution of forces, leading to uniform stress fields [39,40]. Representative mathematical definitions of TPMS topologies are provided in Table 2, with the constant C to control the thickness of the surface and therefore the volume fraction.

Apart from the advancements in the development and analysis of metamaterial topologies, significant breakthroughs have been also witnessed in the engineering of architected composites, fabricated out of two or more distinct material phases [44]. Traditionally, composites were manufactured by the addition of discontinuous reinforcement such as dispersed fibres, particles, or whiskers into a continuous matrix phase, typically named as matrix-inclusion composites (MICs) [45,46]. Among MICs, metal matrix composites (MMCs) represent a widely studied sublet wherein the matrix phase is metallic, and typically reinforced by ceramic particles, continuous fibres and whiskers to enhance mechanical, thermal and wear resistant ability. However, both MICs and conventional MMCs suffer from interfacial limitations due to the discontinuity of the reinforcement phase. With the advancement of manufacturing technologies, the design and fabrication of composites with interpenetrating phases with controllable structures became feasible. Such materials have

Table 1. Categories of additive manufacturing and the materials they can process [18–20].

Process	Mechanism	Materials
Material Extrusion (ME)	Material is selectively dispensed through a nozzle or orifice	M, C, P
Material Jetting (MJ)	Droplets of build material are deposited onto a build platform in a layer-by-layer fashion	P
Binder Jetting (BJ)	A liquid bonding agent is selectively deposited to join powder materials	M, C
Powder Bed Fusion (PBF)	Thermal energy selectively fuses regions of a powder bed	M, C, P
Direct Energy Deposition (DED)	Focused thermal energy is used to fuse materials by melting as they are being deposited	M
Vat Photopolymerization (VP)	Liquid photopolymer resin contained in a vat is selectively cured by exposure to light, typically ultraviolet (UV) or visible light	C, P
Sheet Lamination (SL)	Sheets of material are successively bonded together to form a part through ultrasonic welding or adhesive bonding, followed by machining	M, C, P

Table 2. Mathematical definitions of representative TPMS topologies [41–43].

Topology	Mathematical Equation
Primitive	$\cos x + \cos y + \cos z = C$
IWP	$2(\cos x \cos y + \cos y \cos z + \cos z \cos x) - (\cos 2x + \cos 2y + \cos 2z) = C$
Gyroid	$\sin x \cos y + \sin y \cos z + \sin z \cos x = C$
Diamond	$\sin x \sin y \sin z + \sin x \cos y \cos z + \cos z + \cos x \sin y \cos z + \cos x \cos y \sin z = C$
Fischer-Koch	$4(\cos x \cos y + \cos y \cos z + \cos z \cos x) - 3 \cos x \cos y \cos z = 0$

been named Interpenetrating Phase Composites (IPCs) [47]. More recently, architected IPCs have emerged as a distinct class of IPCs that distinguish themselves from traditional composites—such as conventional MMCs—through their deliberately designed, co-continuous phase architecture. This topology enables superior load transfer, enhanced damage tolerance, and exceptional energy absorption by establishing continuous stress paths through both phases, promoting mechanical synergy and minimising stress concentration [48,49]. This structure continuity results in superior mechanical properties—such as yield strength, toughness, and specific energy absorption—that surpass the bounds achievable by single-phase or discontinuously reinforced materials [50]. Moreover, architected IPCs offer precise tunability of both local and global material behaviour through topological and phase design, making them uniquely suited for multifunctional applications in structural, biomedical, and protective domains.

Most architected IPCs fall into the category of mechanical metamaterials due to their carefully designed structures that integrate distinct material phases in a continuous and synergistic manner, enhancing their overall performance. Architected IPCs typically consist of a reinforcement structure in a truss, skeleton framework, or sheet topology. The use of wire mesh stacks, modified ‘Einstein’ monotiles, and punched-through foam ingots with perpendicularly intersecting inner struts are representative examples of their inner design flexibility [33,51,52]. The second, matrix phase is typically infiltrated into the negative space of the reinforcement, where the chemical independence of the phases and mechanical

interlocking formed at the interfaces contribute to the overall functional properties [53].

IPCs can be categorised by the phase combination and the preform manufacturing technique, with the former to delineate the anticipated application area, and the latter to influence the overall performance and mechanical characteristics [53]. Classifying the up-to-now engineered IPCs with respect to the combination of materials, the following broad IPC classes can be formed: metal-metal (MM), ceramic-metal (CM), polymer-metal (PM), ceramic-polymer (CP), and polymer-polymer (PP) IPCs [54,55]. Common combinations for MM IPCs include tungsten (W) + copper (Cu), titanium (Ti) + aluminium (Al), titanium (Ti) + magnesium (Mg), and stainless steel 316L + titanium (Ti) alloys [56]. While Tungsten has the highest melting point among metal materials, it shows poor machinability due to its high hardness, contrary to copper (Cu) which possesses excellent ductility and energy absorption capacities, along with decent corrosion resistance and conductivity, resulting in high strength and high energy absorption. The same applies to Ti-Al IPCs, which constitute promising high strength-to-weight ratio composites. Mg-Ti composites exhibit superior mechanical properties than as-cast pure Mg and Ti scaffolds while maintaining a moderate Young’s modulus, enhancing their compatibility with bone structures. Additionally, the degradability of Mg phase facilitates bone ingrowth into the scaffold as it dissolves, making these composites highly promising in biomechanical applications [57,58].

In the class of CM IPCs [59], one of the most extensively studied phase combinations is alumina ceramic (Al_2O_3) and aluminium alloy [59,60], while other types,

including oxide ceramics (SiO_2 [61]), carbide ceramics (SiC [62], WC [63]) and nitride ceramics (BN [64,65]) to garner as well significant attention. Ceramics are known for their brittle properties, which greatly jeopardise their applicability, despite their outstanding strength. In CM IPCs, the introduction of a second metallic phase resolves the brittleness limitation of monolithic ceramic systems, with the ductile alloy providing enhanced energy absorption and mechanical resilience. Architected CM IPCs inherit the fundamental load transfer characteristics, wherein the metallic phase initially accommodates deformation and progressively transfers load to the stiffer ceramic network as strain increases [66]. This phase-level load redistribution mechanism—well established in non-architected CM IPCs—remains central to the mechanical synergy observed in architected systems, while the added benefit of topological control in architected designs enables more efficient stress distribution, delayed failure onset, and localised reinforcement [67]. A more detailed analysis of this mechanism is provided in Section 4. Regarding PM and PC IPCs, polymer materials such as PU (polyurethane) have been commonly used as the matrix in the form of foam lattice for further metallic coatings [68], while epoxy has been used as the second phase, infiltrated into metal or ceramic reinforcements or precursors [33,69,70].

IPCs composed of polymer and polymer are also known as interpenetrating polymer networks (IPNs) [71], denoting two crosslinked polymer networks that are physically entangled, but not chemically linked [72]. Commonly employed polymer materials include epoxy/PU [73,74], Polystyrene (PS), and Polymethyl methacrylate (PMMA) [75,76]. IPNs are usually fabricated through sequential synthesis or simultaneous interpenetrating network (SIN) synthesis, involving the preparation of both monomers and cross-linkers in different orders [77,78]. Fabrication through additive manufacturing has also been explored over the years [79,80], with current practice to allow for the engineering of different PP architected IPCs [81,82]. PP IPCs are utilised in various applications, ranging from the biomedical engineering field to energy storage, coating, and damping materials [71,83,84]. Notwithstanding, PP IPCs have typically low strength [81], compared to architected composites that include metallic or ceramic phases [33], so that they will not be included in the analysis to follow.

The manufacturing of architected IPCs remains one of the major challenges. Traditional subtractive or continuous manufacturing methods face significant challenges, including limitations in fabricating complex, interconnected geometries and restrictions in material compatibility [85]. 3D-printing based AM methods offer

exceptional manufacturing capabilities in the production of arbitrarily complex and variable geometric architectures, along with customisation, and efficient fabrication [86–88]. As such, they typically form the basis for the creation of the reinforcement phase of IPCs, as they allow for the engineering of metamaterials with intricate internal structures [89–93]. The International Organisation for Standardization (ISO) and ASTM International classify additive manufacturing processes into 7 categories according to their varying mechanisms and compatible materials, as listed in Table 1 [94,95], and the schematics of Figure 1-Manufacturing.

Among the techniques listed in Table 1, powder bed fusion (PBF) – including selective laser sintering (SLS), selective laser melting (SLM), and electron beam melting (EBM) [89,96] – and vat photopolymerization (VP) are prominently utilised for fabricating architected topologies. In SLS, powder particles are partially melted, resulting in parts with higher porosity and rougher surface finishes, while SLM and EBM fully melt the powder particles to produce denser components with superior mechanical properties [97,98]. EBM, operating in vacuum with higher energy density, can process larger powders improving flowability and packing density [99,100]. VP utilises a light source to selectively cure liquid photopolymer resin or ceramic slurry layer by layer, enabling the creation of complex structures with high resolution and smooth surface finishes. Based on the curing method, VP can be categorised into stereolithography (SLA), which uses single laser spot, and direct light processing (DLP), which cures an entire layer at once via projection light [101]. Both methods yield high accuracy and excellent surface finish, making VP advantageous for fabricating intricate architected designs. In contrast, Directed Energy Deposition (DED) involves focussed thermal energy to simultaneously melt and deposit material, allowing the repair or addition of features on existing components. Among AM categories, ME, MJ, and VP are typically classified as indirect AM due to the need for post-processing or moulds, while others like PBF and DED are considered direct AM processes [102].

Two of the most widely adopted techniques in the fabrication of composite materials are squeeze casting and inert gas pressure infiltration (GPI) – both of which have been extensively used for producing IPCs with fully interpenetrating and dense microstructures [103,104]. Squeeze casting involves the application of high mechanical pressure during metal infiltration into porous ceramic preforms, leading to strong phase bonding and reduced porosity, and further resulting in improved mechanical properties, including residual stress mitigation and enhanced fracture toughness

[105–107]. Inert gas pressure infiltration, on the other hand, utilises inert gas (typically Argon) to drive molten metal into the ceramic network under controlled pressure conditions, thereby avoiding oxidation and ensuring uniform infiltration even in fine-pore foams, and further attributing to excellent compressive and flexural strength [108–110]. While both methods are widely used in the fabrication of non-architected IPCs, their application in architected IPCs is more selective. Due to the geometric delicacy of architected designs, squeeze casting is rarely adopted, whereas gas-assisted pressure infiltration, often in conjunction with investment casting, remains one of the few compatible and effective methods for these systems [111].

While most of the additive manufacturing methods have enabled the fabrication of single-phase architected topologies, they typically fall short in the single-step fabrication of IPCs. Despite advances in multi-material AM, achieving fully integrated IPCs using AM alone remains challenging [112]. In response, hybrid manufacturing (HM), which combine multiple monolithic manufacturing techniques, has been extensively investigated [113,114]. Hybrid manufacturing of IPCs effectively leverages the strengths and compensates for the limitations of each manufacturing method [115–118]. Although AM offers outstanding design freedom and rapid prototyping, its surface quality and feature resolution often lag behind traditional methods like investment casting (IC) [119–121], motivating hybrid approaches that combine AM and casting [122,123]. Hybrid manufacturing is typically classified as sequential HM, mixed HM, and AM-assisted HM [124]. HM approaches for architected IPCs are typically sequential, starting with the AM fabrication of a porous precursor, followed by infiltration of a secondary phase – commonly carried out by casting such as investment casting, sand casting, and injection moulding [125,126]. The specific processes applied in each case will be further detailed in Section 3.

2. Objective and scope

During the last years, a substantial number of works on architected composites and IPCs has been presented, with particular emphasis on novel material combinations, topological designs and fabrication methods. The number of publications and their associated application domains are summarised in Figure 2. The volume of related research has nearly quadrupled over the past decade, with a particular emphasis on materials science, engineering, and physics, including astronomy. While these studies have provided valuable insights, there remains a pressing need for a

conclusive and interconnected review that captures the achievements in mechanical behaviours of various IPCs with architected designs across different categories. As such, it would provide an unprecedented understanding of their potential, bridging the gaps between material science, structural engineering, and practical applications.

In this light, the current review work meticulously compiles and examines various manufacturing methods for IPCs, focussing on four key material combinations: metal-metal (MM), ceramic-metal (CM), polymer-metal (PM), and polymer-ceramic (PC) composites. In Section 3, a comprehensive analysis and comparison of the fabrication methods is provided. Advantages and limitations of each approach are discussed, establishing a robust foundation for the understanding of the advancements and challenges in IPC manufacturing. Additionally, detailed data on the mechanical behaviour of as-built IPCs have been collected. In Section 5, testing data from various studies are meticulously extracted and presented using Ashby-type plots, providing a comparative analysis of the mechanical performance across different IPCs. Current limitations and future perspectives are listed in Section 6, while the key points are summarised in Section 7.

3. Manufacturing methods

In this section, the typical manufacturing methods for different IPC designs are elaborated according to their underlying material phase compositions. The manufacturing methods typically include in the first step the fabrication of the reinforcement phase or precursor, followed by the infiltration of the second phase. The fabrication technology and processes may however substantially differ depending on the material phase combination, as detailed in the sequel.

3.1. Metal and metal (MM IPCs)

MM IPCs are composed of two distinct metallic phases. The most common two-phase MM IPCs contain a metallic precursor infiltrated by another metallic alloy. The manufacturing process can be categorised into two primal workflows: the first of them including a single casting step and the second, two consecutive casting steps. The creation of the reinforcement phase can be either performed through a complete casting step (Figure 3(A)) or employing 3DP methods (Figure 3(B)). In the creation of the reinforcement phase through casting (Figure 3(A)), fabrication begins with the creation of a wax sample and the associated sprue tree

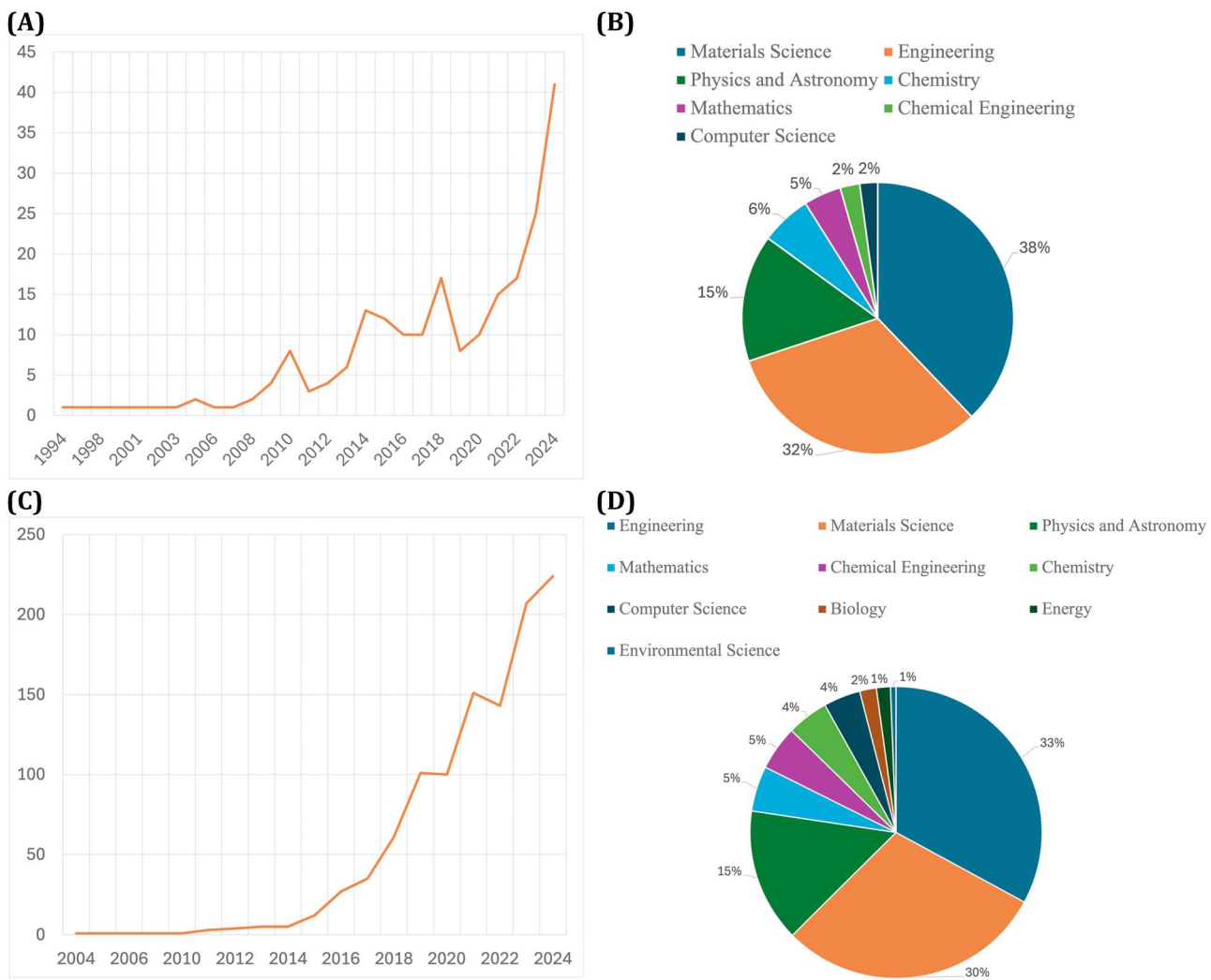


Figure 2. The number of articles published related to (A) interpenetrating phase composite in each year from 1990 to 2024 and articles related to (C) architected materials from 2004 to 2024. (B,D) The subjects of these articles, respectively (Source: from Scopus, accessed in January 2025).

(Figure 3A(a)). The assembly is subsequently placed into a flask for metal investment casting (Figure 3A(b)). Afterwards, the casting sample is separated from the sprue tree by machining and prepared for the subsequent procedure, as continued with the process in Figure 3B(b). In contrast, the single casting process starts from the direct 3D printing of the metallic sample (Figure 3B(a)). The printed sample may undergo a chemical or heat treatment, if necessary, or proceed directly to the following process as a precursor. The precursor is then placed inside a wax box, typically printed via SLA, with dimensions precisely matching those of the sample. This wax box containing the sample is usually manually attached to a sprue tree and fixed with glue (Figure 3B(b)). From this stage, both single and two-step casting processes proceed with a similar workflow (Figures 3B(b) to 3B(d)). The sprue tree is subsequently used to produce the investment flask, enabling the investment casting

of the second-phase matrix metal (Figure 3B(c)). After casting, post-processing that generally involves machine cutting to remove excess materials is carried out (Figure 3B(d)).

In the fabrication of the metallic precursors, the typical fabrication methods include SLM, EBM, SLS, etc. For example, Singh et al. [114] manufactured steel/Al (316L stainless steel and AlSi10Mg alloy) IPCs following the process shown in Figure 4(A). The procedure started with printing the Gyroid 316L lattice by selected laser melting (SLM), followed by fabricating the wax box by stereolithography (SLA). The employment of 3D-printing to build the box ensures the precise dimensional match with the samples. The wax box containing the sample was then attached to a sprue tree, and subsequently soaked in a flask filled with investment and binder. The following casting process was performed in a vacuum environment, ensuring a final product

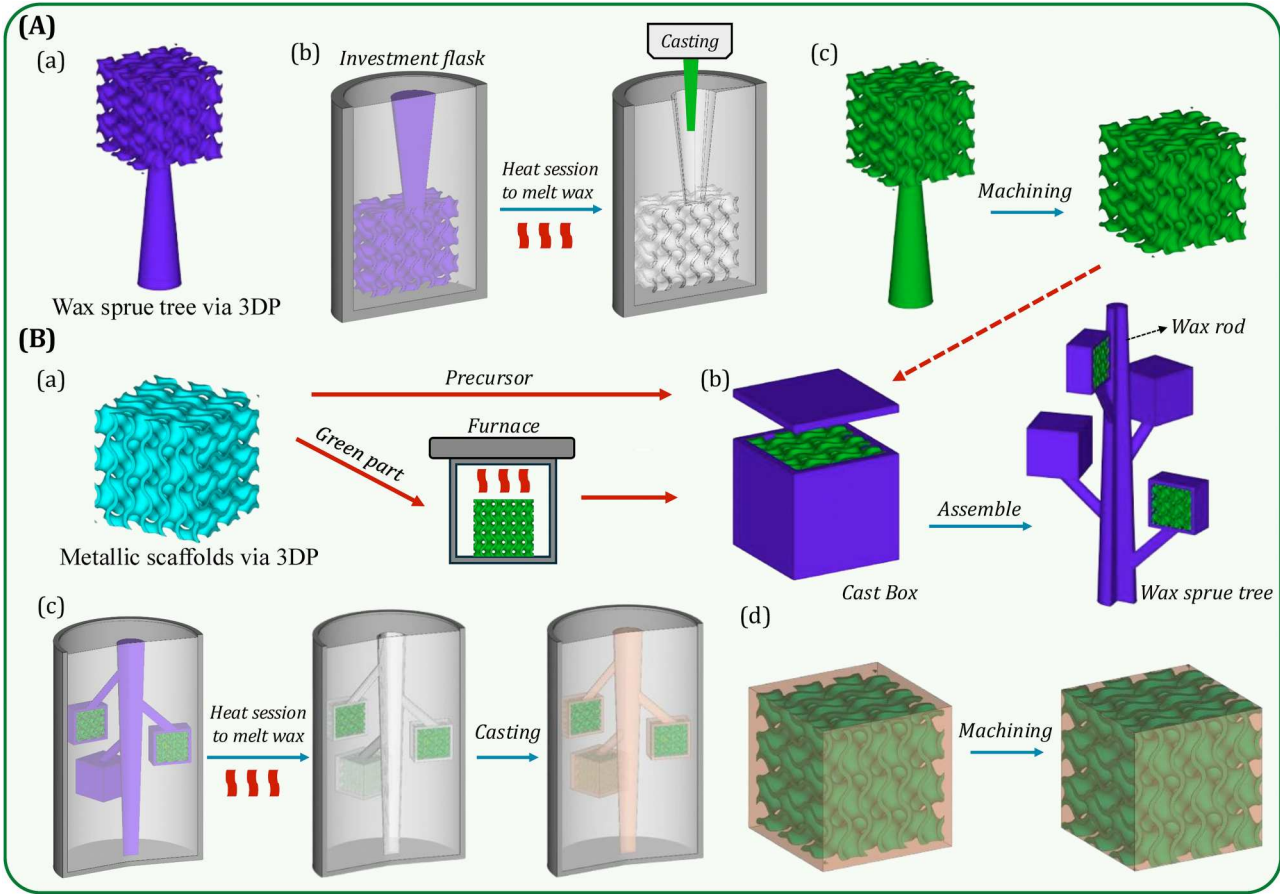


Figure 3. The general process of MM IPCs via hybrid casting. (A) Double casting HM process; (A-a) 3DP wax sample and wax sprue tree, (A-b) produce flask for investment casting, (A-c) cut the casting sample off the tree. (B) Single casting HM process; (B-a) Direct 3DP of the metal scaffolds. Heat treatment is required for green parts, otherwise the precursors can be directly used for further infiltration. (B-b) 3D print cast boxes that match the precise dimension of the sample. Build the sprue tree with cast boxes and samples. (B-c) Make the investment flask, which includes heat treatment to melt the wax tree. (B-d) Post processes including cutting the samples off the sprue tree, removing excess materials and enhancing surface finish, usually through machining.

with reduced porosity and defects. Li et al. [130] studied the mechanical behaviours of a Ti/Al IPC. The titanium Gyroid precursor structure was 3D-printed using SLM in the initial step. The precursor was subsequently placed in a container (a crucible or graphite box or plaster mould) to infiltrate the melted aluminium alloy by casting. After the casting process, the specimen typically requires further post-processing, such as grinding and cutting. A similar fabrication process can be found in the study of Zhang et al. [131], in which a rhombic dodecahedrons (RD) NiTi skeleton was printed by SLM first, followed by pressure-less Mg casting. The casting process can be performed in different variants, such as high-pressure (die) casting (HPDC) and vacuum casting, to reduce porosity and improve accuracy. For instance, pressurised casting was utilised by J.T Zhai et al. [132] while vacuum casting can be found in the work of Ghasri et al. [133]. Yet, there are limited comparisons among the final performance of specimen

engineered with different hybrid casting processes, despite the rather thorough investigation of the impact of processing parameters on most additive manufacturing methods [134–139].

In addition to SLM, other distinct methods for precursor preparation have been reported. Tulpan et al. [140] utilised EB-PBF (electron beam – powder bed fusion) to print Ti64 lattice scaffolds. As previously mentioned, EB-PBF (or EBM) is a variant of the PBF method, with higher laser beam energy that works in vacuum. Due to the particle dispersal, non-uniform melting, and partial vaporisation attributed to the high energy source, EBM usually results in lower residual stress, but tougher surface finishing [141]. Apart from additive manufacturing and casting, other methods have been reported for the fabrication of MM IPCs. Yulin Lin et al. [127] fabricated an Al-Al IPC through hot extrusion, the schematic of the method is illustrated in Figure 4(B). The honeycomb-structured precursor was printed by

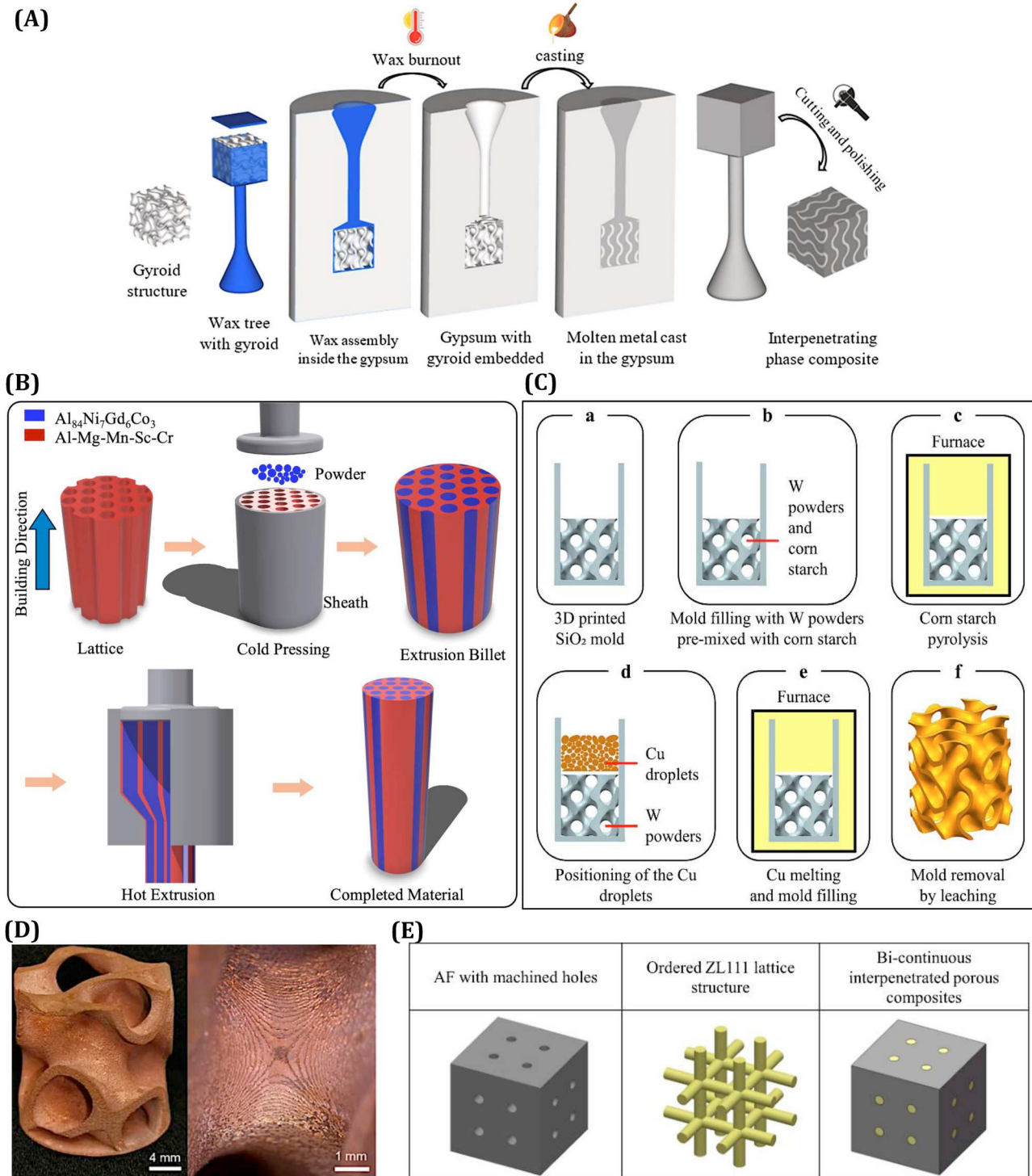


Figure 4. (A) The fabrication procedure of Gyroid 316L stainless steel and AlSi10Mg IPC involving SLM, SLA and vacuum casting [114] (License number: [5962240644661]). (B) Hot extrusion of an Al-Al IPC (schematic remade from [127]). (C) Schematic of fabrication of W-Cu IPC with CS and (D) the as-built W-CU IPC part, with Cu filling the gaps (Adapted from [128], licensed under CC BY). (E) An Al-Al IPC with the configuration of penetrating trusses by [129] (License number: [5962551252615]).

SLM first, then aluminium powder was packed into the precursor under mechanical vibration to ensure dense packing, followed by cold pressing and hot extrusion at different temperatures. Endian Liu et al. [129] fabricated as well Al-Al IPCs. Their fabrication approach

however differed by directly utilising an aluminium foam (AF) ingot, instead of employing additive manufacturing, as schematically presented in Figure 4(D). The precursor was subsequently machined by wire cutting to create lattice structures with desired configurations.

These lattice structures were then used for further infiltration processes. It is worth noticing that the feasibility of this method is attributed to the special configurations of the reinforcement aluminium, with struts penetrating the precursor matrix horizontally and perpendicularly in a relatively simple manner (Figure 4(E)), enabling the manufacturing by subtractive wire cutting machining. It is however rather evident that limitations in the production of complex IPC designs appear, such as TPMS or advanced strut-based structures.

In terms of special structures, D. Vigano et al. [128] designed a fabrication workflow to create W + Cu MM IPC with the assistance of corn starch that acted as space holder. A SiO₂ mould was initially fabricated using SLA (stereolithography), which is a common method in the additive manufacturing of resin materials, then filled up the mould with a mixture of W powder and corn starch (CS) particles with different volume fractions. A pyrolysis process was subsequently conducted in a furnace to fully melt the W powder and decompose the corn starch, followed by the melting and infiltration of Cu powder. At last, the pre-printed SiO₂ mould was removed by leaching, leaving a W + Cu IPC with the Gyroid lattice structure. The fabrication process and the final sample structures are provided in Figure 4(C, E). They reported that the corn starch effectively acts as space holder, providing more pores and gaps for Cu to fill in, as a higher initial corn starch volume fraction in the W-CS powder mixture led to higher Cu proportion in the final sample. In comparison with the reported methods, this study used powder sintering and melting to complete the interpenetration of both metals, rather than printing one metal scaffold first. In addition, the lattice-structured IPC is expected to exhibit lighter weight and reduced density, compared to fully infiltrated IPCs in the aforementioned studies, and thus results in higher specific strength and specific energy absorption. Notwithstanding, compressive tests were not conducted to verify the hypothesis. As a result, comparative experiments involving the fabrication of fully infiltrated IPC using Cu are yet to be performed. Comparing the mechanical properties of this configuration with those of a hollow lattice IPC will help validate the advantages of the latter.

The previous analysis indicates that the fabrication of MM IPCs typically involves printing a metallic lattice precursor followed by infiltration with a second metal phase. The most widely used approach combines SLM-based precursor fabrication with vacuum or investment casting of molten aluminium alloys, enabling high-resolution topologies such as TPMS and Gyroids

[114,130,133]. These methods yield strong metallurgical interfaces, although surface oxidation may still affect bonding. Variants like high-pressure die casting (HPDC) have been applied to infiltrate metallic glass into printed steel scaffolds, achieving diffusion bonding and excellent interfacial strength [132]. Alternatively, hot extrusion, used by Lin et al. [127], involves packing aluminium powder into printed honeycomb lattices and extruding the assembly—providing dense, forged bonding, but limiting structural complexity. To reduce cost and simplify processing, Liu et al. [129] replaced additive precursors with machined aluminium foams. While scalable, this subtractive approach constrains geometry to basic lattice types. A more customisable method by Viganò et al. [128] introduced a space-holder-based casting process, where tungsten and corn starch were packed into SLA moulds, sintered, and infiltrated with molten copper—allowing volume fraction control but requiring further mechanical validation. Finally, EB-PBF followed by melt immersion has been used by Tulpan et al. [140] to infiltrate Ti64 structures with AlSi, achieving well-bonded interfaces and competitive mechanical strength. These methods vary widely in scalability, porosity control, and bonding quality (Table 3). AM-based casting remains dominant for precise lattices, whereas extrusion and unconventional methods target simpler or high-performance reinforcement strategies.

3.2. Ceramic and metal (CM IPCs)

Ceramic materials are known for their high hardness, compressive strength, stiffness, and thermal stability, but they tend to be brittle, exhibiting severe shattering upon loading above a strain threshold, contrary to metals which possess good ductility and toughness. Therefore, the primal idea of CM IPCs has been to leverage the complementary properties of both materials, achieving high strength and stiffness from the ceramic phase and good energy absorption from the metal phase, resulting in superior thermomechanical properties [59,114]. Beyond the mechanical synergy between the two phases, critical mechanisms contributing to the superior performance of CM IPCs have been revealed in several works. For instance, in situ diffraction experiments have shown that under increasing mechanical load, stress is initially absorbed by the metallic phase but is progressively transferred to the stiffer ceramic phase, especially as the metal begins to yield plastically [142]. Furthermore, in lamellar or freeze-cast microstructures, the degree of load transfer is highly directional, with the ceramic phase carrying more than twice the applied macroscopic stress along aligned architectures

Table 3. Comparison of fabrication methods for MM IPCs.

Method	Precursor Fabrication	Matrix Infiltration	Geometric Freedom	Interface Quality	Porosity Control	Study
SLM + Vacuum/Investment Casting	SLM (316L, Ti)	Al, AlSi alloys via vacuum or IC	High (TPMS, Gyroids)	Moderate–High (oxide-sensitive)	Medium	[114,130,133]
SLM + HPDC (MG lattice)	SLM (SS)	Metallic glass (Vit1) via HPDC	High	High (diffusion zone ~1.5 μm)	Excellent	[132]
SLM + Hot Extrusion	SLM (Al honeycomb)	Powder-packed + hot extrusion	Low–Moderate	Very High (forged bonding)	Excellent	[127]
Foam Cutting + Casting	Machined Al foam	Melt infiltration	Low	Moderate	Moderate	[129]
SLA Mold + Space-holder	SLA + W + CS mixture	Cu infiltration post-pyrolysis	Moderate	Variable	Tunable by CS content	[128]
EB-PBF + Immersion Casting	EB-PBF (Ti64 lattice)	AlSi melt immersion	Moderate	High (clean interface zone)	Good	[140]

[143,144]. In addition to mechanical improvements, CM IPCs exhibit reduced and anisotropic thermal expansion, an essential property for structural components in fluctuating thermal environments. Studies on aluminium–ceramic IPCs have reported significant suppression of the overall coefficient of thermal expansion (CTE) due to the constraining effect of the ceramic phase [145,146]. Moreover, directional thermal expansion is evident in composites derived from freeze-cast or uniaxially pressed ceramic preforms, where anisotropic stiffness leads to higher CTE along compliant directions [146]. This tailored thermal response is particularly beneficial for applications requiring thermal dimensional stability, such as aerospace, automotive, and electronics packaging.

In CM IPCs, the ceramic phase is usually manufactured in the first step as the precursor, followed by the infiltration of the metallic phase. Silicon carbide (SiC), Titanium carbide (TiC) and aluminium oxide (Al_2O_3 , alumina ceramics) have been up to now investigated as the reinforcement phase, with the overall CM fabrication process to be nearly identical for most of the reported cases. At the first step of the ceramic scaffold fabrication, the most used method has been vat photopolymerization. The ceramic material is therefore in the form of fine powder dispersed within a photosensitive resin to create a slurry. The slurry is then poured in the vat, and the UV light cures the desired shape. By repeating the process layer by layer, the green part is created. The post-processing generally involves heat treatment, which debinds and removes the polymer, and subsequently sinters and densifies the ceramic to create the porous scaffold. The second step of the manufacturing is similar to that in MM manufacturing. The metallic alloy is melted and infiltrated into the ceramic scaffold, usually held in a crucible or graphite mould. The post-infiltration cooling is typically controlled to ensure firm bonding between the two phases and in order to avoid defects, such as porosity and interface discontinuities.

In one of the most characteristic examples of ceramic–metal IPC manufacturing, Zhang et al. [147] created Gyroid and honeycomb structures by first 3D-printing ceramic scaffolds by SLA with Al_2O_3 of mixed particle sizes. Subsequently, the 3D-printed samples were heated to 550 degrees to remove the Al_2O_3 embryo, followed by a complete densification process with temperatures rising to 1600 degrees with a 5 degrees/min increment, and held at that level for 120 min. The post-processed ceramic scaffolds were then placed in a crucible, and melted aluminium alloy (Al-Mg-Si) was cast into the scaffolds in a furnace with O_2 removed. The fabrication process and final products are provided in Figure 5(A,B). Nearly the same process of SLA and casting has been employed for the creation of different IPC architectures [149], while DLP and casting have been as well combined [150–152], with minor differences in the quality of as-built samples. Notably, in a further variant of the method, Jesus Rivera et al. [153] first employed SLA to print the lattice mould with wax resin, followed by the infiltration of aluminium suspension slurry using CAP (centrifugally assisted packing). The as-built wax resin–ceramic samples went through a further burn-out cycle to remove the wax resin, the space occupied by which was now for the casting of aluminium alloy in vacuum. This method was employed mainly for the fact that wax resin moulds are easier to print upon higher precision and with complex geometric features while 3D-printing the ceramic phase directly can be challenging when it comes to fine details.

One outstanding example is pyrolytic carbon, which is a form of carbon material produced through the thermal decomposition of hydrocarbons in an inert atmosphere. Its structure can vary from amorphous to highly ordered, depending on the specific conditions of its formation. While not a typical ceramic material, pyrolytic carbon exhibits high-temperature stability and brittleness, characteristics commonly associated with ceramics. In the work of Jens et al. [148], a novel nano-scale ceramic–metal IPC was fabricated using

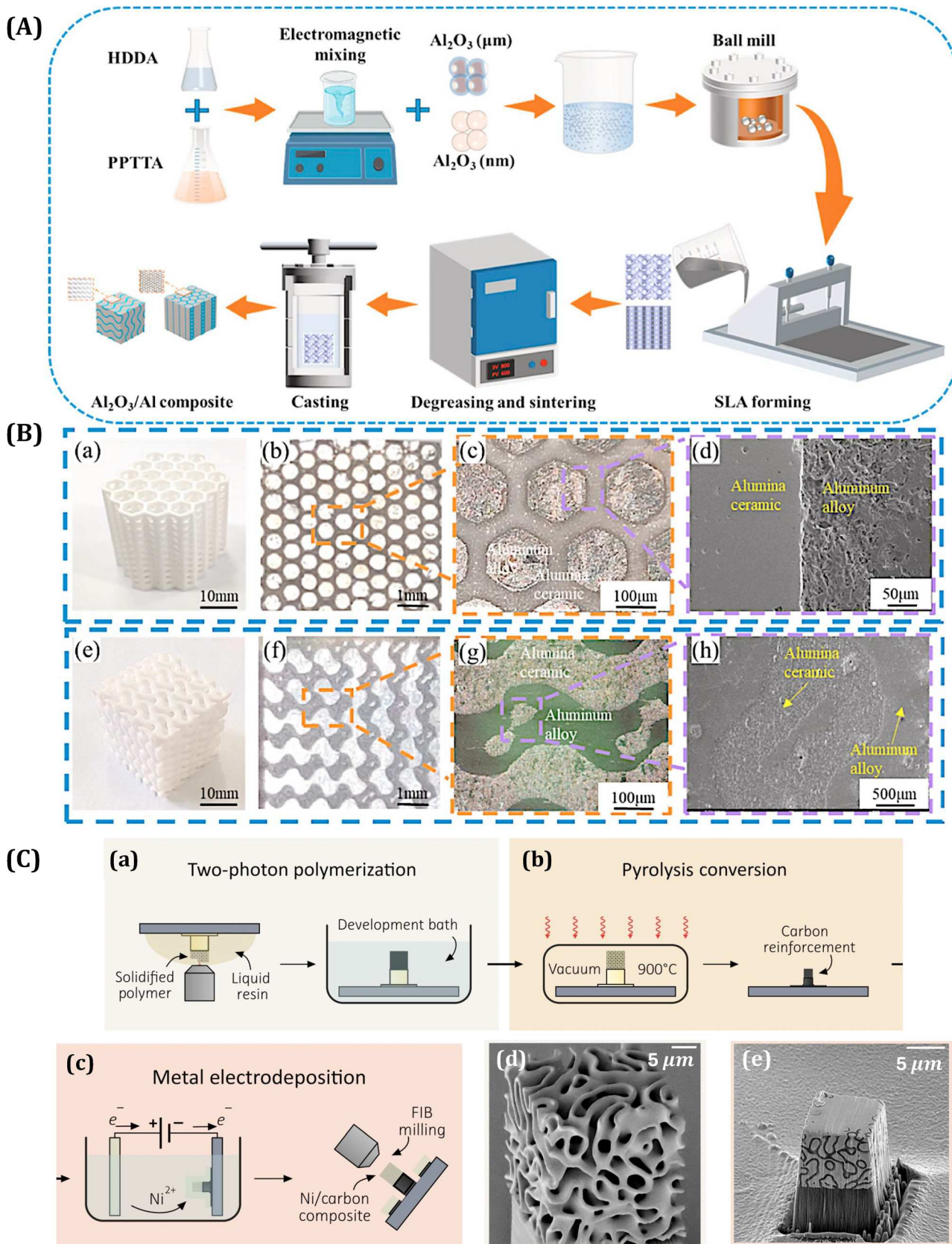


Figure 5. (A) The manufacture process of ceramic+metal IPC by SLA and casting, (B-a,e) the ceramic scaffold with honeycomb and Gyroid structure, respectively, (B-b,f) the IPC parts after infiltration, detailed macroscopic shown in (B-c,g) and scanning electron micrograph (SEM) of the interface area between ceramic and metal phases [147] (License number: [5962640412980]). (C-a–c) The fabrication of nano-architected pyrolytic carbon and nickel IPC, and the SEM images of the TPP-DLW 3D printed polymer reinforcement template (C-d) and the final IPC sample after focussed ion beam (FIB) milling (C-e) (Adapted from [148], licensed under CC BY-NC).

Table 4. Comparison of CM IPC fabrication methods with infiltration types.

Scaffold Fabrication	Metal Infiltration Method	Geometric Fidelity	Remarks	Study
SLA + sintering (Al_2O_3)	Gravity casting (Al-Mg-Si) in vacuum furnace	High	Large-scale TPMS with staged sintering	[147]
DLP + sintering	Vacuum-assisted melt casting (Al)	High	Impact behaviour of different cell sizes	[150]
DLP + sintering	Gravity casting (Al)	High	Topology-deformation interaction explored	[151]
DLP + sintering	Vacuum casting (Al)	High	Bidirectional Gyroids for energy absorption	[152]
SLA wax mould + CAP ceramic fill	Vacuum casting (Al) post-burnout	Very High	Mold-assisted for better resolution	[153]
SLA + sintering (TiO_2)	Gravity casting (Ti alloy)	Moderate-High	Structural tuning for stiffness control	[149]
TPP-DLW + pyrolysis (C)	Electrodeposition (Ni)	Very High (nano)	Low-temp, nano-architected system	[148]

pyrolytic carbon as the ceramic reinforcement phase. The process began with the fabrication of reinforcement architecture templates on silicon substrates using a photoresist via two-photon polymerisation direct laser writing (TPP-DLW). This was followed by a chemical cleaning step to remove excess material and pyrolysis at 900°C in a vacuum furnace. The resulting Gyroid and spinodal pyrolytic carbon templates were then infiltrated with nickel matrices through electrodeposition in a Watts bath for 25 min. The process and the samples are shown in Figure 5(C).

It can be concluded that, fabrication strategies for CM IPCs consistently follow a two-step hybrid route; a ceramic scaffold is first constructed, then infiltrated with molten metal. Vat photopolymerization (SLA/DLP) is the dominant method for generating high-resolution ceramic architectures, especially TPMS structures, as demonstrated by Zhang et al. [147], Lu et al. [150], and Santos et al. [151]. After sintering to densify the ceramic, gravity or vacuum-assisted casting of aluminium alloys is applied to achieve phase interpenetration. To improve feature fidelity, Rivera et al. [153] introduced a mould-based strategy, where SLA wax moulds were filled with ceramic slurry via centrifugally assisted packing (CAP), followed by post-burnout aluminium casting. This method enabled finer geometries than direct ceramic printing but increased processing complexity. In bioceramic applications, Rahmani et al. [149] employed a similar SLA + casting route using Ti alloys, enabling structural tuning via scaffold topology. For micro- and nanoscale applications, Bauer et al. [148] fabricated pyrolytic carbon scaffolds via two-photon polymerisation (TPP-DLW), followed by nickel electrodeposition. This low-temperature route eliminates thermal mismatch issues and achieves exceptional resolution, though it remains limited in scalability. Meanwhile, Matos et al. [152] highlighted how bidirectional Gyroid structures enhanced energy absorption, underlining the importance of reinforcement topology even when casting processes are similar. These workflows differ in infiltration pressure, resolution, and scalability—summarised in Table 4. While vacuum and gravity casting are common in macro-scale applications, mould-

assisted and nanoscale techniques offer precision advantages for specialised designs.

3.3. PM and PC IPCs

Polymers are popular in synergizing IPCs because of their lightweight, soft, and ductile nature, typically combined with a stiff metallic or ceramic phase. The most commonly employed polymer materials include: epoxy resins, which provide high strength and stiffness and excellent corrosion resistance and thermal stability; PU (polyurethane), which exhibits high toughness and good wear and chemical resistance; PE (polyethylene), which is low-cost, tough and has substantial impact resistance material. Unlike the manufacturing methods discussed above, the fabrication of PM and PC IPCs is quite unique from one another, resulting in IPCs with distinct properties for differing applications [154]. Outstanding examples are discussed in the sequel.

The most typical PM manufacturing process infiltrates the polymer phase at the second step, after the engineering of the metallic precursor phase. Xinxin Wang et al. [33] utilised SLM to build the precursor lattice pattern with Ti-6Al-4V powder, and then introduced epoxy liquid resin into a modified mould through vacuum impregnation, followed by a curing process in a vacuum oven to solidify the epoxy resin. The novel aperiodic topology modified from an ‘Einstein’ monotile and the complete process is shown in Figure 6(A). Analogously, Singh et al. [157] utilised PBF to fabricate the AlSi10Mg lattice in BCC, Gyroid, IWP, and Spinodal architectures, and then placed the reinforcement phases into a printed polymer box to further infiltrate the structures with an adhesive epoxy resin mixture. It is worth noting that multi-material 3D printing has also been applied to fabricate polymer–polymer (PP) IPCs, using dual-material fused deposition modelling (FDM) or PolyJet printing [158,159]. These approaches allow direct integration of bicontinuous polymer phases without post-infiltration, offering flexibility in geometries and phase combinations for functional lightweight structures.

In addition to the advancements recorded in mechanical metamaterials, efforts have been directed towards the improvement of the electromagnetic metamaterial

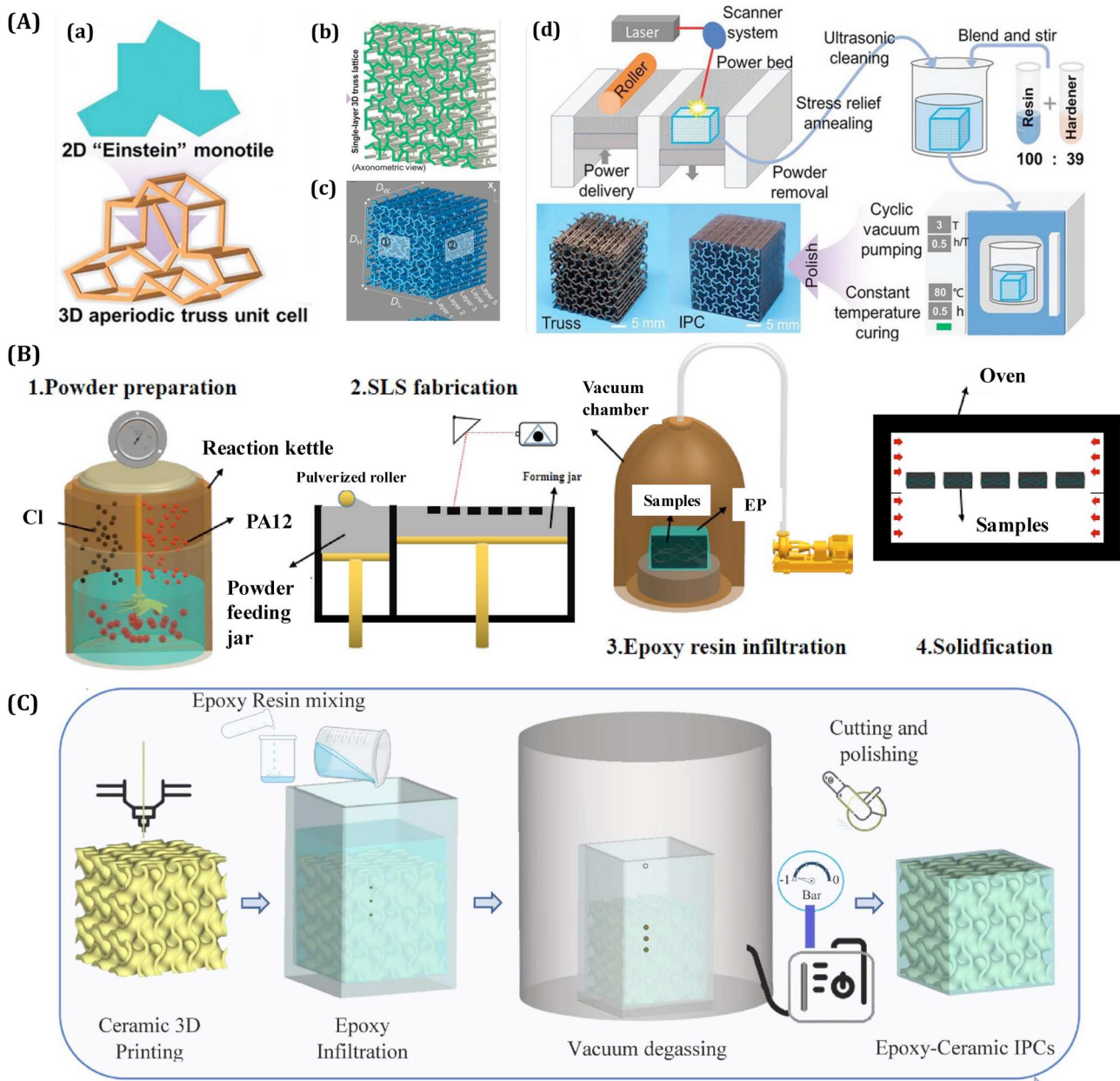


Figure 6. (A) Adapted from [33] (licensed under CC BY), (A-a) the modification and utilisation of a 'Einstein' monolite topology, which is arrayed into (A-b) the single-layer truss lattice and (A-c) the multi-layers aperiodic lattice. (B) Adapted from [155] (license number: [5962660696314]), the fabrication process of MMA, including the sintering of PA12-coated carbonyl iron, the subsequent epoxy infiltration and the post solidification process. (C) The manufacturing process of ceramic+polymer IPCs [156] (license number: [5962660923642]).

performance through the appropriate IPC design. Wen et al. [155] manufactured a metamaterial absorber (MMA) with coated Carbonyl iron (CI) reinforced by epoxy. The sample structures were first manufactured through selective laser sintering (SLS), which combines particles by partially melting and sintering them. Compared to SLM, SLS usually results in a rougher surface finish and yields lower accuracy. This is attributed to the voids and pores created between partially melted particles during printing. Nevertheless, in the study of

Wen et al. [155], SLS was employed on purpose for the previously reported characteristics. After the printing, the MMA samples were infiltrated by epoxy resin under negative pressure, where epoxy resin penetrated into the voids left in the preform structures. Furthermore, the CI particles were coated with polyamide12 (PA12) before the SLS process and PA12 formed additional chemical bonds with the epoxy resin during the infiltration, resulting in a firm bond between the metallic and polymeric phases. The process is illustrated

in Figure 6(B). The absorbing properties of the interpenetrating MMAs were enhanced, with broader bandwidth and increased peak reflection losses.

Alongside polymer and metal IPCs, the combination of polymer and ceramic has also garnered significant interest [160]. Singh et al. [156] manufactured PC IPCs, drawing inspiration from the PM IPC fabrication workflows. Ceramic Gyroid scaffolds were first printed using a fused deposition modelling (FDM) printer, which is a material extrusion AM. The scaffolds were printed using white zirconia filaments with a diameter of 1.75 mm and a layer thickness of 0.2 mm. The resulting green body underwent a thermal-chemical debinding process to remove the organic binder material and sinter the scaffolds. Thereafter, a polymer box was printed by a material jetting printer to precisely match the sample's dimension, facilitating the epoxy infiltration process. The epoxy resin, consisting of EL160-High-temperature laminating epoxy and EL160-epoxy hardener at a weight ratio of 100:35, was poured into the box containing the scaffold under vacuum to eliminate gas pores. Moreover, complementary three-phase samples on the base of PC IPCs were also manufactured, adding silicon carbide (SiC, beta, 99 +%, 45–65 nm, cubic) into the adhesive infiltration, which turned out to enhance the strength, and toughness of the IPCs. The complete process is summarised in Figure 6(C).

Diverging from the use of epoxy as the infiltrating polymeric phase, different scholars have explored the possibility of employing the polymeric -rather than the metallic- phase as the precursor scaffold and coating the metallic phase onto them. Jalilzadeh et al. [68] utilised PU (polyurethane) open-cell foam as precursors, then conducted an electroless process to process a suitable surface for coating. Subsequently, different metallic layers were applied to the PU precursor by the electro-forming method (shown in Figure 7(A)). This method provided guidance in adjusting the material's properties, by tailoring its structure. Interestingly, Tang et al. [161] proposed a novel method, named electrical field-assisted heterogeneous material printing (EF-HMP) to fabricate polymer-metal IPCs with higher flexibility. The process is illustrated in Figure 7B-(a). This method is considered a modification and improvement of the vat photopolymerization of DLP. In particular, copper ion (Cu^{2+}) is added into the photocurable resin to make a special electrolyte solution. The method generally includes two distinct processes: (1) When the UV light is turned on, the solution can be cured into the desired shape in that layer. (2) When the UV light is off and the electrical field is initiated, electrodeposition is activated (Figure 7B-(b)). The anode is placed in the

solution and generates Cu irons, which move towards the cathode, on the surface of the printed polymer sample. While the process achieves a firm interfacial connection between the copper phase and the polymer phase, and allows for the fabrication of polymer-metal IPCs with much higher design freedom, the fidelity and accuracy of the samples produced is not as satisfying as expected (Figure 7B-(c)). Nonetheless, their efforts have elaborated a novel methodology in the fabrication of PM IPCs.

Overall, fabrication methods for PM and PC IPCs diverge significantly based on precursor selection, infiltration techniques, and processing complexity. In PM IPCs, the dominant strategy begins with metallic scaffolds fabricated via SLM or PBF, followed by vacuum-assisted epoxy resin infiltration [33,157]. These workflows support intricate topologies such as Gyroids, BCC, and aperiodic tilings, while vacuum curing enhances matrix penetration and interfacial bonding. In more function-oriented designs, Wen et al. [155] used SLS-fabricated carbonyl iron (CI)-PA12 composites to intentionally retain porosity and surface reactivity for enhanced electromagnetic performance after epoxy infusion. In contrast, PC IPCs typically use ceramic scaffolds formed via FDM or DIW, followed by thermal debinding, sintering, and then resin infiltration. This approach—seen in works by Singh et al. [156] and Liu et al. [154]—enables lightweight, architected ceramics with moderate resolution but suffers from sintering-induced shrinkage and limited fidelity. Singh et al. also incorporated SiC nanoparticles into the epoxy for improved mechanical performance in three-phase systems. Alternative strategies reverse the traditional precursor-infiltration order. Jalilzadeh et al. [68] used PU foam scaffolds as the polymeric precursor for electroless plating and electroforming of metallic shells, creating metal-coated networks with tuneable stiffness. Meanwhile, Tang et al. [161] introduced a hybrid method (EF-HMP) combining DLP photopolymerization with electrodeposition, allowing for in situ Cu deposition during printing. Though promising for design flexibility, EF-HMP still faces fidelity and surface quality challenges. These workflows—summarised in Table 5—offer varying degrees of precision, scalability, and mechanical integrity, depending on the sequencing of phase fabrication and infiltration.

4. Interfacial characterisation

Interfacial bonding plays a critical role in determining the mechanical reliability of MM IPCs. In infiltration-based systems, the quality of bonding varies widely depending on processing conditions. Among the

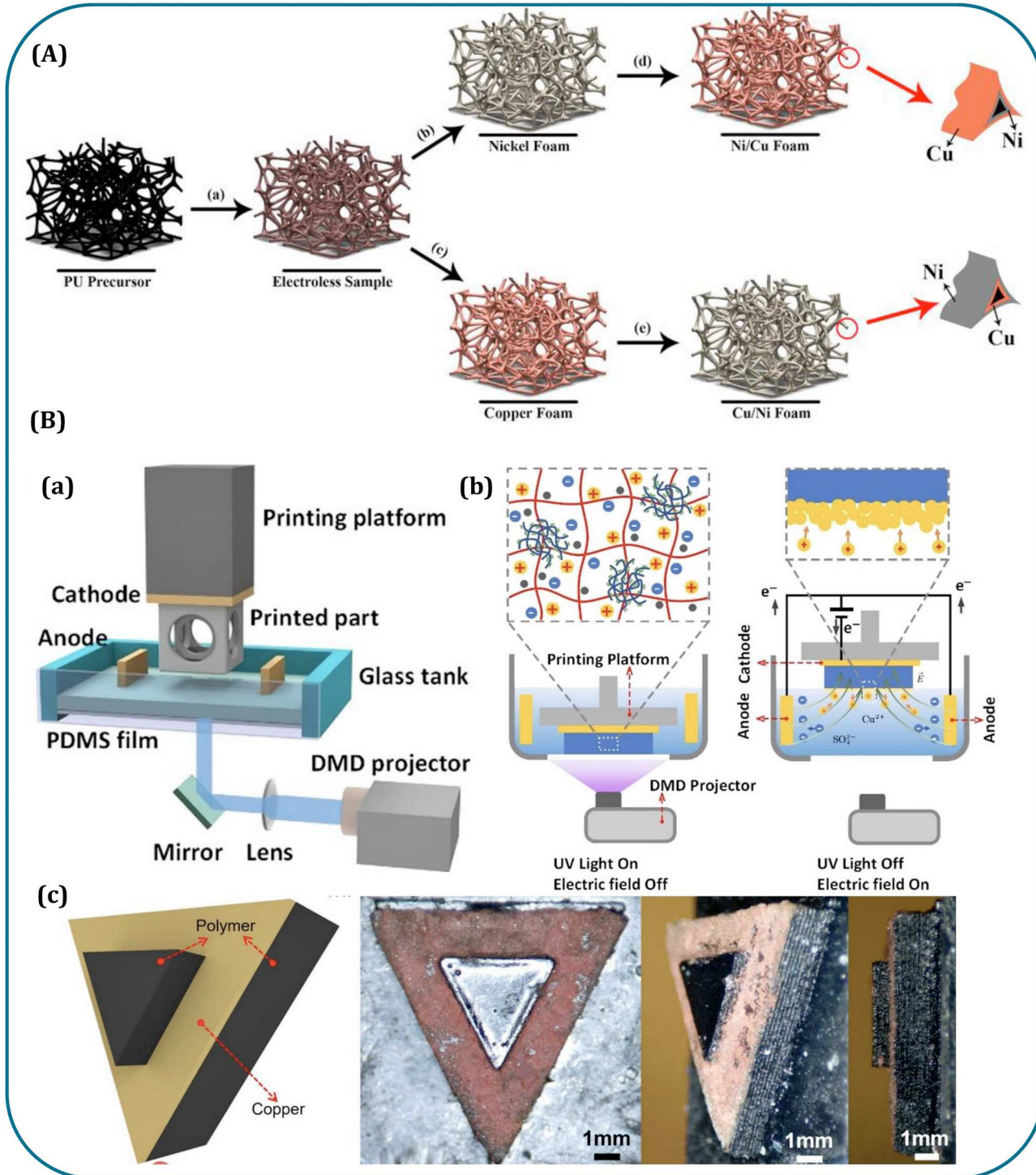


Figure 7. (A) The synergy process of metal-coated PU foam structure through electroforming [68] (license number: [5962661218827]). (B-a) Schematic for the setup of the electric field-assisted heterogeneous material printing (EF-HMP). (B-b) Schematic of the curing process in DLP of resin and the electrical field-assisted material deposition process, respectively. (B-c) The printed sample of a polymer-metal-polymer sandwich structure exhibiting evident layer-by-layer printing pattern [161].

aforementioned studies, Singh et al. [114] reported thorough interpenetration of ceramic-aluminium and steel-aluminium phase (as shown in Figure 8(A)), along with inner porosity in the aluminium phase due to gas entrapment during casting. Li et al. [130] observed

interfacial debonding and microcracking in ZL102-TC4 IPCs, noting that rough surface features promoted mechanical interlocking and energy dissipation. Different surface roughness is attributed to varying degrees of particle adhesion to the surface. The fracture

Table 5. Comparison of PM and PC IPC fabrication methods.

Method	Precursor Fabrication	Infiltration Phase	Geometric Fidelity	Study
SLM + Vacuum Epoxy Infiltration	SLM (Ti-6Al-4V, AlSi10Mg)	Epoxy (vacuum curing)	High	[33,157]
SLS + Epoxy (for EM Absorbers)	SLS (Cl + PA12)	Epoxy (vacuum filled)	Medium	[155]
FDM + Vacuum Epoxy Infiltration	FDM (zirconia filament)	Epoxy (with printed box)	Moderate	[156]
DIW + Resin Infiltration	DIW (ceramic ink)	Epoxy or hybrid resin	Moderate	[154]
PU Foam + Electroforming	PU foam scaffold	Electroless plating (Ni/Cu)	Low-Moderate	[68]
EF-HMP (UV + Electrodeposition)	DLP-like cured resin	In situ Cu ²⁺ electrodeposition	Moderate	[161]

mechanism is illustrated in Figure 8(D). In contrast, Zhang et al. [131] achieved clean metallurgical bonding in Mg–NiTi IPCs through interfacial diffusion and Mg₂Ni phase formation. Zhai et al. [132] further demonstrated that high-pressure die casting produced near-defect-free MG–SS interfaces with a narrow diffusion zone and minimal porosity, enabling efficient load transfer and superior bonding quality. More specifically, Tulpan's investigation of Ti64–AlSi9Cu3 IPCs fabricated via the PrintCast method identified a distinct two-layer interfacial structure: as shown in Figure 8(B), one adjacent to the Ti64 lattice composed of nanoscale τ_2 (Ti(Al, Si)₂), and another containing granular (AlSi)₃Ti and α -AlFeSi phases [140]. These phases were formed as a result of localised reactions during solidification and were strongly influenced by lattice topology, with the BCCZ architecture promoting better infiltration and more uniform phase development than the Cubic structure. High-resolution characterisation (TEM, EBSD, SAED) revealed dislocation structures and twin boundaries, suggesting plastic accommodation within the interfacial region, which corresponded to enhanced compressive strength and energy absorption.

Analogously, Nejad et al. examined Mg-7Al-1Ca infiltrated into 3D Cu foam and observed that post-casting heat treatment at 480°C led to significant thickening of the diffusion zone (up to 13 µm) and the formation of intermetallics such as Mg₂Cu, Al₂Ca, and (Mg, Al)₂Ca [52]. These new phases improved fracture toughness by enhancing load transfer and crack path deflection, although a moderate reduction in shear strength was noted due to localised embrittlement. In alternative fabrication routes, such as in the one presented by Lin et al.'s [127], the combination of SLM with hot extrusion yielded strong metallurgical bonding and hybrid nanostructures, while Liu et al.'s [129] in situ foamed-lattice composite leveraged co-solidification and mutual constraint for synergistic mechanical response. Regarding the architected W–Cu IPCs fabricated by Viganò et al. [128] using a space-holder-assisted powder route, the interface was primarily mechanical in nature, with infiltration driven by capillary action and pore connectivity, rather than by diffusion or metallurgical bonding (as shown in Figure 4(D)). The previous findings

underscore the role of the interface in the performance of MM IPCs. Its form and composition are highly sensitive to process-induced parameters, while the lattice geometry can be strategically employed to optimise interfacial bonding and mechanical outcomes.

In CM IPCs, the interface between the brittle ceramic scaffold and infiltrated metal matrix plays a critical role in the mechanical performance. Across several studies, the connection between the two phases is primarily physical, with limited evidence of metallurgical bonding or elemental diffusion at the interface. Microstructural observations commonly reveal the presence of interfacial defects such as microvoids, unfilled regions, and localised debonding. These defects are frequently associated with either incomplete infiltration or mismatches in thermal expansion coefficients between the two phases. For instance, Zhang et al. [147] reported that interfacial failure was the dominant fracture mechanism under compression, with cracks initiating along the ceramic–metal boundary due to cleavage and stress concentration at micropores. The interface of ceramic and metal is shown in Figure 5(B). Matos et al. [152] demonstrated that increased architectural interconnectivity in the ceramic phase improved interfacial coherence, enhancing stress transfer and delaying delamination (see Figure 8(E)). Similarly, Lu et al. [150] observed that enlarging the TPMS cell size contributed to a more continuous metallic phase and improved interface morphology, which in turn led to enhanced resistance to dynamic loading. However, even in geometrically optimised structures, the interface remains the critical site for damage initiation, as reported by Santos et al. [151], where different TPMS topologies affected the distribution and localisation of interfacial strain. Compared to MM IPCs, which often benefit from metallurgical bonding and diffusion zones formed during high-pressure or heat-assisted processing, CM IPCs tend to rely on mechanical interlocking and morphological compatibility for interfacial strength. The absence of intermetallic phases or transitional layers makes them more susceptible to interface-driven fracture. Furthermore, the ceramic scaffolds produced by vat

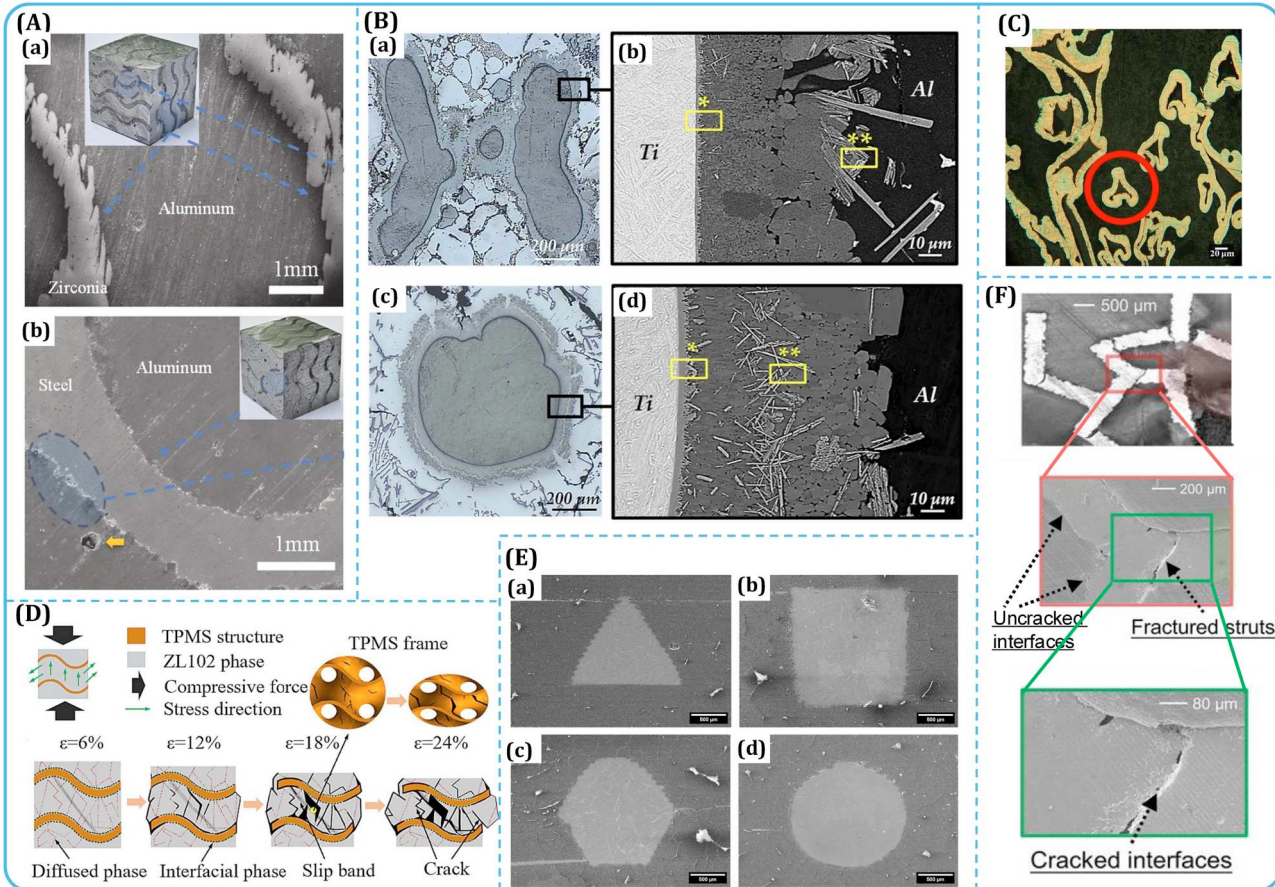


Figure 8. (A) SEM images of aluminium-ceramic (a) and aluminium-steel (b) IPCs by [114] (license number: [6015380023468]). (B) Microstructure of the Ti64 and AlSi9Cu3 IPCs (adapted from [140], license number: [6015380475746]). (a) Cross-sectional micrograph image of IPC-BZ. (b) Magnified image of the interface zone. (c) Cross-sectional image of IPC-C. (d) Magnified image of the interface zone in IPC-C. In the regions denoted by yellow rectangles, TEM lamellae were extracted. (C) Optical microscope images of the cross section of the Cu–Ni shells after the uniaxial compression test [68] (license number: [6015380243067]). (D) The force diagram of structural compression, and the deformation damage mechanism diagram of Ti/Al IPC [130] (license number: [6015380658821]). (E) SEM images for the different aluminium-alumina IPCs: (a) triangular; (b) square; (c) hexagonal; (d) circular [151] (licensed under CC-BY 4.0). (F) Microscopic morphology of metal and polymer interface fracture (adapted from [33], licensed under CC-BY).

photopolymerization methods often exhibit pronounced staircase effects along their printed layers, particularly in horizontal planes. These geometric artefacts can serve as stress risers during infiltration and subsequent loading, further weakening the interface. In contrast, SLM-fabricated metal lattices used in MM IPCs typically display smoother surfaces and reduced layer-induced roughness, allowing for more uniform interfacial contact. Thus, while CM IPCs benefit from excellent geometric tunability and high stiffness contrast, their performance is often limited by the quality and continuity of the interface, which remains a key area for optimisation in future composite design.

In polymer-infiltrated IPCs, the interface between the rigid reinforcement and the soft matrix is predominantly governed by mechanical interlocking and surface conformance, with little or no chemical bonding. Due to the disparity in stiffness and surface energy, achieving

robust adhesion between phases presents a major challenge. In PM IPCs, studies such as Wang et al. [33,162] demonstrate that aperiodic Ti–epoxy structures fabricated via SLM and vacuum infiltration exhibit clear phase separation at the micro-interface, with enhanced performance attributed to geometric complementarity and confined load transfer within the aperiodic truss (as depicted in Figure 8(F)). Singh et al. [156] further show that rough internal features and partially filled gaps along printed ceramic TPMS surfaces promote microscale interlocking with epoxy, enhancing energy dissipation despite the absence of strong chemical bonding. Similarly, in PC IPCs, the interfacial morphology is influenced significantly by the printed topology and post-processing conditions. Ceramic lattices fabricated via FDM and sintered before epoxy infiltration tend to form discontinuous bonding zones, especially at surface nodes where the staircase effect and residual

porosity dominate. Nonetheless, Singh and Karathanasopoulos [157] report that surface-based topologies like spinodal and TPMS geometries, when paired with whisker-enhanced epoxy matrices, yield IPCs with up to 30-fold increases in peak stress compared to their ceramic counterparts, indicating the crucial role of architecture-enabled interface engagement. In contrast, electroformed metal-coated PU foams, as investigated by Jalilzadeh et al. [68], establish stronger interface adhesion due to micrometer-scale diffusion layers and continuous metallic shells, resulting in multilayered foams with superior energy absorption and yield strength relative to single-layer constructs. The dense infiltration and fully infiltrated interlayer is shown in Figure 8(C). Compared to MM IPCs, where metallurgical diffusion and interfacial reaction products are common and facilitate strong phase continuity, the interface in PM and PC IPCs is often the limiting factor for load transfer. Furthermore, due to differences in manufacturing fidelity, the surface staircase effect in polymer and ceramic scaffolds is generally more pronounced than in AM metals, intensifying stress concentrations and local debonding at the interface. Overall, while PM and PC IPCs benefit from lightweight composition and architectural flexibility, their mechanical performance remains highly sensitive to interfacial integrity, which is shaped by surface morphology, infiltration quality, and the compatibility of constituent phases.

5. Mechanical performance

In this section, the mechanical behaviour of a wide range of IPC designs is analysed in detail, including the elastic modulus, yield strength, ultimate strength, and toughness (energy absorption). The relevant mechanical parameters definitions are detailed below (Section 5.1), while the data extracted (Section 5.2) are provided in comparative Ashby-type plots in Section (Section 5.3). A summary schematic of the different IPC fabrication processes is provided in Figure 9(B).

5.1. Constitutive response of architected IPCs

Experimental stress-strain curves (s-s curve) allow for the quantification of key material performance features, including the elastic (E) modulus, yield strength ($\sigma_{0.2}$), ultimate strength (σ_u), and the strain to densification (ϵ_D) or fracture (ϵ_f) [163,164] (Figure 9(A)). It is worth noticing that in cubic symmetry materials, mechanical properties such as tensile and compressive moduli are equal at a given orientation testing, as of the uniformity of their internal structure. The latter ensures that the material's response to stress is consistent, regardless of

the direction of the applied force [165–167]. Apart from single-crystal metals and ceramics, as well as some specially processed materials, most metals and ceramics exhibit an isotropic base material behaviour due to their randomly oriented grains, an attribute that equally applies to amorphous polymers, such as epoxies [168].

In the following section, the mechanical properties of different IPC samples are analysed. In IPCs, the effective composite material performance depends on the uniformity and orientation of the underlying phases. Many IPCs, especially those with random phase distributions, are inherently isotropic. However, specific fabrication methods or intentional phase alignments can result in anisotropic behaviour [143,169,170]. In this context, both microstructural analysis and direction-specific property measurements (e.g. tensile and compressive tests) are crucial, and if the tensile properties of the composites are of interest, tensile test data must be considered, as compressive data alone may not fully capture the mechanical behaviour of these materials. A generalised schematic of the stress-strain curves of ceramic, metal, and polymer materials is shown in Figure 9(A). A few special features are worth noticing before further analysis.

The elastic modulus represents the stiffness of a material, that is its elastic resistance ability to deformation. At the early stage of the stress-strain response, most IPC materials obey the Hooke's law, where their stress is in proportion to the strain values, denoted as $\sigma_e = E\epsilon_e$ (denoted as E in Figure 9(A)). The linear curve part, defining the elastic modulus, also known as Young's modulus (E) [171] is analysed in all cases. By definition, it is calculated by the slope of the curve in the elastic region, before yielding occurs. Notably, accurately determining the Young's modulus of metal matrix composites (MMCs), including IPCs, remains a significant challenge [172]. Conventional tensile testing often underestimates stiffness due to the absence of a clear elastic regime and early onset of microplasticity or damage, especially in heterogeneous systems like IPCs [128,173]. Anisotropy further complicates the process, as full characterisation requires multi-directional testing, which is often impractical due to specimen preparation constraints [174]. To address these issues, non-destructive ultrasonic techniques such as ultrasound phase spectroscopy (UPS) and resonant ultrasound spectroscopy (RUS) have been widely adopted in the characterisation of composites. These methods allow directional elastic constants to be determined without inducing damage and have been effectively used by Roy et al. to extract full stiffness matrices in AlSi12-Al₂O₃ composites [174,175]. However, these

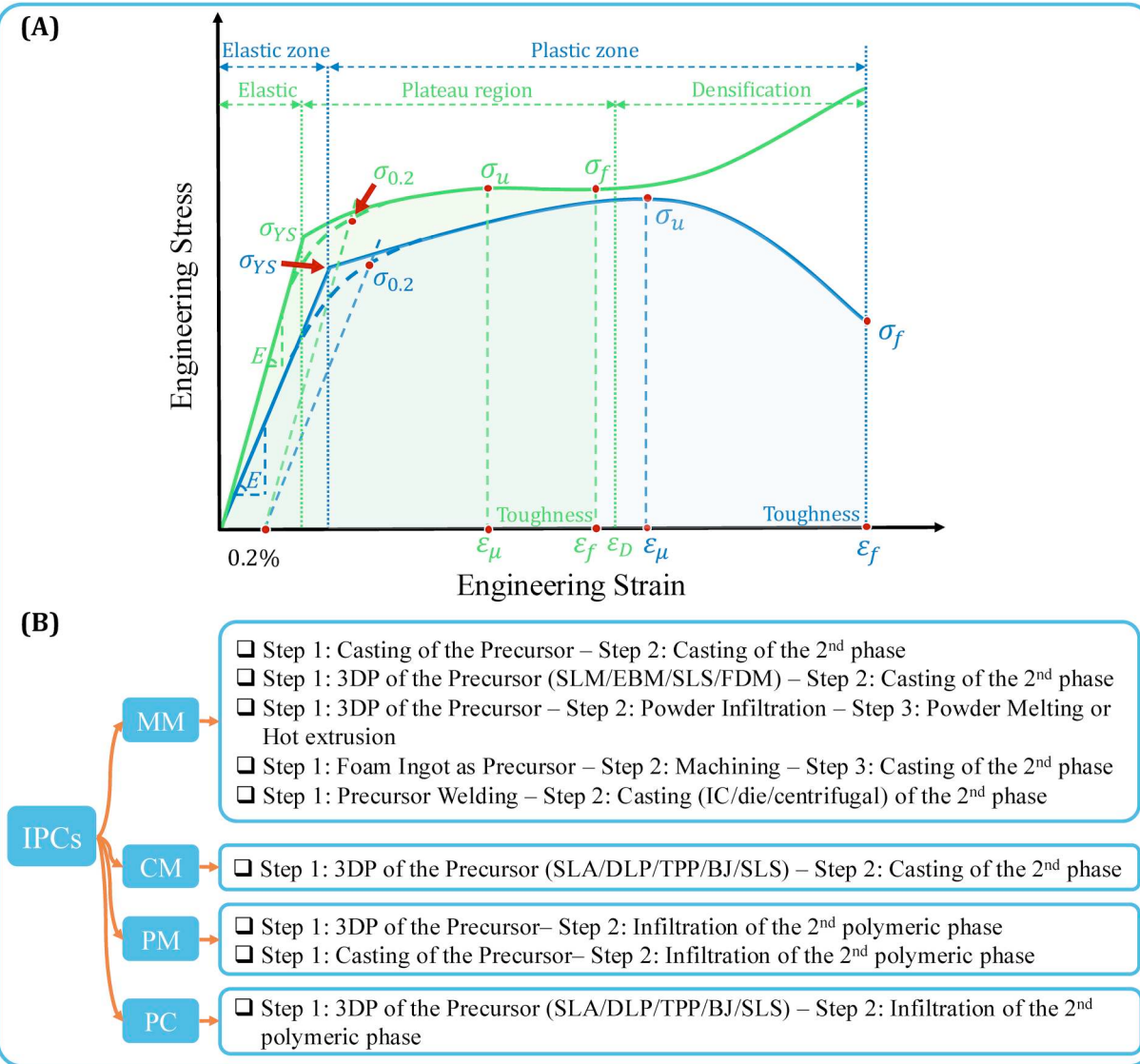


Figure 9. (A) Characteristic stress-strain curve of ductile metal materials [163] in blue, as well as typical stress-strain curve of IPCs with elastic, plateau and densification region in green. The general shape of curve near yield point (σ_{YS}) in realistic testing is drawn with curved blue/green dashed line, on which the yield point is usually difficult to identify clearly. The 0.2% offset method is demonstrated by the straight dashed line paralleling to the linear curve in elastic region. $\sigma_{0.2}$ denotes the 0.2% yield strength, σ_u denotes the ultimate strength, and σ_f represents the fracture strain. ε_D defines the strain at which densification zone starts. (B) A recap and summary of the manufacturing procedure for the 4 categories of IPCs.

techniques are rarely employed in architected IPCs, due to geometric compatibility, sample size limitations, and the non-homogeneous nature of architected structures. Up to now, compressive testing serves as the fundamental testing method for the mechanical assessment of such architected bi-continuous composites [176], with bending or tensile testing data being scarce or utterly unavailable.

The yield strength is the stress at which the material begins to deform plastically, denoted as σ_{YS} in Figure 9(A). It signifies the transition from elastic elastic deformation, where the material can return to its original shape, to plastic deformation, where permanent

changes occur [177]. However, in empirical stress-strain curves, the exact transition from elastic to plastic deformation is often difficult to pinpoint, as the curve typically exhibits a smooth, continuous progression rather than a sharp yield point. This gradual transition, illustrated by the blue and green curved dashed lines in Figure 9(A), reflects the onset of strain hardening, where the material begins to deform plastically while still increasing in strength [178]. For generality, the 0.2% offset method is employed [171]: drawing a line parallel to the linear elastic region and crossing the 0.2% strain x-axis, the intersection point where the offset line meets the stress-strain curve is determined

as the 0.2% offset yield strength ($\sigma_{0.2}$, orange dashed line and intersection red dots in [Figure 9\(A\)](#)). In most of the compressive stress-strain curves evaluated, the yield strength values were identified by the 0.2% offset method, unless the specific value was mentioned in the paper. The toughness refers to a material's ability to absorb energy and plastically deform before fracturing [46]. It is typically quantified as the total area under the stress-strain curve up to the fracture point and is influenced by both strength and ductility. In contrast, energy absorption (EA) often refers to the area under the stress-strain curve up to a specific point of interest, such as the densification point in porous or composite materials, as highlighted in [Figure 9\(A\)](#). While toughness is a fundamental material property, EA is more application-specific. To normalise for mass and enable fair comparison across materials with different densities, specific energy absorption (SEA) is used, representing the absorbed energy per unit mass.

The ultimate compressive strength, denoted as σ_u in [Figure 9\(A\)](#), refers to the stress level associated with failure following initial yielding. It typically represents the onset of fracture or irreversible deformation, but does not necessarily correspond to the global peak stress in the stress-strain curve. In IPCs exhibiting ductile responses, the stress-strain curve often follows a three-stage deformation pattern: an initial elastic region, a plateau phase where deformation progresses at relatively constant stress, and a final densification region marked by a steep rise in stress due to hardening and localised failure mechanisms [179–181]. In this context, σ_u is typically identified as the maximum stress in the plateau region, occurring just before the densification phase begins, by which point significant internal plastification or localised failure has already taken place.

This three-stage stress-strain behaviour is initially observed in architected materials such as lattices, foams, and hierarchical structures [182]. Oscillations in the plateau region are commonly attributed to layer-by-layer collapse, indicating brittle features and localised shear band formation [183–185]. In contrast, a smooth and stable plateau suggests the presence of distributed plastic deformation, which enhances the material's ability to deform and absorb energy [186]. However, it is important to note that not all IPCs conform to this idealised three-stage pattern. This variability will be further explored in subsequent sections and summarised in [Tables 6,7, and 8](#). Furthermore, the densification in lattice-based structures is typically associated with the collapse of macroscopic pores, leading to a rapid stress increase once structural compaction is complete [192]. Similar behaviour is observed in porous IPCs, particularly

those incorporating foam architectures. In contrast, fully dense IPCs undergo densification through different mechanisms, such as phase interface sliding, localised plasticity, or the progressive collapse of microstructural features [53]. These transitions reduce internal compliance and lead to a change in deformation behaviour, often manifested as an upward curvature in the stress-strain curve (as depicted in [Figure 9\(A\)](#)). As such, the presence, onset, and nature of densification are highly system-dependent, shaped by the material phases, their interactions, and the architecture of the composite.

Overall, IPCs leverage the complementary attributes of their constituent phases, often achieving higher elastic modulus and yield strength than ductile metals through load-sharing and phase constraint effects, though typically at the cost of reduced fracture strain. It should be emphasised that the stress-strain curves presented here are illustrative of commonly observed trends in many IPC systems, but they are by no means universal. The mechanical response of IPCs varies widely depending on the specific combination of phases, interfacial bonding quality, architecture, porosity, and loading conditions. For example, high-performance ceramics may still surpass IPCs in absolute stiffness, and polymers may offer superior flexibility or ease of processing. Moreover, the sequence of densification and fracture is system-dependent: in porous IPCs or those with foam-like architecture, densification typically precedes fracture as voids collapse under loading [154]; whereas in stiffer, brittle-rich IPCs, fracture may occur before any noticeable densification [147,150,193]. These variations must be considered when interpreting stress-strain behaviour and comparing IPCs with monolithic materials. The curves provided should therefore be seen as indicative examples rather than general rules.

While rule-of-mixture (RoM) models are commonly used to estimate the effective mechanical properties of composite materials, they exhibit notable limitations when applied to architected IPCs. In such systems, the mechanical response is not solely governed by constituent material properties and phase volume fractions, but also by the designed geometry, interfacial effects, and local deformation modes. Studies have shown that architected IPCs often display significantly reduced stiffness and strength compared to RoM predictions, due to bending-dominated architectures, non-uniform stress paths, and early deformation localisation. For instance, Bauer et al. demonstrated that gyroid-based Cu–C IPCs exhibited elastic properties far below those expected from conventional mixture models [148]. Similarly, high-strength metallic lattices could show substantial mechanical softening due to geometric effects [194]. These observations highlight the need for alternative

Table 6. Summary of the physical and mechanical behaviours of MM IPCs. In column 3, materials are listed in the format of 'architected reinforcement lattices + infiltrated materials' (e.g. samples of No. 1–5 are Gyroid tungsten scaffolds infiltrated with melted copper). In column 5, ρ^* represents the density calculated by RoM. In the column of critical strain (%), data is listed in the format of 'densification strain (fracture strain)'. Unavailable values are denoted by '-'.

No.	Cell Type	Materials	Sample Size(mm)	ρ^* (g/cm ³)	E (GPa)	YS (MPa)	UCS (MPa)	Critical Strain (%)	SS (MPa/g)	SEA (kJ/kg)	Ref.
1	Gyroid	W+Cu	$(\pi/4) \times (12.6)^2 \times 10$	16,000	7.6	626	883.37	-(35)	14.64	44.28	[187]
2				15,800	6.9	440	728	-(35)	36.95	12.06	
3				15,700	6.1	400	668	-(35)	34.12	10.67	
4				15,600	5.6	380	636	26(35)	32.7	7	
5				15,500	6.3	359	532	20(35)	27.53	4.61	
6	Cubic	W+Cu	$10 \times 10 \times 10$	13500	9.6	560	662	28(54)	196.15	10.47	[188]
7	RD			13,500	10.5	191.3	985.5	30(71)	292	7.66	
8	BCC	316L+Zr	$10 \times 10 \times 6$	7519	3.54	646	1980	-(47)	776	87.11	[132]
9	FCC			7519	10.13	703	1205	29(34)	472	38.83	
10	HCP			7519	23.7	845	1254	-(31)	492	48.45	
11	RD	NiTi+Mg	—	3210	4.6	80	320	33(51)	154	31.15	[131]
12	BCC	Ti64+AlSi9Cu3	$10 \times 10 \times 10$	4185.5	2.8	293.1	345.8	29(50)	13	17.71	[140]
13	Cubic			4088	3.6	202	231	27(50)	11	13.37	
14	Honey-comb	Al-Mg-Mn-Sc-Zr +Al ₈₄ Ni ₇ Gd ₆ Co ₃	$(\pi/4) \times (5)^2 \times 135$	3057.2	25.3	745	1158	-(30)	8933	97.62	[127]
15				3057.2	22.9	629	1150	-(40)	8872	112.59	
16				3057.2	24	542	1078	-(40)	8316	104.97	
17	Machined Foam	Al+ZL111	$60 \times 60 \times 60$	910	0.793	20	26	40(60)	0.12	9.88	[129]
18				1220	1.204	30	40	40(60)	0.19	11.42	
19				1440	1.453	44	68	41(60)	0.31	15.99	
20				1770	2.172	82.35	106.62	42(58)	0.49	19.53	
21	Gyroid	Ti64+ZL102	$10 \times 10 \times 25$	3816	6.15	305	420	-(25)	168	20.91	[130]
22	OB	Ti+Mg	$1 \times 1 \times 1$	2570	11.07	184.8	427.11	-(25)	2e5	29.83	[189]
23	Wire mesh scaffold	Ti64+Zr-based metal glass	$3 \times 3 \times 6$	7050	84.8	1537	1537	-(2)	3e4	2.46	[51]
24				7050	76.2	1261.4	1609	-(4)	3e4	5.29	
25				7050	74.3	1410	1555.3	-(3)	3e4	4.21	
26				7050	64.6	1383	1619.4	-(11)	3e4	20.51	
27	Gyroid	316L+AlSi10Mg	$10 \times 10 \times 10$	2452	4.28	187.2	500	-(40)	85.73	50.86	[114]

Table 7. Summary of the physical and mechanical behaviours of CM IPCs.

No.	Cell Type	Materials	Sample Size(mm)	ρ^* (g/cm ³)	E (GPa)	YS (MPa)	UCS (MPa)	Critical Strain (%)	SS (MPa/g)	SEA (kJ/kg)	Ref.
1	Gyroid	Al ₂ O ₃ +Al-Mg-Si	$20 \times 20 \times 20$	3575	36	231.44	259.5	-(3)	9.07	0.94	[147]
2	Gyroid	Al ₂ O ₃ + AlSi10Mg	-	3075	2.4	112	188	30(60)	61.13	19.28	[150]
3				3075	2.6	82	170	38(55)	11.25	17.54	
4				3075	1.9	87	100	38(55)	2.35	8.64	
5	Primitive	Bison High Al ₂ O ₃ Resin + AlSi12(Fe)	$15 \times 15 \times 15$	2745	2.6	172	261	24(50)	41.07	16.88	[151]
6	Diamond			2745	2.8	175	290	30(50)	45.64	23.81	
7	Gyroid			2745	2.7	172	291.4	29(50)	45.86	24.55	
8	Triangular Channel	Bison High Al ₂ O ₃ Resin + AlSi12(Fe)	$15 \times 15 \times 15$	3494	2.5	180	203	24(50)	58.1	10.44	[152]
9	Hexagonal Channel			3501	2.6	188	217	21(50)	62	9.9	
10	Circular Channel			3436	3.1	196	220	23(50)	64.03	12.24	
11	Square Channel			3320	2.8	189.82	225.81	23(50)	68.02	12.82	
12	Foam	A356+AlN	$6 \times 6 \times 6$	3165.6	3.61	130	140	30(56)	229	12.94	[190]
13	Rectangular	Ti6Al4V + CaSiO ₃	$(\pi/4) \times (20)^2 \times 15$	3271.7	3.3	250.31	383.55	-(12)	87.67	6.28	[149]
14	Honeycomb			3271.7	2.2	124.3	143.41	9(12)	26.68	2.09	
15	Primitive			3371.8	1.7	140.57	158	12(39)	24.78	2.88	
16	Gyroid			3400.4	1.3	93.91	107	25(52)	14.51	4.76	
17	Gyroid	Pyrolytic carbon + Ni	$5 \times 5 \times 5 \times 10^{-3}$	5300	28.8	2700	3450	32(50)	1e11	161.18	[148]
18	Gyroid	ZrO ₂ + AlSi10Mg	$10 \times 10 \times 10$	3670	4	198.55	223.19	39(49)	38.27	21.21	[114]

Table 8. Summary of the physical and mechanical behaviours of polymer-based IPCs (PM and CM included).

No.	Cell Type	Materials	Sample Size(mm)	ρ^* (g/cm ³)	E (GPa)	YS (MPa)	UCS (MPa)	Critical Strain (%)	SS (MPa/g)	SEA (kJ/kg)	Ref.
1	Modified Aperiodic Lattice	Ti6Al4V+Epoxy	25 × 25 × 25	1542	1.33	94	110	48(60)	4.64	31	[33]
2				1751	1.28	111	123	36(60)	4.56	20.96	
3				1953	1.9	122	150	29(60)	4.99	18.95	
4				2255	2.59	175	200	45(60)	5.76	33.44	
5	BCC	Ti6Al4V+PEEK	10 × 10 × 10	1930	1.66	137	201.7	40(70)	104	33.52	[191]
6				3180	5.2	560	660	-(20)	207	22.26	
7	Metal-coated PU foam	Polyurethan + Cu/Ni	-	977	0.05	4.084	4.07	15(47)	0.2	0.3	[68]
8				657	0.04	2.869	2.87	16(66)	0.18	0.76	
9	BCC	AlSi10Mg+epoxy	25 × 25 × 25	1566.1	2.51	120.01	131.62	29(50)	17.85	19.23	[157]
10	Gyroid			1566.1	2.66	148	164.5	17(50)	19.64	12.61	
11	IWP			1566.1	2.98	151.8	172	10(50)	18.35	6.85	
12	Spinadol			1566.1	2.94	141.69	153.4	20(50)	14.79	15.38	
13	Gyroid	Zirconia ceramic +epoxy	24 × 24 × 24	2010.4	1.88	94.4	97.83	26(50)	8.6	6.74	[156]
14	IWP			2010.4	2.07	99.3	100.75	30(50)	8.14	9.51	
15	Primitive			2010.4	1.81	84.24	88.21	-(50)	6.6	9.15	
16	Spinadol			2010.4	1.98	101.93	105.3	40(50)	7.33	9.35	

approaches, such as geometry-informed modelling or numerical simulation, when predicting the mechanical behaviour of architected IPCs. A more detailed quantitative comparison of their mechanical responses is provided in the following sections.

5.2. Mechanical performance of MM, CM, PM and PC IPCs

Summarizing information on the design and performance of MM, CM, PM and PC IPCs is provided in **Tables 6,7**, and **Table 8**. The data including geometric properties, such as the cell type, the materials, the sample sizes, and densities, along with effective mechanical response metrics for the elastic modulus (E), yield strength (YS), compressive strength (UCS), critical strain (densification strain and fracture strain), specific strength (SS), and specific energy absorption (SEA). The critical strain provides data both for the onset strain of densification and the fracture strain. Notwithstanding, in different works, the densification region persists until the end-of-test strain, typically ranging between 30% to 60%. In such cases, the fracture strain is denoted in italicised font to indicate an end-of-test strain, rather than the actual fracture strain.

In terms of physical properties, the lattice structures encompass a wide range of designs, from 2D cellular architectures (e.g. honeycomb, channels, etc.) and machined-cut foams to 3D architected strut-based structures (e.g. BCC, FCC, etc.), TPMS structures (e.g. Gyroid, primitive, diamond, etc.), self-organised periodic spinodal structures, as well as aperiodic, orthogonal branching, and wire mesh scaffolds.

In metal-metal IPCs, a wide variety of aluminium alloys have been used, mainly due to their excellent

balance of strength and ductility combined with their lightweight nature [151]. Similarly, ductile and conductive metals such as copper have been frequently used as one phase in IPCs. These metals are typically paired with lighter, high-strength materials such as titanium alloys such as Ti-6Al-4V to balance ductility, strength, and stiffness, enabling the design of composites with tailored mechanical performance within a target density range. In CM IPCs, Al₂O₃ alumina is the most extensively studied material. It is usually infiltrated with aluminium alloys to form stiff and strong composites with enhanced energy absorption capacities. In addition, other ceramic materials such as AlN and CaSiO₃ have been investigated. For PM and PC IPCs, epoxy is a widely used infiltration material, paired with a spectrum of metals or ceramics. Among all classes of IPCs samples, cube dimensions typically range from 1³ mm³ to 25³ mm³, with two extreme cases as small as the nanoscale of 5 m and as large as 60³ mm³. The dimensions of cylindric samples span a broad range, the associated sample volumes to vary from approximately 1246 to 4710 mm³.

The density of MM IPCs overall contains higher values compared to CM and PM or PC IPCs. Exceptional densities exceed 10,000 kg/m³ in IPCs paired with tungsten (W), whose intrinsic density is as high as 19,300 kg/m³. In contrast, Al + ZL111 alloy IPCs with hollow metal foam lattices feature much lower densities, ranging from 910 to 2000 kg/m³ (**Table 6**). Ceramic-metal IPCs, have a rather narrow density bandwidth for the investigated material phase combinations, typically ranging in-between 2700 to 3400 kg/m³ (**Table 7**). Polymer-based PM IPCs show significantly lower densities, generally between 1542 and 2010.4 kg/m³. An exception is seen in metal-coated PU foam samples, which have unusually low densities of 657 and 977 kg/m³ (**Table 8**).

Mechanical responses vary over a wide range and are influenced by a combination of factors which include the reinforcement phase topology and the underlying phase combination. Among MM IPCs (Table 6), the elastic modulus ranges from 0.793 GPa for machined metal foam IPCs to an extraordinary 84.8 GPa for Ti64 + Zr-based metal glass wire mesh IPCs. The yield limit of IPCs accordingly vary from 20 to 1537 MPa, while ultimate compressive strength values as low as 26 MPa and up to 1980 MPa have been reported. With respect to the critical strain, it can be noticed that not all architected IPCs exhibit a distinct plateau and densification region. In certain cases, the stress-strain curves continue to increase in an almost linear manner after the elastic region until fracture occurs. For samples with exceptional ductility metrics, even beyond the recorded strain ranges (denoted by italicised numbers in the tables), exceptional energy absorptions are reported. In particular, specific energy absorption values as low as 2.46 kJ/kg and up to 112.59 kJ/kg for a hard Ti64 and Zr-based metal glass IPC are reported.

In CM IPCs (Table 7), most of the elastic modulus values are in the single-digit range, ranging from 1.3 to 3.61 GPa. Nonetheless, the samples studied by Zhang et al. [147] achieve an exceptional value of 36 GPa. Yield strength values are in the range of 82 and 250.31 MPa, while ultimate compressive strength values lie between 100 and 383.55 MPa, which are overall lower than those recorded for MM IPCs. Unlike MM IPCs, most CM IPC samples exhibit a clear densification zone at strains ranging from 2% to 38%. Specific energy absorption values range from 0.95 to 51.01 kJ/kg. For polymer-based IPCs (Table 8), although their elastic modulus and strength properties are inferior to MM and CM IPCs, their energy absorption capacities remain significant, with their SEA to range from 5.21 to 67.11 kJ/kg. It is also worth noticing that, in most cases, densification occurs at low or moderate strain magnitudes, resulting in a long densification region before fracture.

5.3. Comparative metrics: Ashby plots

5.3.1. Young's modulus

In certain applications, such as aerospace and automotive industries, materials exhibiting both optimal stiffness and lightweight properties are sought for [195,196]. Elevated elastic modulus values indicate a material that is stiffer and exhibits reduced deformation under stress. Consequently, a stiffness-to-weight ratio index is proposed to evaluate and select materials that provide the necessary qualities [197]. The ratio of elastic modulus (E) to density (ρ), represented as $\frac{E}{\rho}$ and

referred to as specific modulus, is a critical parameter in material selection for applications that require weight reduction while preserving stiffness. It is also an outstanding criterion when considering material substitution [198] and topology optimisation (TO) [199]. An elevated $\frac{E}{\rho}$ value signifies that a material can get the required stiffness upon reduced mass, resulting in advantages such as enhanced fuel efficiency, augmented load capacity, and superior performance [200]. Ashby diagrams [182,201–203] provide unique insights into the comparative performance of materials over a wide range of densities, their significance is well-established for a series of applications [204]. In this context, the elastic modulus versus density for IPCs of different categories on an Ashby plot effectively integrates stiffness and weight considerations into a unified visual framework. This approach simplifies material screening and selection, as the plotted indices highlight the specific modulus and stiffness-to-weight ratios, making comparisons intuitive and straightforward, as summarised in Figure 10(A).

In Figure 10(A), MM IPCs are denoted in red, CM in blue, while PM and PC in green. Samples from various contributions are represented by distinct symbols, as illustrated in the legend. Regarding the clustering of the data, MM IPCs encompass an extensive area, with samples fabricated from aluminium foam ingot and ZAl-Si9Cu2Mg alloy (ZL111) yielding the lowest modulus [129]. This is mostly attributed to the hollow structures of the final samples resulting from the metal foam ingot matrix, in contrast to samples from other studies that exhibit nearly complete infiltration with no visible and macroscale porous structures. Furthermore, owing to this hollow architecture, they demonstrate the lowest density, with exceptional lightweight characteristics. In the other extreme, Gyroid tungsten and copper IPCs [187] yield the highest density among the MM IPCs investigated, due to the high density of monolithic tungsten (19,300 kg/m³ in theory, 18,600 kg/m³ in experiment). The highest elastic modulus is reported for 304 steel (AISI 304) and zirconium-based metallic glass IPCs [51], achieving 64.6 to 84.8 GPa upon a density of 7050 kg/m³. The outstanding results can be attributed to the integrated effects of the high monolithic modulus of both 304 steel and Zr-based metallic glass (193 to 200 GPa, and 89 to 94 GPa, respectively [205]), strong metallurgical bonding and optimised microstructure derived from the high-pressure die casting process, as well as the robust continuous metal mesh skeleton phase within the metal glass matrix.

Analysing the material against the guidelines of $\frac{E}{\rho}$, $\frac{E^{1/2}}{\rho}$ and $\frac{E^{1/3}}{\rho}$, the 304 steel + Zr-based MG IPCs demonstrate superior performance, making them promising

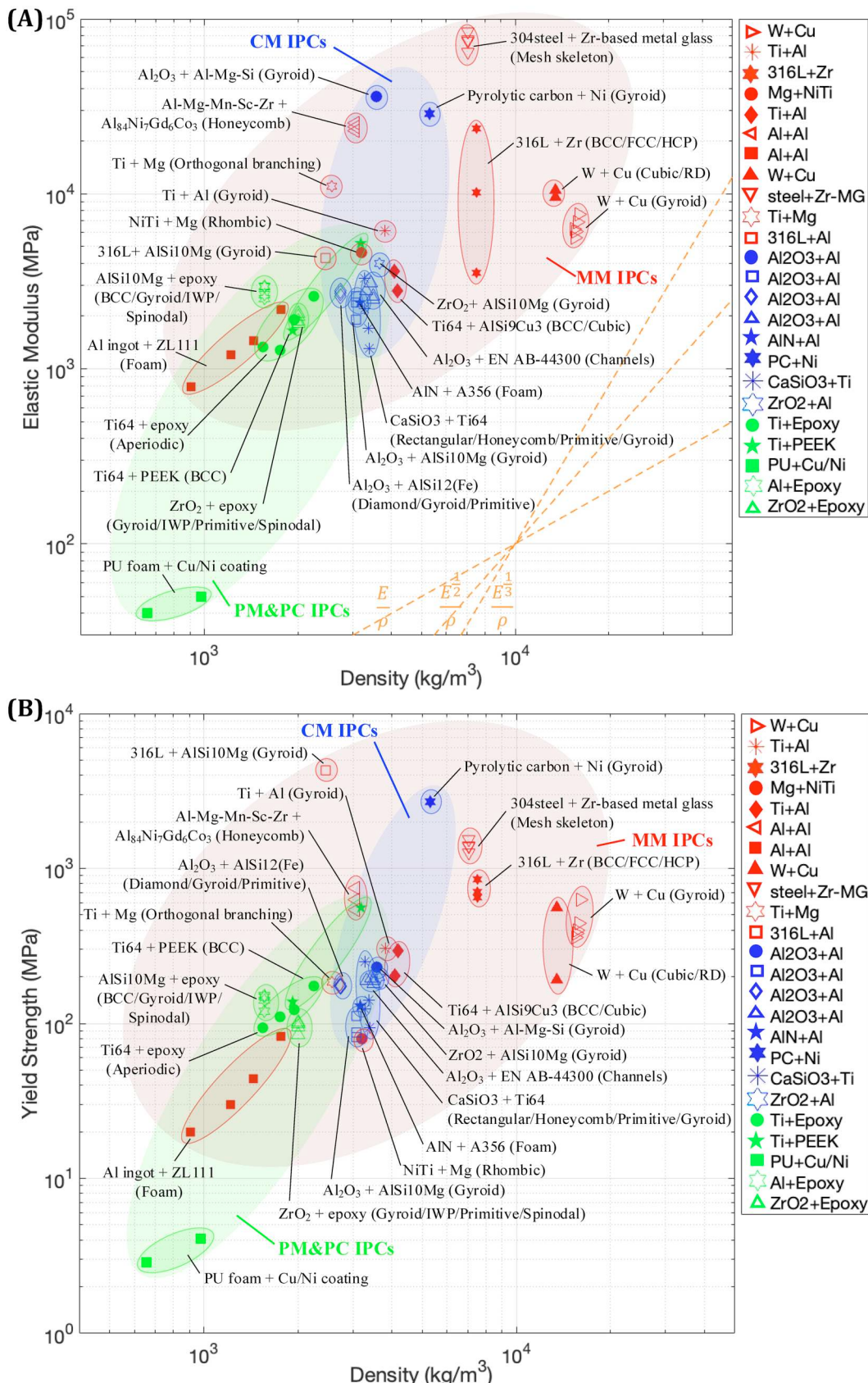


Figure 10. The Ashby plot of (A) elastic modulus (MPa) and (B) yield strength (YS) with respect to density (kg/m^3) of IPCs in log-log scale. The data in Tables 6,7 and 8 is utilised here. The legend gives the simplified material combinations, where the detailed materials and scaffold topologies are denoted in the plot. MM IPCs are represented in red, CM in blue, PM and PC in green.

candidates for lightweight, high-stiffness applications. Moreover, Al + Al alloy hot-extruded IPCs [127] also achieved a significant modulus of 25.2 GPa with a density of approximately 3000 kg/m³, a combination that in normalised stiffness-to-weight ratio terms constitutes an excellent candidate for high stiffness and low weight applications. Notably, the three samples with different matrix structures fabricated by Zhai et al. [132] exhibited significant differences in their mechanical behaviours. The primary factor underlying these differences is the variation in structural stress concentration among the matrix structures. Their analysis revealed that close-packed hexagonal (HCP) structure accommodates higher stresses and deformation compared to FCC and BCC structures. In contrast, the BCC lattice shows lower stress concentrations, enabling greater deformability before cracking, which contributes to its higher plasticity and outstanding elastic modulus. These findings highlight the sensitivity of both deformability and deformation resistance to matrix structure design.

Contrary to the wide area of MM IPCs, CM IPCs occupy a rather narrow space (blue ellipse area in Figure 10), representing a narrow distribution of densities in the range of 2745 to 5300 kg/m³. While the elastic modulus of samples from most of the studies cluster around 2 to 4 GPa, two outliers are reported with elastic moduli of 36 GPa [147] and 28.8 GPa [148], denoted by solid blue circle and hexagram markers, respectively. The former is primarily attributed to the high volume fraction of the ceramic phase in the samples, which approach 70%, with Al₂O₃ ceramic materials to be well-established for their exceptional elastic modulus, which exceeds 300 GPa. The latter is predominantly due to size-dependent strengthening at nanoscale, which is also known as the ‘smaller is stronger’ effect, where reducing dimensions limits defect formation, leading to enhanced mechanical properties [206–208]. In contrast, the Al₂O₃-Al alloy samples reported in other studies ([150–152]) contain ceramic phases ranging from mere 14.57% to 49.6% by volume, resulting in comparatively lower elastic moduli. The Young’s modulus of the unique IPC, engineered with a pyrolysis carbon matrix and nickel-reinforced infiltration (with a volume ratio of nickel to carbon of 52/48), is lower than what a rule of mixture principle would predict. Jens et al. [148] ascribed the low values recorded to sample-plate misalignments, weak interfacial bonding between the inner phases, and residual porosity. It was also observed that pyrolytic carbon typically exhibits a significantly lower Young’s modulus compared to nickel. Their sample achieved a remarkable modulus value among MM, CM and PM

IPCs, without compromising deformation characteristics. This result will be further elaborated in the subsequent section.

PM and PC IPCs (Table 8) mostly occupy mediocre elastic modulus and low-density regions. For instance, Jalilzadeh et al. [68] fabricated metal-coated polyurethane (PU) open-cell foam samples with elastic moduli ranging from 0.04 to 0.05 GPa and density of 657 and 977 kg/m³, respectively. In comparison, studies with titanium alloy (Ti-6Al-4V) precursors infiltrated with epoxy [33] and polyetheretherketone (PEEK) [191] leverage the intrinsically high elastic modulus of Ti-6Al-4V, demonstrating substantially higher elastic moduli. In Chen’s study [191], samples with strut diameters of 477 and 829 m attained elastic moduli of around 1.67 and 5.2 GPa, respectively, with densities of 1930 and 3180 kg/m³, indicating enhanced deformation support with thicker reinforcement phase struts.

5.3.2. Yield strength

While the elastic stiffness is an indicator of the yield strength of metals and polymers, the actual yield strength value of IPC can vary, depending on the underlying phase combinations. The relative information is of primal importance in engineering and material science, as it characterises the permissible load magnitudes before permanent deformation takes place [209]. The Ashby plot with regards to yield strength and density of the 3 categories is provided in Figure 10(B). The clustering pattern resembles the one recorded in the elastic modulus versus density plot (Figure 10(A)). MM IPCs span the widest region, while PM and PC IPCs are concentrated in the low-density area, while CM IPCs are tightly gathered, except for the aforementioned nano-scale pyrolytic carbon + Ni IPCs. The latter reports a yield strength of 2700 MPa, that is the highest value recorded in the entire yield space, essentially due to scale effect and manufacturing innovation. Similar to the elastic modulus, the yield strength of MM IPCs is profoundly influenced by the material combination, reinforcement topology, and phase content, leading to a dispersed distribution in the plot. In contrast, CM, PM, and PC IPCs generally exhibit yield strength within the range of 80 to 250 MPa, with no distinct variations in density. For PM and PC IPCs, the outlier with an extraordinary 560 MPa can be attributed to the high content of Ti64 phase (70%), whereas the low-strength outliers (PU foams + Cu or Ni coating by Jalilzadeh et al. [68]) result from the different coating structure from the rest of the IPCs.

It can be concluded that, the yield behaviours of MM IPCs can be flexibly modified by materials and topology

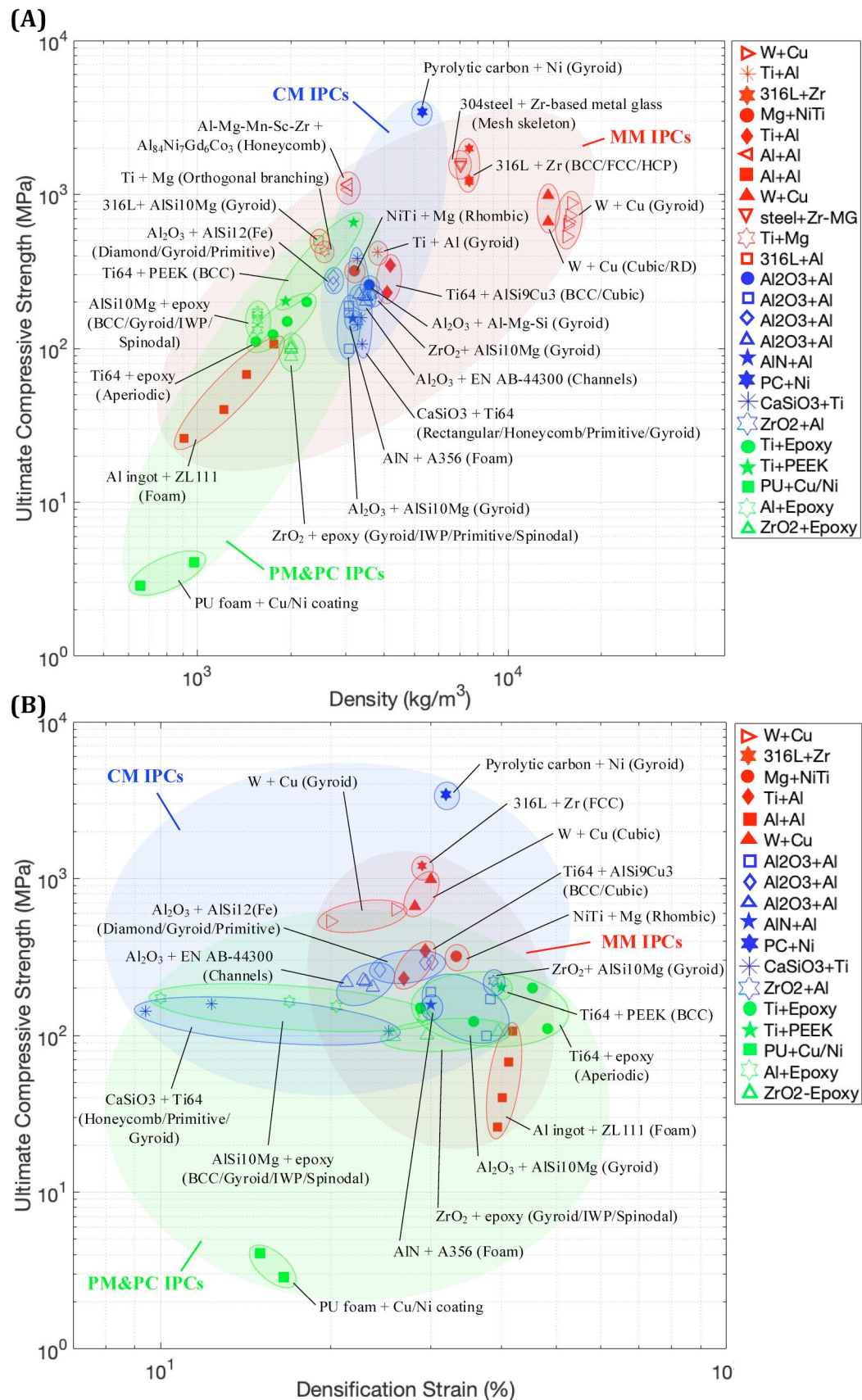


Figure 11. The Ashby plot of ultimate compressive strength (MPa) versus (A) density (kg/m^3) and (B) densification onset strain (%) of IPCs in log-log scale.

designs, and excellent yield strength can be derived at various density regions. On the other hand, CM, PM and PC IPCs exhibit moderate and clustering yield strength, while their behaviours are also tuneable by design.

5.3.3. Ultimate compressive strength and Densification strain

The relationship among the compressive strength and density of IPCs across various categories is also depicted in Figure 11(A). Compared to other material properties such as density, the rule of mixtures does not here apply, out of the unique interfacial characteristics, inherent material heterogeneity, and the effects of the inner interpenetrating phase topological design [181,210]. IPCs engineered with 316L stainless steel and Zr metal glass achieved UCS values ranging from 1200 to 1980 MPa [51]. Notably, the typical UCS for 316L stainless steel and zirconium ranges between 200 to 400 MPa [132]. The significant enhancement is attributed to the diffusion between the two phases at the interface, forming a robust bond that imparts high strength. Additionally, the architectural structures of BCC, FCC, and HCP effectively dissipate stress and therefore enhance the overall compressive strength. Among other MM samples, the hot-extruded Al + Al honeycomb IPCs [127] can be categorised as lightweight and high-strength materials. In contrast, Al + Al foam samples [129] show the lowest strength and energy absorption among MM IPCs, primarily due to the inherent characteristics of the foam structures, as previously discussed. Figure 11(B) illustrates the relationship between ultimate compressive strength and critical densification strain. It should be noted that not all of the IPCs exhibit distinct plateau regions and densification regions, so that only a subpart of the dataspace previously reported is presented in the plot. The majority of the investigated IPCs densify at strain magnitudes between 20% to 50%, with MM IPCs to occupy the narrowest area. The IPCs of honeycomb CaSiO₃ + Ti64 [149] and IWP AlSi10Mg + epoxy [157] exhibit the earliest densification, starting from 6 and 10% of strain, respectively.

Regarding CM IPCs in Figure 11(A), the compressive strength cluster is relatively small and concentrated within the range of 100 and 260 MPa, representing a significant reduction from the intrinsic strength of ceramics, which is typically between 2000 to 4000 MPa. This suggests that the strength of ceramic IPCs is predominantly influenced by the interface strength, rather than the intrinsic strength of the individual phases or the structural design. Figure 11(B) reveals minimal variations between samples with differing structures and volume fractions of alumina ceramic and aluminium alloy IPCs

(among [147,150–152]), whose densification onset strain is in the range of 21% to 38%. In contrast, the outliers of CaSiO₃ + Ti64 IPCs report densification strains of 9 to 25 MPa. Therefore, the densification onset strain for CM IPCs is material sensitive. An early-onset densification strain signifies faster close-up of the macroscale pores and quicker collapse of the inner structures, induced by varying stiffness and energy absorption capacity of IPCs [211]. Due to the small densification strain, CaSiO₃ + Ti64 IPCs exhibit a comparably low specific energy absorption among CM IPCs (in Figure 12).

As for PM and PC IPCs, their compressive strength is typically lower than what a rule of mixture estimate would suggest. Compared to MM IPCs, this difference could be attributed to the weak interfacial bonding between polymer and metal phases, resulting in reduced strength values. Nonetheless, they overall maintain relatively substantial values, above 100 MPa, with the exception of metal-coated PU foams [68]. Although not within the main scope of this review, recent studies on PP IPCs fabricated via multi-material printing have demonstrated notable mechanical performance. For instance, Song et al. [158] reported compressive strengths of up to 84 MPa and specific energy absorption (SEA) values reaching 24.6 J/g in PolyJet-printed TPMS structures. Wang et al. [159] achieved tunable stiffness and toughness by adjusting volume fractions in dual-FDM printed PLA/TPU IPCs, with SEA values exceeding 17 J/g, illustrating strong synergistic behaviour between phases.

5.3.4. Specific energy absorption

The Ashby plot of SEA versus density is provided in Figure 12. Similar to the elastic modulus and yield strength density plots, MM IPCs span a dominant region, with a relatively lower span along the energy scale, compared to their horizontal density distribution axis. The highest SEA among MM samples was achieved by Lin et al.'s hot-extruded Al-Al alloy IPCs [127], with values ranging from 97.62 to 112.59 kJ/kg. These exceptional results are primarily attributed to the heterogeneous structure of the samples, which consist of a hard nanostructured zone and a soft lattice zone. Compared to casting infiltration, hot extrusion resulted in strong interfacial bonding, high densification, and confinement effects, suppressing premature brittle fracture and promoting uniform stress redistribution. These features collectively enhance the composite's energy absorption capacity while maintaining structural integrity. Moreover, 316L stainless steel and zirconium are renowned for their high ductility, enabling substantial deformation before fracture, resulting in excellent

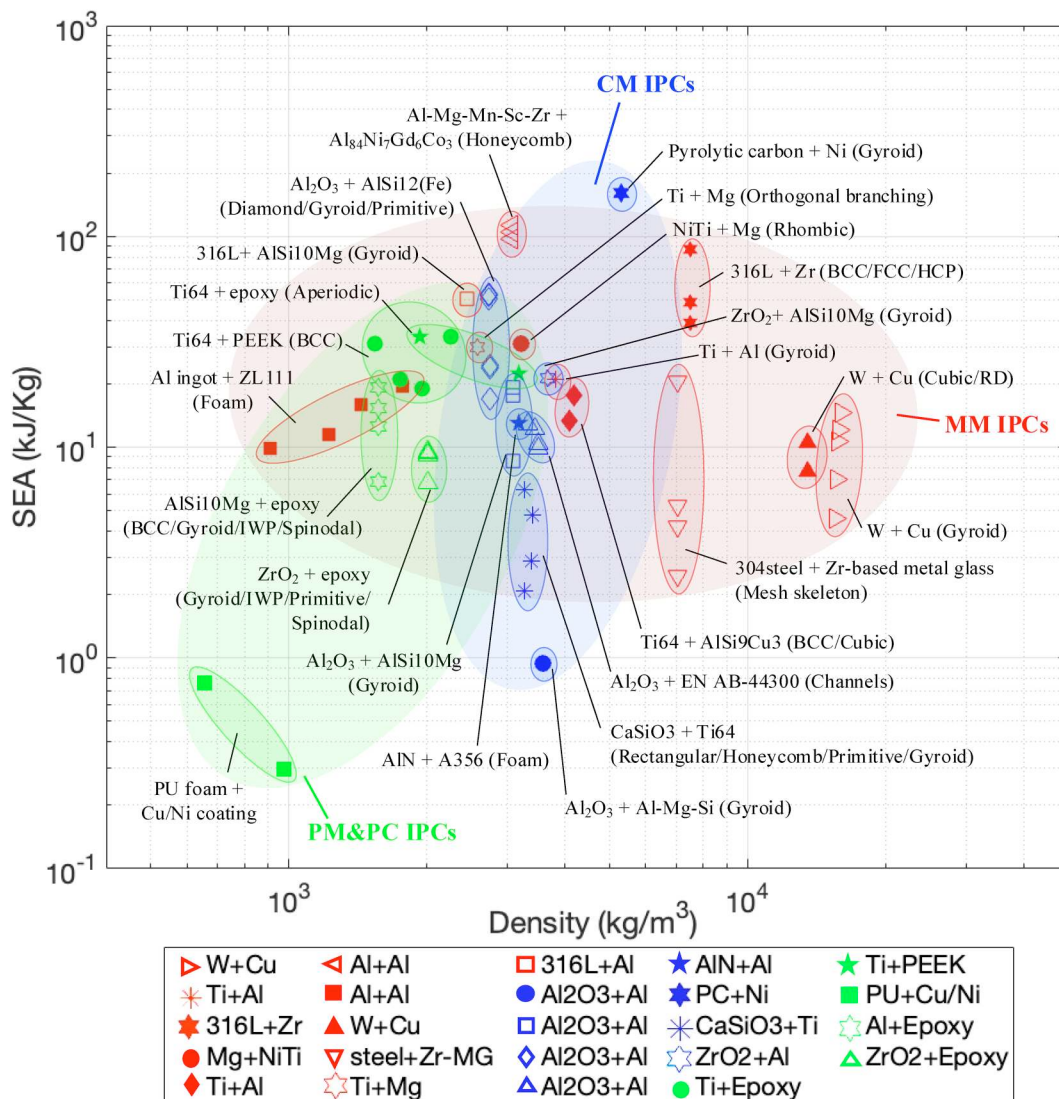


Figure 12. The Ashby plot of specific energy absorption (SEA, kJ/kg) versus density (kg/m³) of IPCs in log-log scale.

energy absorption [212–215]. Zhai et al.'s 316L + Zr IPCs demonstrated an energy absorption of 655 MJ/m³ for BCC sample, corresponding to an SEA of 87.11 kJ/kg. In contrast, the SEA values of FCC and HCP samples were 38.83 and 48.45 kJ/kg, respectively. Those inferior results are also attributed to the differing stress concentration behaviours inherent to their lattice structures.

Regarding W + Cu IPCs, tungsten's brittleness limits the composite's ability to absorb energy through plastic deformation. While copper adds ductility, its lower strength doesn't compensate for tungsten's limitations. Within a comparable range of high density (>10,000 kg/m³), the SEA values are not evidently influenced by topology, since W + Cu IPCs with cubic, rhombic dodecahedron and Gyroid structures yield comparable SEA values, as shown by the red solid upper triangles and red hollow right-pointing triangles on the right side of the plot in 12. Nonetheless, the SEA of

Gyroid W + Cu IPCs is significantly influenced by unit cell size [187], with the smallest cell size ($L = 2$ mm) achieving the highest SEA (14.64 kJ/kg) and the largest cell size ($L = 4$ mm) yielding the lowest value (4.61 kJ/kg). This is attributed to the better W-Cu bonding induced from higher surface area and positive geometric deviations in samples with smaller cell size. The excellent bonding leads to high yield and compressive strength, and thus results in higher EA and SEA under the same end-of-test strain. Regarding the W + Cu IPCs with cubic and rhombic dodecahedron structures [188], cubic one exhibits higher SEA (10.47 kJ/kg) than that of RD one (7.66 kJ/kg). This result is due to the distinct deformation modes of the two structures. The cubic W-skeleton primarily experiences buckling deformation, whereas the RD W-skeleton undergoes bending deformation. Moreover, buckling deformation typically resists higher loads before failure due to more uniform

load transfer, thereby resulting in greater EA and SEA [216].

The 304 steel + Zr-based metal glass IPC fabricated at 1233 K during the high pressure die casting exhibits the lowest SEA among all MM IPCs of 2.46 kJ/kg. It is worth noticing that monolithic 304 stainless steel and Vit 1 metal glass used in this work are high-ductility, high-energy-absorption materials, leaving the observed results unexpected [217,218]. This discrepancy is mainly attributed to the poor metallurgical bonding between the MG and 304 steel phase, leading to interfacial gaps and premature failure [51]. Additionally, the limited deformation of the MG phase, which is primarily localised within shear bands propagation, alongside the porosity and inhomogeneities included in the 3D stainless steel framework collectively contribute to a significant reduction in the energy absorption capacity. The aluminium foam ingots reinforced with Al alloy samples [129] retain their low-density characteristics while exhibiting moderate specific energy absorption performance. This combination makes them suitable for applications requiring lightweight structures with adequate energy absorption capabilities, such as automotive components, aerospace structures, and protective packaging materials [219–221].

For CM IPCs, their SEA values vary over a wide spectrum. Nanoarchitected nickel/carbon IPCs delivers the highest SEA value of approximately 161.18 kJ/kg (854.26 MJ/m³) with a density of 5300 kg/m³. The exceptional energy absorption ability results from the trade-off of reduced stiffness caused by poor interface bonding. At the fracture sites in the carbon phase, nickel provides closure force through tensile-like behaviours, impede local crack propagation while delaminates and shears against carbon matrix. The brittleness of pyrolysis carbon is successfully suppressed by nickel, and catastrophic failure is thus prevented, enabling greater deformation. The energy absorption capacity of CM IPCs is sensitive to the volume fraction of the ceramic phase. Zhang et al's Gyroid Al₂O₃ ceramic + Al-Mg-Si alloy IPCs demonstrated the lowest SEA among all studied samples, measuring 0.94 kJ/kg (3.37 MJ/m³). The brittle ceramic domain compromises the whole composite's ability to undergo deformation before shattering and fracture. Conversely, CM IPCs with lower ceramic proportions yielded moderate SEA properties, comparable to some MM, PM and PC IPCs.

Polymer materials are widely utilised in engineering applications, particularly due to their distinct energy absorption ability. In IPC designs, epoxy resins offer high strength but their energy absorption is limited by

brittleness unless modified, PEEK provides a balance of strength and toughness, resulting in superior energy absorption [222], while PU excels in flexibility and energy absorption, particularly in foam form, making it ideal for cushioning and impact protection applications [223]. The IPCs of Ti-6Al-4V with PEEK and epoxy [33,191], as well as AlSi10Mg + epoxy and ZrO₂ + epoxy ([156,157]) exhibited considerable SEA values, with some of the samples outperforming those of Al foam + Al and W + Cu MM IPCs and high-ceramic-content CaSiO₃ + Ti64 and Al₂O₃ + Al-Mg-Si CM IPCs. Furthermore, the hollow and porous structure of PU foams coated with Cu/Ni layers were unable to effectively accommodate deformation, resulting in comparatively lower SEA values.

5.4. Fracture toughness and toughening mechanisms

While this review primarily focuses on mechanical metrics such as modulus, strength, and energy absorption, it is pertinent to briefly address fracture toughness—a critical property for structural applications of IPCs [224].

Fracture toughness characterises a material's resistance to crack propagation under stress. Crack propagation can occur in various modes, with the most common being Mode I (opening mode) and Mode II (sliding mode) [70,225]. To evaluate fracture toughness, standard methods such as single-edge notched bending (SENB) and edge-notched disc bend (ENDB) tests are employed, often under Mode I or mixed-mode I/II loading conditions [226].

Several studies have demonstrated that interpenetrating architectures enable enhanced damage tolerance through synergistic toughening mechanisms such as crack deflection, crack bridging, and process zone formation. Xiao et al. [227] investigated polymer-polymer (PP) IPCs based on triply periodic minimal surface (TPMS) structures and observed that toughening was closely related to the reinforcement topology and constituent ductility. In particular, IPCs based on the Diamond structure showed greater deflection and energy dissipation than those based on IWP, with the VB+/Agilus30 system outperforming VB+/PP due to higher matrix compliance and phase interaction. Similarly, Li et al. [228] reported up to a sixteenfold increase in fracture toughness for 3D printed PP IPCs with architected rod-based lattice structures (simple-cubic, BCC, FCC), relative to their monolithic or particle-reinforced counterparts. These improvements were attributed to both intrinsic and extrinsic mechanisms: plastic deformation in the hard phase enabled by the compliant

matrix, and microstructural control of crack propagation paths.

These findings confirm that IPCs do not simply inherit the fracture characteristics of their constituents but instead demonstrate emergent behaviours through their architecture. The consideration of fracture toughness is essential for the development of IPCs intended for applications where resistance to crack initiation and propagation is critical.

6. Limitations and future perspectives

Interpenetrating phase composites have demonstrated mechanical performance that well exceeds the limitations of single-phase architected materials. Their multi-phase nature introduces rich design space, where the interplay between geometry, material distribution, and interfacial behaviour can be finely tuned to achieve enhanced functionality. Nonetheless, with these additional degrees of freedom come new challenges, particularly in characterisation, modelling, optimisation, and scalable fabrication. In particular:

- The majority of the literature on IPCs investigates their compressive performance. However, the performance in other fundamental loading modes, namely, tension, shear or torsion, as well as their thermal conductivity remain to a great extent unquantified. Further analysis and thorough experimental campaigns are required for the acquisition of a more comprehensive experimental dataset.
- Moreover, while most studies emphasise on static compression, the understanding of the IPC behaviour under dynamic loading remains limited. Strain-rate sensitivity—particularly relevant for polymer-based IPCs—is underexplored, despite the well-known rate-dependent behaviour of polymer matrices, particularly prominent for IPCs engineered exclusively with polymeric phases [80]. For MM IPCs, Zhang et al. reported stable plateau stresses across strain rates and temperatures due to crack-arresting interpenetrating structures for 3D-printed Mg–NiTi IPCs [229]. On the contrary, aluminium–polyurethane foam MP IPCs exhibited considerable strain-rate sensitivities, their performance governed by the polymeric filler, which enhanced energy absorption [230]. However, comparative insights into the role of inner architecture and base material selection on the effective dynamic performance for the above-analysed IPC classes are, up to now, infeasible. Further investigations into the dynamic performance, the associated failure mechanisms, the pre-existing and induced microstructural damage, and interphase cracking are necessary. In parallel, non-destructive techniques like CT-scanning should be leveraged to correlate manufacturing defects with the recorded mechanical performance under varying loading rates.
- As of their complex geometric design, diverse material phases, and interface conditions, experimental testing had up to now precedence over computational modelling. Comprehensive numerical models allowing for the parametric prediction of their effective thermomechanical attributes are critical for their design and inverse optimisation. Their modelling requires a detailed description of their inner topological features and elastoplastic material attributes, with simplified homogenisation methods being insufficient in capturing the complexity of the aforementioned parameters. As such, robust modelling approaches will provide the predictive tools required for their thorough understanding and for the acceleration of their development cycle.
- In the Ashby plots analysed in Section 5.3, the populated regions for a given IPC class, e.g. MM IPCs, span partially populated spaces. Different combinations of density-strength, densification strain, and energy absorption remain to be explored, leveraging base material combinations, reinforcement phase architectures, and processing techniques beyond the ones up to now investigated [33,231,232]. The previous tasks are a requirement for the understanding of the trade-offs and constraints inherent in IPC engineering.
- The electrical field-assisted heterogeneous material printing (EF-HMP) method, introduced in Section 3.3 by Tang et al. [161], offers potential for the in-situ manufacturing of multiphase PM IPC materials with substantial design freedom. The novel method thus requires further exploration and refinement, particularly in enhancing surface finish, improving geometric accuracy, and reassuring mechanical performance consistency [233].
- The dimensions of most of the samples up to now manufactured remain at an experimental scale [21], with dimensional upscaling effects remaining largely unexplored. The broader applicability of IPC materials requires the development of in-situ and scalable manufacturing methods [234,235].
- Recent advancements have demonstrated the efficacy of machine learning (ML) in enhancing topology optimisation processes, including symbolic regression and explainable ML frameworks [236,237]. Moreover, the Self-directed Online Learning Optimization (SOLO) framework integrates deep neural networks (DNNs) with finite element method

(FEM) calculations to expedite topology optimisation, significantly reducing computational costs associated with traditional methods [238]. Moreover, Gaussian Process Regression (GPR) has been employed as a surrogate modelling technique to predict material properties with associated uncertainty quantification [239]. In the context of interpenetrating phase composites, integrating these ML approaches can facilitate the design of materials with tailored properties [240]. Neural networks can predict optimal microstructures for desired mechanical and acoustic performance, while GPR can assist in understanding the trade-offs and uncertainties involved in material behaviour predictions.

While this review has primarily emphasised the mechanical behaviours of architected IPCs, it is essential to revisit a key point introduced in the beginning: architected structures alone – without classical interpenetrating phases – have demonstrated exceptional multifunctional potential. Recently, more research works show that through geometric design and interface engineering, these structures can deliver not only high stiffness and energy absorption, but also broadband acoustic performance and functional responsiveness. For example, Li et al. [241] developed an interwoven dual-phase lattice optimised via machine learning that achieves simultaneous improvements in stiffness, acoustic absorption, and elastic isotropy. More recently, a cuttlebone-inspired metamaterial that achieves exceptional mechanical energy absorption (50.7 J/g) alongside ultrahigh acoustic absorptance ($\bar{\alpha} = 0.80$) at a remarkable compact thickness was introduced [242]. Taken together, these two designs effectively overcome the long-standing trade-offs between mechanical robustness and acoustic performance, and merge two traditionally separate categories of mechanical and acoustic metamaterials into a unified multifunctional design space. Furthermore, Farman et al. [243] expand this direction by presenting an all-PDMS multi-layered sensor platform with engineered interfaces that can maintain high sensitivity and durability for pressure sensing applications on complex surfaces, illustrating the potential of architected designs in flexible and wearable IPC analogues.

These developments collectively highlight the growing potential of architected metamaterials in delivering multifunctional performance without relying on classical IPC phase architectures. Moreover, it is worth noting that the overall behaviours of these advanced systems are likely to be further enhanced when integrated into true IPC frameworks, where distinct material

phases can contribute synergistically to load transfer, damping, energy absorption, or functional responsiveness. This convergence of architectural ingenuity and material interpenetration offers an exciting future direction for the next generation of IPCs.

7. Summary

Overall, the current work has comprehensively investigated the manufacturing and mechanical performance of metal-metal, ceramic-metal, polymer-metal, and polymer-ceramic architected interpenetrating phase composites. The manufacturing processes typically employed were elaborated and critically compared, highlighting their merits and limitations. Subsequently, the physical and mechanical properties, including the elastic modulus, yield strength, densification, and failure strain as well as the overall energy absorption of different IPC designs were assessed, and comparatively presented in tabular and Ashby diagrams forms. It has been found that:

MM IPCs allow for versatile stiffness and strength attributes that can be tuned over wide performance spaces upon the appropriate selection of inner metallic phases. Their strength, densification and failure strain, as well as their specific energy absorption are particularly sensitive to the underlying reinforcement phase architecture.

The properties of CM IPCs are typically determined by the ceramic phase content. Most of the samples exhibit comparable stiffness and strength upon a rather close range of densities. In comparison, their critical densification strain and specific energy absorption vary distinctly among different structures and manufacturing methods.

Different PM and PC IPC designs have been shown capable of providing substantial stiffness and strength at moderate and low-density ranges, making them ideal lightweight candidates compared to MM and CM IPCs. Nevertheless, a wide range of phase combinations remains unexplored [68], requiring further investigations for the proper exploration of the feasible performance space.

While overlapping characteristics among different IPC designs can be identified, their overall mechanical performance is distinct and arises as a nonlinear combination of multiple interrelated factors. The comprehensive analysis provided aspires to act a reference summary of the state-of-the-art, providing unique insights into the inner design and performances up to now probed, while paving the way to a new generation of IPCs, that carefully consider and balance trade-offs between different design parameters, leveraging complementary attributes.

Disclosure statement

No potential conflict of interest was reported by the author(s).

Author contributions: CRediT

Qinze Song: Writing – original draught, Formal Analysis, Investigation, Visualization, Data Curation **Agyapal Singh:** Writing – review & editing, Writing – original draught, Visualization, Investigation **Nikolaos Karathanasopoulos:** Writing – review & editing, Visualization, Validation, Supervision, Resources, Project administration, Funding acquisition, Conceptualization.

Data availability statement

The datasets supporting the findings of this study are openly available in the Zenodo repository at <https://doi.org/10.5281/zenodo.15262461>.

References

- [1] Schnabelrauch M. Introduction to chapter 15: chemical bulk properties of biomaterials. In: Schnabelrauch M, editor. Chemical bulk properties of biomaterials. Berlin: Springer; 2017. p. 225–240.
- [2] Wei C, Zhang Z, Cheng D, et al. An overview of laser-based multiple metallic material additive manufacturing: from macro- to micro-scales. *Int J Extreme Manuf.* 2020;3(1):012003. doi: [10.1088/2631-7990/abce04](https://doi.org/10.1088/2631-7990/abce04)
- [3] Liu Y, Zhang X. Metamaterials: a new frontier of science and technology. *Chem Soc Rev.* 2011;40(5):2494–2507. doi: [10.1039/c0cs00184h](https://doi.org/10.1039/c0cs00184h)
- [4] Valipour A, Kargozarfard MH, Rakhshi M, et al. Metamaterials and their applications: an overview. *Proc Inst Mech Eng Part L.* 2022;236(11):2171–2210.
- [5] Lu C, Hsieh M, Huang Z, et al. Architectural design and additive manufacturing of mechanical metamaterials: a review. *Engineering.* 2022;17:44–63. doi: [10.1016/j.eng.2021.12.023](https://doi.org/10.1016/j.eng.2021.12.023)
- [6] Kadic M, Milton GW, van Hecke M, et al. 3D metamaterials. *Nat Rev Phys.* 2019;1(3):198–210. doi: [10.1038/s42254-018-0018-y](https://doi.org/10.1038/s42254-018-0018-y)
- [7] Fan J, Zhang L, Wei S, et al. A review of additive manufacturing of metamaterials and developing trends. *Mater Today.* 2021;50:303–328. doi: [10.1016/j.mattod.2021.04.019](https://doi.org/10.1016/j.mattod.2021.04.019)
- [8] Veselago VG. The electrodynamics of substances with simultaneously negative values of ϵ and μ . *Sov Phys Usp.* 1968;10(4):509–514. doi: [10.1070/PU1968v10n04ABEH003699](https://doi.org/10.1070/PU1968v10n04ABEH003699)
- [9] Cuan-Urquiza E, Silva RG. Fused filament fabrication of cellular, lattice and porous mechanical metamaterials: a review. *Virtual Phys Prototyping.* 2023;18(1):e2224300. doi: [10.1080/17452759.2023.2224300](https://doi.org/10.1080/17452759.2023.2224300)
- [10] Lakes R. Foam structures with a negative Poisson's ratio. *Science.* 1987;235(4792):1038–1040. doi: [10.1126/science.235.4792.1038](https://doi.org/10.1126/science.235.4792.1038)
- [11] Bertoldi K, Reis PM, Willshaw S, et al. Negative Poisson's ratio behavior induced by an elastic instability. *Adv Mater.* 2010;22(3):361–366.
- [12] Zheng X, Lee H, Weisgraber TH, et al. Ultralight, ultrastiff mechanical metamaterials. *Science.* 2014;344(6190):1373–1377. doi: [10.1126/science.1252291](https://doi.org/10.1126/science.1252291)
- [13] Li X, Gao H. Smaller and stronger. *Nat Mater.* 2016;15(4):373–374. doi: [10.1038/nmat4591](https://doi.org/10.1038/nmat4591)
- [14] Bückmann T, Thiel M, Kadic M, et al. An elasto-mechanical unfeelability cloak made of pentamode metamaterials. *Nat Commun.* 2014;5(1):4130. doi: [10.1038/ncomms5130](https://doi.org/10.1038/ncomms5130)
- [15] Liu C, Zhang X, Chang J, et al. Programmable mechanical metamaterials: basic concepts, types, construction strategies—a review. *Front Mater.* 2024;11:1361408. doi: [10.3389/fmats.2024.1361408](https://doi.org/10.3389/fmats.2024.1361408)
- [16] Haibo Feng LX, Xu C, Li L. Multiscale hierarchical composite with extremely specific damping performance via bottom-up synergistic enhancement strategy. *Virtual Phys Prototyping.* 2025;20(1):e2448541. doi: [10.1080/17452759.2024.2448541](https://doi.org/10.1080/17452759.2024.2448541)
- [17] Askari A, Jamalzadeh M. A review of structural diversity design and optimization for lattice metamaterials. *AIP Adv.* 2024;14(10):100702. doi: [10.1063/5.0229080](https://doi.org/10.1063/5.0229080)
- [18] Armstrong M, Mehrabi H, Naveed N. An overview of modern metal additive manufacturing technology. *J Manuf Process.* 2022;84:1001–1029. doi: [10.1016/j.jmapro.2022.10.060](https://doi.org/10.1016/j.jmapro.2022.10.060)
- [19] Mercado Rivera FJ, Rojas Arciniegas AJ. Additive manufacturing methods: techniques, materials, and closed-loop control applications. *Int J Adv Manuf Technol.* 2020;109:17–31. doi: [10.1007/s00170-020-05663-6](https://doi.org/10.1007/s00170-020-05663-6)
- [20] Sireesha M, Lee J, Kiran ASK, et al. A review on additive manufacturing and its way into the oil and gas industry. *RSC Adv.* 2018;8(40):22460–22468. doi: [10.1039/C8RA03194K](https://doi.org/10.1039/C8RA03194K)
- [21] Umanzor ME, Batra RC, Williams CB, et al. Penetration resistance of cast metal-ceramic composite lattice structures. *Adv Eng Mater.* 2021;23(12):2100577. doi: [10.1002/adem.v23.12](https://doi.org/10.1002/adem.v23.12)
- [22] Shomper M. Tangible solutions | designing lattice structures for medical implants. [accessed 2025 Jan 17]. Available from: <https://www.ntop.com/resources/blog/1194designing-lattice-structures-for-medical-implants/> (July 25 2019)
- [23] nTop. Guide to lattice structures in additive manufacturing. [accessed 2025 Jan 17]. Available from: <https://www.ntop.com/resources/blog/1197guide-to-lattice-structures-in-additive-manufacturing/> (April 28 2022)
- [24] Nazir A, Gokcekaya O, Billah KMM, et al. Multi-material additive manufacturing: a systematic review of design, properties, applications, challenges, and 3D printing of materials and cellular metamaterials. *Mater Des.* 2023;226:111661. doi: [10.1016/j.matdes.2023.111661](https://doi.org/10.1016/j.matdes.2023.111661)
- [25] Deshpande VS, Fleck NA, Ashby MF. Effective properties of the octet-truss lattice material. *J Mech Phys Solids.* 2001;49(8):1747–1769. doi: [10.1016/S0022-5096\(01\)00010-2](https://doi.org/10.1016/S0022-5096(01)00010-2)
- [26] Syam WP, Jianwei W, Zhao B, et al. Design and analysis of strut-based lattice structures for vibration isolation. *Precis Eng.* 2018;52:494–506. doi: [10.1016/j.precisioneng.2017.09.010](https://doi.org/10.1016/j.precisioneng.2017.09.010)

- [27] Viswanath A, Khan KA, Barsoum M. Design of novel isosurface strut-based lattice structures: effective stiffness, strength, anisotropy and fatigue properties. *Mater Des.* **2022**;224:111293. doi: [10.1016/j.matdes.2022.111293](https://doi.org/10.1016/j.matdes.2022.111293)
- [28] Viet N, Karathanasopoulos N, Zaki W. Mechanical attributes and wave propagation characteristics of TPMS lattice structures. *Mech Mater.* **2022**;172:104363. doi: [10.1016/j.mechmat.2022.104363](https://doi.org/10.1016/j.mechmat.2022.104363)
- [29] Senhora FV, Sanders ED, Paulino GH. Optimally-tailored spinodal architected materials for multiscale design and manufacturing. *Adv Mater.* **2022**;34(26):2109304. doi: [10.1002/adma.v34.26](https://doi.org/10.1002/adma.v34.26)
- [30] Soyarslan C, Bargmann S, Pradas M, et al. 3D stochastic bicontinuous microstructures: generation, topology and elasticity. *Acta Mater.* **2018**;149:326–340. doi: [10.1016/j.actamat.2018.01.005](https://doi.org/10.1016/j.actamat.2018.01.005)
- [31] Ioannidis M, Chatzis I. On the geometry and topology of 3D stochastic porous media. *J Colloid Interface Sci.* **2000**;229(2):323–334. doi: [10.1006/jcis.2000.7055](https://doi.org/10.1006/jcis.2000.7055)
- [32] Wang X, Li X, Li Z, et al. Superior strength, toughness, and damage-tolerance observed in microlattices of aperiodic unit cells. *Small.* **2024**;20(23):2307369. doi: [10.1002/smll.v20.23](https://doi.org/10.1002/smll.v20.23)
- [33] Wang X, Li Z, Deng J, et al. Unprecedented strength enhancement observed in interpenetrating phase composites of aperiodic lattice metamaterials. *Adv Funct Mater.* **2024**; 34(25):2406890. doi: [10.1002/adfm.2406890](https://doi.org/10.1002/adfm.2406890)
- [34] Zhang Y, Hsieh M-T, Valdevit L. Mechanical performance of 3D printed interpenetrating phase composites with spinodal topologies. *Compos Struct.* **2021**;263:113693. doi: [10.1016/j.compstruct.2021.113693](https://doi.org/10.1016/j.compstruct.2021.113693)
- [35] Feng J, Fu J, Yao X, et al. Triply periodic minimal surface (TPMS) porous structures: from multi-scale design, precise additive manufacturing to multidisciplinary applications. *Int J Extreme Manuf.* **2022**;4(2):022001. doi: [10.1088/2631-7990/ac5be6](https://doi.org/10.1088/2631-7990/ac5be6)
- [36] Kladovasilakis N, Tsongas K, Kostavelis I, et al. Effective mechanical properties of additive manufactured triply periodic minimal surfaces: experimental and finite element study. *Int J Adv Manuf Technol.* **2022**;121(11):7169–7189. doi: [10.1007/s00170-022-09651-w](https://doi.org/10.1007/s00170-022-09651-w)
- [37] Ermolenko S, Snopov P. Porosity and topological properties of triply periodic minimal surfaces. arXiv preprint arXiv:2406.16215.
- [38] Jung Y, Torquato S. Fluid permeabilities of triply periodic minimal surfaces. *Phys Rev E Stat Nonlinear Soft Matter Phys.* **2005**;72(5):056319. doi: [10.1103/PhysRevE.72.056319](https://doi.org/10.1103/PhysRevE.72.056319)
- [39] Dadashi A, Rahimi G. A comprehensive investigation of the lattice structure mechanical properties based on Schwarz primitive triply periodic minimal surface: elastic modulus, yield strength, and maximum bearing force in the elastic region. *Int J Solids Struct.* **2024**;295:112776. doi: [10.1016/j.ijsolstr.2024.112776](https://doi.org/10.1016/j.ijsolstr.2024.112776)
- [40] Xie H, Wang Y, Liu F, et al. Strengthening mechanism of TPMS interpenetrating phase composites for bone tissue engineering. *Compos Struct.* **2024**;349:118526. doi: [10.1016/j.compstruct.2024.118526](https://doi.org/10.1016/j.compstruct.2024.118526)
- [41] Han L, Che S. An overview of materials with triply periodic minimal surfaces and related geometry: from biological structures to self-assembled systems. *Adv Mater.* **2018**;30(17):1705708. doi: [10.1002/adma.v30.17](https://doi.org/10.1002/adma.v30.17)
- [42] Michielsen K, Kole J. Photonic band gaps in materials with triply periodic surfaces and related tubular structures. *Phys Rev B.* **2003**;68(11):115107. doi: [10.1103/PhysRevB.68.115107](https://doi.org/10.1103/PhysRevB.68.115107)
- [43] Grosse-Brauckmann K. Triply periodic minimal and constant mean curvature surfaces. *Interface Focus.* **2012**;2(5):582–588. doi: [10.1098/rsfs.2011.0096](https://doi.org/10.1098/rsfs.2011.0096)
- [44] Sabet FA, Su FY, McKittrick J, et al. Mechanical properties of model two-phase composites with continuous compared to discontinuous phases. *Adv Eng Mater.* **2018**;20(10):1800505. doi: [10.1002/adem.v20.10](https://doi.org/10.1002/adem.v20.10)
- [45] Liu W, Köster U. Microstructures and properties of interpenetrating alumina/aluminium composites made by reaction of SiO₂ glass preforms with molten aluminium. *Mater Sci Eng A.* **1996**;210(1–2):1–7. doi: [10.1016/0921-5093\(95\)10078-4](https://doi.org/10.1016/0921-5093(95)10078-4)
- [46] Wegner L, Gibson L. The mechanical behaviour of interpenetrating phase composites—I: modelling. *Int J Mech Sci.* **2000**;42(5):925–942. doi: [10.1016/S0020-7403\(99\)00025-9](https://doi.org/10.1016/S0020-7403(99)00025-9)
- [47] Feng P, Zhao R, Yang F, et al. Co-continuous structure enhanced magnetic responsive shape memory PLLA/TPU blend fabricated by 4D printing. *Virtual Phys Prototyping.* **2024**;19(1):e2290186. doi: [10.1080/17452759.2023.2290186](https://doi.org/10.1080/17452759.2023.2290186)
- [48] Wang L, Lau J, Thomas EL, et al. Co-continuous composite materials for stiffness, strength, and energy dissipation. *Adv Mater.* **2011**;23(13):1524. doi: [10.1002/adma.v23.13](https://doi.org/10.1002/adma.v23.13)
- [49] Su FY, Sabet FA, Tang K, et al. Scale and size effects on the mechanical properties of bioinspired 3D printed two-phase composites. *J Mater Res Technol.* **2020**;9(6):14944–14960. doi: [10.1016/j.jmrt.2020.10.052](https://doi.org/10.1016/j.jmrt.2020.10.052)
- [50] Su J, Guo L, Zhu H, et al. High toughness of 3D printed ceramic/polymer interpenetrating phase composite with gradient structures under multi-directional stresses. *J Mater Sci.* **2025**;60:4197–4210.
- [51] Gao W, Zhang W, Zhang T, et al. Large tensile plasticity in Zr-based metallic glass/stainless steel interpenetrating-phase composites prepared by high pressure die casting. *Composites Part B.* **2021**;224:109226. doi: [10.1016/j.compositesb.2021.109226](https://doi.org/10.1016/j.compositesb.2021.109226)
- [52] Nejad SR, Hosseinpour M, Mirbagheri SMH. Interface characterization of Mg-7Al-1Ca alloy reinforced by integrated 3DCu open-cell foam. *Mater Charact.* **2024**;209:113687. doi: [10.1016/j.matchar.2024.113687](https://doi.org/10.1016/j.matchar.2024.113687)
- [53] Asar A, Zaki W. A comprehensive review of the mechanisms and structure of interpenetrating phase composites with emphasis on metal-metal and polymer-metal variants. *Compos Part B Eng.* **2024**;275:111314. doi: [10.1016/j.compositesb.2024.111314](https://doi.org/10.1016/j.compositesb.2024.111314)
- [54] Huang G, Li B. Fabrication of bimetallic interpenetrating structures with enhanced impact resistance via 3D-printing of high-entropy alloy lattices and vacuum melt infiltration of al-based alloys. *Virtual Phys Prototyping.* **2025**;20(1):e2459799. doi: [10.1080/17452759.2025.2459799](https://doi.org/10.1080/17452759.2025.2459799)
- [55] Yu-Bai Hu M-YJ, Shen P. Compositionally gradient Al₂O₃–B₄C/Al composites with interpenetrating structure and tailored properties via material extrusion-based additive manufacturing and pressure infiltration. *Virtual Phys Prototyping.* **2025**;20(1):e2450101. doi: [10.1080/17452759.2025.2450101](https://doi.org/10.1080/17452759.2025.2450101)

- [56] Chen L-Y, Qin P, Zhang L, et al. An overview of additively manufactured metal matrix composites: preparation, performance, and challenge. *Int J Extreme Manuf.* **2024**;6(5):052006. doi: [10.1088/2631-7990/ad54a4](https://doi.org/10.1088/2631-7990/ad54a4)
- [57] Dou C, Zhang M, Ren D, et al. Bi-continuous Mg-Ti interpenetrating-phase composite as a partially degradable and bioactive implant material. *J Mater Sci Technol.* **2023**;146:211–220. doi: [10.1016/j.jmst.2022.11.011](https://doi.org/10.1016/j.jmst.2022.11.011)
- [58] Liu Z, Zhang Z, Ritchie RO. Structural orientation and anisotropy in biological materials: functional designs and mechanics. *Adv Funct Mater.* **2020**;30(10):1908121. doi: [10.1002/adfm.v30.10](https://doi.org/10.1002/adfm.v30.10)
- [59] Kota N, Charan MS, Laha T, et al. Review on development of metal/ceramic interpenetrating phase composites and critical analysis of their properties. *Ceram Int.* **2022**;48(2):1451–1483. doi: [10.1016/j.ceramint.2021.09.232](https://doi.org/10.1016/j.ceramint.2021.09.232)
- [60] del Rio E, Nash JM, Williams JC, et al. Co-continuous composites for high-temperature applications. *Mater Sci Eng A.* **2007**;463(1–2):115–121. doi: [10.1016/j.msea.2006.07.162](https://doi.org/10.1016/j.msea.2006.07.162)
- [61] Abu Al-Rub RK, Abueidda DW, Dalaq AS. Thermo-electro-mechanical properties of interpenetrating phase composites with periodic architecture reinforcements. In: Altenbach H, Matsuda T, Okumura D, editors. *From creep damage mechanics to homogenization methods: A Liber Amicorum to celebrate the birthday of Nobutada Ohno*. Cham: Springer; **2015**. p. 1–18.
- [62] Chen Y, Wang A, Fu H, et al. Preparation, microstructure and deformation behavior of Zr-based metallic glass/porous SiC interpenetrating phase composites. *Mater Sci Eng A.* **2011**;530:15–20. doi: [10.1016/j.msea.2011.08.063](https://doi.org/10.1016/j.msea.2011.08.063)
- [63] Han X, Zhang Y, Li J, et al. Mechanical properties of Cu-W interpenetrating-phase composites with ordered skeletons. *Metals.* **2022**;12(6):903. doi: [10.3390/met12060903](https://doi.org/10.3390/met12060903)
- [64] Qing P, Huang S, Naren T, et al. Interpenetrating LiB/ Li_3BN_2 phases enabling stable composite lithium metal anode. *Sci Bull.* **2024**;69(18):2842–2852. doi: [10.1016/j.scib.2024.07.021](https://doi.org/10.1016/j.scib.2024.07.021)
- [65] Biswas A, Xu R, Christiansen-Salameh J, et al. Phase stability of hexagonal/cubic boron nitride nanocomposites. *Nano Lett.* **2023**;23(15):6927–6936. doi: [10.1021/acs.nanolett.3c01537](https://doi.org/10.1021/acs.nanolett.3c01537)
- [66] Roy S, Gibmeier J, Wanner A. In situ study of internal load transfer in a novel metal/ceramic composite exhibiting lamellar microstructure using energy dispersive synchrotron x-ray diffraction. *Adv Eng Mater.* **2009**;11(6):471–477. doi: [10.1002/adem.v11.6](https://doi.org/10.1002/adem.v11.6)
- [67] Roy S, Gibmeier J, Schell KG, et al. Internal load transfer in an interpenetrating metal/ceramic composite material studied using energy dispersive synchrotron x-ray diffraction. *Mater Sci Eng A.* **2019**;753:247–252. doi: [10.1016/j.msea.2019.03.049](https://doi.org/10.1016/j.msea.2019.03.049)
- [68] Jalilzadeh E, Rohani Nejad S, Khiabani A, et al. Mechanical response of open-cell metal foams with single-and multilayer shell during uniaxial compression test. *Adv Eng Mater.* **2024**;26(6):2301995. doi: [10.1002/adem.v26.6](https://doi.org/10.1002/adem.v26.6)
- [69] Wang X, Zhou Y, Li J, et al. Uniaxial compression mechanical properties of foam nickel/iron-epoxy interpenetrating phase composites. *Materials.* **2021**;14(13):3523. doi: [10.3390/ma14133523](https://doi.org/10.3390/ma14133523)
- [70] Khedri E, reza Karimi H, Aliha M, et al. Tensile, flexural, and mode-I cracking behavior of interpenetrating phase composites (IPC), developed using additively manufactured PLA-based structures with different infill densities and epoxy resin polymer as matrix. *Results Eng.* **2024**;22:102162. doi: [10.1016/j.rineng.2024.102162](https://doi.org/10.1016/j.rineng.2024.102162)
- [71] Silverstein MS. Interpenetrating polymer networks: so happy together? *Polymer.* **2020**;207:122929. doi: [10.1016/j.polymer.2020.122929](https://doi.org/10.1016/j.polymer.2020.122929)
- [72] Sperling LH. *Interpenetrating polymer networks and related materials*. New York: Springer Science & Business Media; **2012**.
- [73] Xu K, Jing F, Zhao R, et al. Bio-based epoxy/polyurethane interpenetrating polymer networks (IPNs) derived from plant oils with tunable thermal and mechanical properties. *J Therm Anal Calorim.* **2023**;148(19):10093–10102. doi: [10.1007/s10973-023-12368-x](https://doi.org/10.1007/s10973-023-12368-x)
- [74] Chern Y, Hsieh K-H, Ma C, et al. Interpenetrating polymer networks of polyurethane and epoxy. *J Mater Sci.* **1994**;29:5435–5440. doi: [10.1007/BF01171558](https://doi.org/10.1007/BF01171558)
- [75] Pandey P, Kamal M, Srivastava A. Interpenetrating polymer network of poly (styrene) and poly (citronelol-*alt*-methyl methacrylate). Synthesis and characterization. *Polym J.* **2003**;35(2):122–126. doi: [10.1295/polymj.35.122](https://doi.org/10.1295/polymj.35.122)
- [76] Kizhnyaev VN, Pokatilov FA, Shabalov AI, et al. Conetworks on the base of polystyrene with poly (methyl methacrylate) paired polymers. *e-Polymers.* **2019**;19(1):421–429. doi: [10.1515/epoly-2019-0043](https://doi.org/10.1515/epoly-2019-0043)
- [77] Adachi H, Kotaka T. Structure and mechanical properties of sequential interpenetrating polymer networks. I. Poly (ethyl acrylate)/poly (methyl methacrylate) system. *Polym J.* **1982**;14(5):379–390. doi: [10.1295/polymj.14.379](https://doi.org/10.1295/polymj.14.379)
- [78] Mathew AP. Interpenetrating polymer networks: processing, properties and applications. In: Thomas S, editor. *Advances in elastomers I: blends and interpenetrating networks*. Berlin: Springer; **2013**. p. 283–301.
- [79] Singh A, Karathanasopoulos N. Strut and stochastic polymer reinforcement interpenetrating phase composites: static, strain-rate and dynamic damping performance. *Thin-Walled Struct.* **2024**;198:111618. doi: [10.1016/j.tws.2024.111618](https://doi.org/10.1016/j.tws.2024.111618)
- [80] Singh A, Al-Ketan O, Karathanasopoulos N. Highly strain-rate sensitive and ductile composite materials combining soft with stiff TPMS polymer-based interpenetrating phases. *Compos Struct.* **2024**;328:117646. doi: [10.1016/j.comstruct.2023.117646](https://doi.org/10.1016/j.comstruct.2023.117646)
- [81] Al-Ketan O, Assad MA, Al-Rub RKA. Mechanical properties of periodic interpenetrating phase composites with novel architected microstructures. *Compos Struct.* **2017**;176:9–19. doi: [10.1016/j.comstruct.2017.05.026](https://doi.org/10.1016/j.comstruct.2017.05.026)
- [82] Singh A, Al-Ketan O, Karathanasopoulos N. Mechanical performance of solid and sheet network-based stochastic interpenetrating phase composite materials. *Composites Part B.* **2023**;251:110478. doi: [10.1016/j.compositesb.2022.110478](https://doi.org/10.1016/j.compositesb.2022.110478)
- [83] Qadri MF, Malviya R, Sharma PK. Biomedical applications of interpenetrating polymer network system. *Open Pharm Sci J.* **2015**;2(1):21–30. doi: [10.2174/1874844901502010021](https://doi.org/10.2174/1874844901502010021)

- [84] Klempner D, Sophiea D. Interpenetrating polymer networks. In: Cheremisinoff NP, editor. Elastomer technology handbook. Boca Raton: CRC Press; 2020. p. 421–444.
- [85] Prashanth KG, composites I. A nomenclature dilemma. *Materials*. 2025;18(2):273. doi: [10.3390/ma18020273](https://doi.org/10.3390/ma18020273)
- [86] Gardner L. Metal additive manufacturing in structural engineering—review, advances, opportunities and outlook. *Structures*. 2023;47:2178–2193. doi: [10.1016/j.istruc.2022.12.039](https://doi.org/10.1016/j.istruc.2022.12.039)
- [87] Wu Y, Fang J, Wu C, et al. Additively manufactured materials and structures: a state-of-the-art review on their mechanical characteristics and energy absorption. *Int J Mech Sci*. 2023;246:108102. doi: [10.1016/j.ijmecsci.2023.108102](https://doi.org/10.1016/j.ijmecsci.2023.108102)
- [88] Tariq A, Arif ZU, Khalid MY, et al. Recent advances in the additive manufacturing of stimuli-responsive soft polymers. *Adv Eng Mater*. 2023;25(21):2301074. doi: [10.1002/adem.v25.21](https://doi.org/10.1002/adem.v25.21)
- [89] Zhou X, Ren L, Song Z, et al. Advances in 3D/4D printing of mechanical metamaterials: from manufacturing to applications. *Composites Part B*. 2023;254:110585. doi: [10.1016/j.compositesb.2023.110585](https://doi.org/10.1016/j.compositesb.2023.110585)
- [90] Behera MP, Dougherty T, Singamneni S. Conventional and additive manufacturing with metal matrix composites: a perspective. *Procedia Manuf*. 2019;30:159–166. doi: [10.1016/j.promfg.2019.02.023](https://doi.org/10.1016/j.promfg.2019.02.023)
- [91] Zhai Y, Lados DA, LaGoy JL. Additive manufacturing: making imagination the major limitation. *JOM*. 2014;66:808–816. doi: [10.1007/s11837-014-0886-2](https://doi.org/10.1007/s11837-014-0886-2)
- [92] Kaikai X, Yadong G, Qiang Z. Comparison of traditional processing and additive manufacturing technologies in various performance aspects: a review. *Arch Civ Mech Eng*. 2023;23(3):188. doi: [10.1007/s43452-023-00699-3](https://doi.org/10.1007/s43452-023-00699-3)
- [93] Askari M, Hutchins DA, Thomas PJ, et al. Additive manufacturing of metamaterials: a review. *Addit Manuf*. 2020;36:101562.
- [94] International Organization for Standardization. Additive manufacturing – general principles – fundamentals and vocabulary. Standard; 2021.
- [95] International Organization for Standardization. ISO 17296-2:2015. Additive manufacturing– General principles– Part 2: Overview of process categories and feedstock. Geneva: ISO; 2015.
- [96] Wang X, Jiang M, Zhou Z, et al. 3D printing of polymer matrix composites: a review and prospective. *Composites Part B*. 2017;110:442–458. doi: [10.1016/j.compositesb.2016.11.034](https://doi.org/10.1016/j.compositesb.2016.11.034)
- [97] Yap CY, Chua CK, Dong ZL, Liu ZH, Zhang DQ, Loh LE, Sing SL. Review of selective laser melting: materials and applications. *Appl Phys Rev*. 2015;2(4):041101. doi: [10.1063/1.4935926](https://doi.org/10.1063/1.4935926)
- [98] Suryawanshi J, Prashanth K, Ramamurty U. Mechanical behavior of selective laser melted 316L stainless steel. *Mater Sci Eng A*. 2017;696:113–121. doi: [10.1016/j.msea.2017.04.058](https://doi.org/10.1016/j.msea.2017.04.058)
- [99] Zhao X, Li S, Zhang M, et al. Comparison of the microstructures and mechanical properties of Ti-6Al-4V fabricated by selective laser melting and electron beam melting. *Mater Des*. 2016;95:21–31. doi: [10.1016/j.matdes.2015.12.135](https://doi.org/10.1016/j.matdes.2015.12.135)
- [100] Metalnikov P, Ben-Hamu G, Eliezer D. Corrosion behavior of AM-Ti-6Al-4V: a comparison between EBM and SLM. *Prog Addit Manuf*. 2022;7(3):509–520. doi: [10.1007/s40964-022-00293-8](https://doi.org/10.1007/s40964-022-00293-8)
- [101] Al Rashid A, Ahmed W, Khalid MY, et al. Vat photopolymerization of polymers and polymer composites: processes and applications. *Addit Manuf*. 2021;47:102279.
- [102] Montero J, Vitale P, Weber S, et al. Indirect additive manufacturing of resin components using polyvinyl alcohol sacrificial moulds. *Procedia CIRP*. 2020;91:388–395. doi: [10.1016/j.procir.2020.02.191](https://doi.org/10.1016/j.procir.2020.02.191)
- [103] Gao M, Pan Y, Oliveira F, et al. Interpenetrating microstructure and fracture mechanism of NiAl/Tic composites by pressureless melt infiltration. *Mater Lett*. 2004;58(11):1761–1765. doi: [10.1016/j.matlet.2003.10.060](https://doi.org/10.1016/j.matlet.2003.10.060)
- [104] Etter T, Kuebler J, Frey T, et al. Strength and fracture toughness of interpenetrating graphite/aluminium composites produced by the indirect squeeze casting process. *Mater Sci Eng A*. 2004;386(1–2):61–67. doi: [10.1016/S0921-5093\(04\)00915-3](https://doi.org/10.1016/S0921-5093(04)00915-3)
- [105] Mattern A, Huchler B, Staudenecker D, et al. Preparation of interpenetrating ceramic–metal composites. *J Eur Ceram Soc*. 2004;24(12):3399–3408. doi: [10.1016/j.jeurceramsoc.2003.10.030](https://doi.org/10.1016/j.jeurceramsoc.2003.10.030)
- [106] Maj J, Basista M, Węglewski W, et al. Effect of microstructure on mechanical properties and residual stresses in interpenetrating aluminum-alumina composites fabricated by squeeze casting. *Mater Sci Eng A*. 2018;715:154–162. doi: [10.1016/j.msea.2017.12.091](https://doi.org/10.1016/j.msea.2017.12.091)
- [107] Kota N, Jana P, Sahasrabudhe S, et al. Processing and characterization of Al-Si alloy/SiC foam interpenetrating phase composite. *Mater Today Proc*. 2021;44:2930–2933. doi: [10.1016/j.matpr.2021.01.923](https://doi.org/10.1016/j.matpr.2021.01.923)
- [108] Jiang Y, Xu P, Zhang C, et al. Simulation and experimental of infiltration and solidification process for Al_2O_3 (3D)/5083Al interpenetrating phase composite for high speed train prepared by low-pressure infiltration. *Materials*. 2023;16(20):6634. doi: [10.3390/ma16206634](https://doi.org/10.3390/ma16206634)
- [109] Vijayan K, Ramalingam S, Sadik MRA, et al. Fabrication of co-continuous ceramic composite (C4) through gas pressure infiltration technique. *Mater Today Proc*. 2021;46:1013–1016. doi: [10.1016/j.matpr.2021.01.212](https://doi.org/10.1016/j.matpr.2021.01.212)
- [110] VT S, Bright RJ. Experimental studies on the mechanical behaviour of LM25-SICF-interpenetrating phase composites synthesized using gas pressure infiltration. *Silicon*. 2023;15(17):7357–7370. doi: [10.1007/s12633-023-02584-3](https://doi.org/10.1007/s12633-023-02584-3)
- [111] Basista M, Jakubowska J, Węglewski W. Processing induced flaws in aluminum-alumina interpenetrating phase composites. *Adv Eng Mater*. 2017;19(12):1700484. doi: [10.1002/adem.v19.12](https://doi.org/10.1002/adem.v19.12)
- [112] Weflen E, Frank MC. Hybrid additive and subtractive manufacturing of multi-material objects. *Rapid Prototyp J*. 2021;27(10):1860–1871. doi: [10.1108/RPJ-06-2020-0142](https://doi.org/10.1108/RPJ-06-2020-0142)
- [113] Strong D, Kay M, Conner B, et al. Hybrid manufacturing—integrating traditional manufacturers with additive manufacturing (AM) supply chain. *Addit Manuf*. 2018;21:159–173.
- [114] Singh A, Al-Ketan O, Karathanasopoulos N. Hybrid manufacturing and mechanical properties of architected

- interpenetrating phase metal-ceramic and metal-metal composites. *Mater Sci Eng A.* **2024**;897:146322. doi: [10.1016/j.msea.2024.146322](https://doi.org/10.1016/j.msea.2024.146322)
- [115] Hong L, Guo X, Li G, et al. Multi-directional freeze-casting of interpenetrating phase composites with multi-aligned structure, nearly isotropy, high performance. *Mater Des.* **2024**;244:113172. doi: [10.1016/j.matdes.2024.113172](https://doi.org/10.1016/j.matdes.2024.113172)
- [116] Kozak J, Rajurkar KP. Hybrid machining process evaluation and development. In: Proceedings of 2nd International Conference on Machining and Measurements of Sculptured Surfaces, Keynote Paper, Krakow; 2000, p. 501–536.
- [117] Pragana J, Sampaio RF, Bragança I, et al. Hybrid metal additive manufacturing: a state-of-the-art review. *Adv Ind Manuf Eng.* **2021**;2:100032.
- [118] Wu L, Meng L, Wang Y, et al. Fabrication of polyether-etherketone (peek)-based 3D electronics with fine resolution by a hydrophobic treatment assisted hybrid additive manufacturing method. *Int J Extreme Manuf.* **2023**;5(3):035003. doi: [10.1088/2631-7990/acd826](https://doi.org/10.1088/2631-7990/acd826)
- [119] Vevers A, Kromanis A, Gerins E, et al. Additive manufacturing and casting technology comparison: mechanical properties, productivity and cost benchmark. *Latv J Phys Tech Sci.* **2018**;55(2):56–63.
- [120] Forrester K, Sheridan R, Phoenix RD. Assessing the accuracy of casting and additive manufacturing techniques for fabrication of a complete palatal coverage metal framework. *J Prosthodont.* **2019**;28(7):811–817. doi: [10.1111/jopr.v28.7](https://doi.org/10.1111/jopr.v28.7)
- [121] Dejene ND, Lemu HG, Gutema EM. Critical review of comparative study of selective laser melting and investment casting for thin-walled parts. *Materials.* **2023**;16(23):7346. doi: [10.3390/ma16237346](https://doi.org/10.3390/ma16237346)
- [122] Sealy MP, Madireddy G, Williams RE, et al. Hybrid processes in additive manufacturing. *J Manuf Sci Eng.* **2018**;140(6):060801. doi: [10.1115/1.4038644](https://doi.org/10.1115/1.4038644)
- [123] Lynch P, Hasbrouck C, Wilck J, et al. Challenges and opportunities to integrate the oldest and newest manufacturing processes: metal casting and additive manufacturing. *Rapid Prototyp J.* **2020**;26(6):1145–1154. doi: [10.1108/RPJ-10-2019-0277](https://doi.org/10.1108/RPJ-10-2019-0277)
- [124] Lauwers B, Klocke F, Klink A, et al. Hybrid processes in manufacturing. *CIRP Ann.* **2014**;63(2):561–583. doi: [10.1016/j.cirp.2014.05.003](https://doi.org/10.1016/j.cirp.2014.05.003)
- [125] Mitra S, de Castro AR, El Mansori M. On the rapid manufacturing process of functional 3D printed sand molds. *J Manuf Process.* **2019**;42:202–212. doi: [10.1016/j.jmapro.2019.04.034](https://doi.org/10.1016/j.jmapro.2019.04.034)
- [126] León-Cabezas M, Martínez-García A, Varela-Gandía F. Innovative advances in additive manufactured moulds for short plastic injection series. *Procedia Manuf.* **2017**;13:732–737. doi: [10.1016/j.promfg.2017.09.124](https://doi.org/10.1016/j.promfg.2017.09.124)
- [127] Lin Y, Wang D, Yang C, et al. An Al-Al interpenetrating-phase composite by 3D printing and hot extrusion. *Int J Miner Metall Mater.* **2023**;30(4):678–688. doi: [10.1007/s12613-022-2543-z](https://doi.org/10.1007/s12613-022-2543-z)
- [128] Viganò D, Balzarotti R, Santoliquido O, et al. A preliminary investigation of gyroids made of W-Cu composite materials produced by investment casting into SiO₂-based molds 3D-printed by stereolithography. *Mater Des.* **2023**;234:112361. doi: [10.1016/j.matdes.2023.112361](https://doi.org/10.1016/j.matdes.2023.112361)
- [129] Liu E, Bai Y, Li J, et al. Bi-continuous interpenetrated porous composite integrating the high strength and long plateau stress stage prepared by an in situ method. *Composites Part A: Applied Science and Manufacturing.* **2024**;185:108315. doi: [10.1016/j.compositesa.2024.108315](https://doi.org/10.1016/j.compositesa.2024.108315)
- [130] Li Z, Mo H, Tian J, et al. A novel Ti/Al interpenetrating phase composite with enhanced mechanical properties. *Mater Lett.* **2024**;357:135723. doi: [10.1016/j.matlet.2023.135723](https://doi.org/10.1016/j.matlet.2023.135723)
- [131] Zhang M, Yu Q, Liu Z, et al. 3D printed Mg-NiTi interpenetrating-phase composites with high strength, damping capacity, and energy absorption efficiency. *Sci Adv.* **2020**;6(19):eaba5581. doi: [10.1126/sciadv.aba5581](https://doi.org/10.1126/sciadv.aba5581)
- [132] Zhai J, Gao W, Dong H, et al. Novel metal matrix composites reinforced with Zr-based metallic glass lattices. *Appl Mater Today.* **2022**;29:101649. doi: [10.1016/j.apmt.2022.101649](https://doi.org/10.1016/j.apmt.2022.101649)
- [133] Ghasri-Khouzani M, Li X, Bogno A, et al. Fabrication of aluminum/stainless steel bimetallic composites through a combination of additive manufacturing and vacuum-assisted melt infiltration casting. *J Manuf Process.* **2021**;69:320–330. doi: [10.1016/j.jmapro.2021.07.047](https://doi.org/10.1016/j.jmapro.2021.07.047)
- [134] Bryla J. The influence of the mex manufacturing parameters on the tensile elastic response of printed elements. *Rapid Prototyp J.* **2021**;27(1):187–196. doi: [10.1108/RPJ-02-2020-0034](https://doi.org/10.1108/RPJ-02-2020-0034)
- [135] Fayazfar H, Salarian M, Rogalsky A, et al. A critical review of powder-based additive manufacturing of ferrous alloys: process parameters, microstructure and mechanical properties. *Mater Des.* **2018**;144:98–128. doi: [10.1016/j.matdes.2018.02.018](https://doi.org/10.1016/j.matdes.2018.02.018)
- [136] Gor M, Soni H, Wankhede V, et al. A critical review on effect of process parameters on mechanical and microstructural properties of powder-bed fusion additive manufacturing of SS316L. *Materials.* **2021**;14(21):6527. doi: [10.3390/ma14216527](https://doi.org/10.3390/ma14216527)
- [137] Oliveira JP, LaLonde A, Ma J. Processing parameters in laser powder bed fusion metal additive manufacturing. *Mater Des.* **2020**;193:108762. doi: [10.1016/j.matdes.2020.108762](https://doi.org/10.1016/j.matdes.2020.108762)
- [138] Temiz A. The effects of process parameters on tensile characteristics and printing time for masked stereolithography components, analyzed using the response surface method. *J Mater Eng Perform.* **2024**;33(18):9356–9365. doi: [10.1007/s11665-023-08617-7](https://doi.org/10.1007/s11665-023-08617-7)
- [139] Reddy BY, Siddhartha M, Reddy PSR, et al. Influence of process parameters on sheet lamination method-based 3D printing: a review. In: E3S Web of Conferences. Vol. 430. EDP Sciences; 2023. p. 01251.
- [140] Tulpan I, Snir Y, Halevi S, et al. Effect of the lattice structure on the interface zone and the final properties of novel printcast Ti64-AlSi9Cu3 interpenetrating phase composites. *Addit Manuf.* **2024**;79:103902.
- [141] Galati M, Minetola P, Rizza G. Surface roughness characterization and analysis of the electron beam melting

- (EBM) process. *Materials*. **2019**;12(13):2211. doi: [10.3390/ma12132211](https://doi.org/10.3390/ma12132211)
- [142] Maurya P, Kota N, Gibmeier J, et al. Review on study of internal load transfer in metal matrix composites using diffraction techniques. *Mater Sci Eng A*. **2022**;840:142973. doi: [10.1016/j.msea.2022.142973](https://doi.org/10.1016/j.msea.2022.142973)
- [143] Roy S, Albrecht P, Weidenmann KA. Influence of ceramic freeze-casting temperature on the anisotropic thermal expansion behavior of corresponding interpenetrating metal/ceramic composites. *J Mater Eng Perform*. **2023**;32(19):8795–8806. doi: [10.1007/s11665-022-07769-2](https://doi.org/10.1007/s11665-022-07769-2)
- [144] Schukraft J, Roßdeutscher J, Siegmund F, et al. Thermal expansion behavior and elevated temperature elastic properties of an interpenetrating metal/ceramic composite. *Thermochim Acta*. **2022**;715:179298. doi: [10.1016/j.tca.2022.179298](https://doi.org/10.1016/j.tca.2022.179298)
- [145] Shen Y-L. Thermal expansion of metal–ceramic composites: a three-dimensional analysis. *Mater Sci Eng A*. **1998**;252(2):269–275. doi: [10.1016/S0921-5093\(98\)00698-4](https://doi.org/10.1016/S0921-5093(98)00698-4)
- [146] Roy S, Nagel A, Weidenmann KA. Anisotropic thermal expansion behavior of an interpenetrating metal/ceramic composite. *Thermochim Acta*. **2020**;684:178488. doi: [10.1016/j.tca.2019.178488](https://doi.org/10.1016/j.tca.2019.178488)
- [147] Zhang F, Qian K, Lu P, et al. Quasi-static compressive fracture behavior of three-period minimum surface $\text{Al}_2\text{O}_3/\text{Al}$ composites fabricated by stereolithography. *J Mater Res Technol*. **2024**;30:4950–4960. doi: [10.1016/j.jmrt.2024.04.224](https://doi.org/10.1016/j.jmrt.2024.04.224)
- [148] Bauer J, Sala-Casanovas M, Amiri M, et al. Nanoarchitected metal/ceramic interpenetrating phase composites. *Sci Adv*. **2022**;8(33):eabo3080. doi: [10.1126/sciadv.abo3080](https://doi.org/10.1126/sciadv.abo3080)
- [149] Rahmani R, Antonov M, Kollo L, et al. Mechanical behavior of $\text{Ti}_6\text{Al}_4\text{V}$ scaffolds filled with CaSiO_3 for implant applications. *Appl Sci*. **2019**;9(18):3844. doi: [10.3390/app9183844](https://doi.org/10.3390/app9183844)
- [150] Lu J, Zhang X, Li S, et al. Quasi-static compressive and cyclic dynamic impact performances of vat photopolymerization 3D printed Al_2O_3 triply periodic minimal surface scaffolds and $\text{Al}_2\text{O}_3/\text{Al}$ hybrid structures: effects of cell size. *J Alloys Compd*. **2023**;969:172445. doi: [10.1016/j.jallcom.2023.172445](https://doi.org/10.1016/j.jallcom.2023.172445)
- [151] Santos S, Matos C, Duarte I, et al. Effect of TPMS reinforcement on the mechanical properties of aluminium–alumina interpenetrating phase composites. *Prog Addit Manuf*. **2024**;10:1187–1199. doi: [10.1007/s40964-024-00698-7](https://doi.org/10.1007/s40964-024-00698-7)
- [152] Matos C, Santos S, Duarte I, Olhero SM, Miranda G. Insights into morphology and mechanical properties of architected interpenetrating aluminum-alumina composites. *J Compos Mater*. **2024**;58(24):2623–2637. doi: [10.1177/00219983241271054](https://doi.org/10.1177/00219983241271054)
- [153] Rivera J, Yang Q, Bustillos CG, et al. Mechanical responses of architected boron carbide-aluminum lattice composites fabricated via reactive metallic infiltration of hierarchical pore structures. *Mater Today Commun*. **2023**;37:107550. doi: [10.1016/j.mtcomm.2023.107550](https://doi.org/10.1016/j.mtcomm.2023.107550)
- [154] Liu Q, Hong L, Dong X, et al. 3D printed hierarchical interpenetrating phase composites with multi-scale mechanical energy absorption mechanisms. *Composites Part B*. **2023**;264:110911. doi: [10.1016/j.compositesb.2023.110911](https://doi.org/10.1016/j.compositesb.2023.110911)
- [155] Wen Y, Xiong Y, Zhang F, et al. Enhancement of mechanical properties of metamaterial absorber based on selective laser sintering and infiltration techniques. *Compos Commun*. **2020**;21:100373. doi: [10.1016/j.coco.2020.100373](https://doi.org/10.1016/j.coco.2020.100373)
- [156] Singh A, Karathanasopoulos N. Mechanics of ceramic-epoxy interpenetrating phase composites engineered with TPMS and spinodal topologies. *Compos Sci Technol*. **2024**;253:110632. doi: [10.1016/j.compscitech.2024.110632](https://doi.org/10.1016/j.compscitech.2024.110632)
- [157] Singh A, Karathanasopoulos N. Static and dynamic damping mechanical performance of architected metal-epoxy interpenetrating phase composites. *Composites Part A*. **2024**;182:108171. doi: [10.1016/j.compositesa.2024.108171](https://doi.org/10.1016/j.compositesa.2024.108171)
- [158] Song W, Mu K, Feng G, et al. Mechanical properties of 3d printed interpenetrating phase composites with TPMS architectures. *Thin-Walled Struct*. **2023**;193:111210. doi: [10.1016/j.tws.2023.111210](https://doi.org/10.1016/j.tws.2023.111210)
- [159] Wang K, Wang H, Zhang J, et al. Mechanical behavior of interpenetrating phase composite structures based on triply periodic minimal surface lattices. *Compos Struct*. **2024**;337:118044. doi: [10.1016/j.compstruct.2024.118044](https://doi.org/10.1016/j.compstruct.2024.118044)
- [160] Li G, Li Y, Yang L, et al. Strong hybrid cellular/lamellar ceramic/polymer composites via emulsification freeze casting. *J Am Ceram Soc*. **2025**;108(2):e20164. doi: [10.1111/jace.v108.2](https://doi.org/10.1111/jace.v108.2)
- [161] Tang T, Ahire B, Li X. Scalable multi-material additive manufacturing of bioinspired polymeric material with metallic structures via electrically assisted stereolithography. *J Manuf Sci Eng*. **2023**;145(1):011004. doi: [10.1115/1.4055793](https://doi.org/10.1115/1.4055793)
- [162] Wang X, Li Z, Guo X, et al. Superior damage tolerance observed in interpenetrating phase composites composed of aperiodic lattice structures. *Extreme Mech Lett*. **2024**;72:102227. doi: [10.1016/j.eml.2024.102227](https://doi.org/10.1016/j.eml.2024.102227)
- [163] Tu S, Ren X, He J, et al. Stress-strain curves of metallic materials and post-necking strain hardening characterization: a review. *Fatigue Fract Eng Mater Struct*. **2020**;43(1):3–19. doi: [10.1111/ffe.v43.1](https://doi.org/10.1111/ffe.v43.1)
- [164] Faridmehr I, Osman MH, Adnan AB, et al. Correlation between engineering stress-strain and true stress-strain curve. *Am J Civ Eng Archit*. **2014**;2(1):53–59.
- [165] Newnham RE. Properties of materials: anisotropy, symmetry, structure. Oxford, UK: Oxford University Press; 2005.
- [166] Skrzypek JJ, Ganczarski AW (Eds.), *Mechanics of anisotropic materials, engineering materials*. Cham, Switzerland: Springer; 2015.
- [167] Gorodtsov VA, Lisovenko DS. Elastic model of isotropic powder materials with different tensile and compressive moduli. *J Eng Phys Thermophys*. **2009**;82(1):123–130.
- [168] Odom EM, Adams DF. An investigation of the isotropy of epoxy polymers. *J Mater Res*. **1992**;7(12):3352–3358. doi: [10.1557/JMR.1992.3352](https://doi.org/10.1557/JMR.1992.3352)



- [169] Siebert L, Jeschek T, Zeller-Plumhoff B, Roszak R, Hrynevich A, Dalton PD, Wunner FM. Mechanical interactions in interpenetrating composites. In: Tiginyanu I, Cojocaru P, Ursaki V, editors. 5th International Conference on Nanotechnologies and Biomedical Engineering. Cham: Springer; 2022. p. 579–586. (IFMBE Proceedings; vol. 93). doi: [10.1007/978-3-030-92328-0_74](https://doi.org/10.1007/978-3-030-92328-0_74)
- [170] Yao B, Zhou Z, Duan L. Anisotropic compressive properties and energy absorption of metal–resin interpenetrating phase composites. *J Mater Res.* 2018;33(17):2463–2476. doi: [10.1557/jmr.2018.158](https://doi.org/10.1557/jmr.2018.158)
- [171] Roylance D. Stress-strain curves. Cambridge: Massachusetts Institute of Technology study.
- [172] Kostic S, Milojkovic J, Simunovic G, et al. Uncertainty in the determination of elastic modulus by tensile testing. *Eng Sci Technol Int J.* 2022;25:100998.
- [173] Hauert A, Rossoll A, Mortensen A. Young's modulus of ceramic particle reinforced aluminium: measurement by the impulse excitation technique and confrontation with analytical models. *Composites Part A.* 2009;40(4):524–529. doi: [10.1016/j.compositesa.2009.02.001](https://doi.org/10.1016/j.compositesa.2009.02.001)
- [174] Roy S, Gebert J-M, Stasiuk G, et al. Complete determination of elastic moduli of interpenetrating metal/ceramic composites using ultrasonic techniques and micromechanical modelling. *Mater Sci Eng A.* 2011;528(28):8226–8235. doi: [10.1016/j.msea.2011.07.029](https://doi.org/10.1016/j.msea.2011.07.029)
- [175] Roy S, Stoll O, Weidenmann KA, et al. Analysis of the elastic properties of an interpenetrating AlSi12-Al₂O₃ composite using ultrasound phase spectroscopy. *Compos Sci Technol.* 2011;71(7):962–968. doi: [10.1016/j.compscitech.2011.02.014](https://doi.org/10.1016/j.compscitech.2011.02.014)
- [176] Wanner A. Elastic modulus measurements of extremely porous ceramic materials by ultrasonic phase spectroscopy. *Mater Sci Eng A.* 1998;248(1–2):35–43. doi: [10.1016/S0921-5093\(98\)00524-3](https://doi.org/10.1016/S0921-5093(98)00524-3)
- [177] International Organization for Standardization. ISO 13314:2011. Mechanical testing of metals—Ductility testing—Compression test for porous and cellular metals. Geneva: ISO; 2011.
- [178] Prasad G, Goerdeler M, Gottstein G. Work hardening model based on multiple dislocation densities. *Mater Sci Eng A.* 2005;400:231–233. doi: [10.1016/j.msea.2005.03.061](https://doi.org/10.1016/j.msea.2005.03.061)
- [179] Taya M, Chou T-W. Prediction of the stress–strain curve of a short-fibre reinforced thermoplastic. *J Mater Sci.* 1982;17:2801–2808. doi: [10.1007/BF00644654](https://doi.org/10.1007/BF00644654)
- [180] Li S, Xu M, Yan S, et al. On the objectivity of the nonlinear along-fibre shear stress–strain relationship for unidirectionally fibre-reinforced composites. *J Eng Math.* 2021;127:1–13. doi: [10.1007/s10665-021-10089-4](https://doi.org/10.1007/s10665-021-10089-4)
- [181] Jhaver R, Tippur H. Processing, compression response and finite element modeling of syntactic foam based interpenetrating phase composite (IPC). *Mater Sci Eng A.* 2009;499(1–2):507–517. doi: [10.1016/j.msea.2008.09.042](https://doi.org/10.1016/j.msea.2008.09.042)
- [182] Ashby MF, Medalist RM. The mechanical properties of cellular solids. *Metall Trans A.* 1983;14(9):1755–1769. doi: [10.1007/BF02645546](https://doi.org/10.1007/BF02645546)
- [183] Sha Y, Jiani L, Haoyu C, et al. Design and strengthening mechanisms in hierarchical architected materials processed using additive manufacturing. *Int J Mech Sci.* 2018;149:150–163. doi: [10.1016/j.ijmecsci.2018.09.038](https://doi.org/10.1016/j.ijmecsci.2018.09.038)
- [184] Choy SY, Sun C-N, Leong KF, et al. Compressive properties of functionally graded lattice structures manufactured by selective laser melting. *Mater Des.* 2017;131:112–120. doi: [10.1016/j.matdes.2017.06.006](https://doi.org/10.1016/j.matdes.2017.06.006)
- [185] Sun Z, Guo Y, Shim V. Characterisation and modeling of additively-manufactured polymeric hybrid lattice structures for energy absorption. *Int J Mech Sci.* 2021;191:106101. doi: [10.1016/j.ijmecsci.2020.106101](https://doi.org/10.1016/j.ijmecsci.2020.106101)
- [186] Liu J, Guo K, Sun J, et al. Compressive behavior and vibration-damping properties of porous Ti-6Al-4V alloy manufactured by laser powder bed fusion. *J Manuf Process.* 2021;66:1–10. doi: [10.1016/j.jmapro.2021.03.060](https://doi.org/10.1016/j.jmapro.2021.03.060)
- [187] Chernyshikhin S, Zhevnenko S, Suvorova V, et al. Mechanical and thermal properties of gyroid-based WCU composites produced via laser powder bed fusion assisted by infiltration. *Int J Refract Met Hard Mater.* 2024;122:106699. doi: [10.1016/j.ijrmhm.2024.106699](https://doi.org/10.1016/j.ijrmhm.2024.106699)
- [188] Han Y, Li S, Cao Y, et al. Mechanical properties of CU-W interpenetrating-phase composites with different w-skeleton. *Metals.* 2022;12(6):903. doi: [10.3390/met202060903](https://doi.org/10.3390/met202060903)
- [189] Okulov IV, Wilmers J, Joo S-H, et al. Anomalous compliance of interpenetrating-phase composite of Ti and Mg synthesized by liquid metal dealloying. *Scr Mater.* 2021;194:113660. doi: [10.1016/j.scriptamat.2020.113660](https://doi.org/10.1016/j.scriptamat.2020.113660)
- [190] Yan X, Sugio K, Choi Y, et al. Microstructure and mechanical properties of Al/AlN interpenetrating phase composites with different preform porosity. *Mater Chem Phys.* 2024;315:129029. doi: [10.1016/j.matchemphys.2024.129029](https://doi.org/10.1016/j.matchemphys.2024.129029)
- [191] Chen X, Wu Y, Liu H, et al. Mechanical performance of PEEK-Ti6Al4V interpenetrating phase composites fabricated by powder bed fusion and vacuum infiltration targeting large and load-bearing implants. *Mater Des.* 2022;215:110531. doi: [10.1016/j.matdes.2022.110531](https://doi.org/10.1016/j.matdes.2022.110531)
- [192] Leary M. Design of lattice and zero-mean curvature structures. In: Leary M, editor. Design for Additive Manufacturing. Cambridge (MA): Elsevier; 2020. p. 123–163.
- [193] Li X, Kim M, Zhai W. Ceramic microlattice and epoxy interpenetrating phase composites with simultaneous high specific strength and specific energy absorption. *Mater Des.* 2022;223:111206. doi: [10.1016/j.matdes.2022.111206](https://doi.org/10.1016/j.matdes.2022.111206)
- [194] Tancogne-Dejean T, Diamantopoulou M, Gorji MB, et al. 3D plate-lattices: an emerging class of low-density metamat material exhibiting optimal isotropic stiffness. *Adv Mater.* 2018;30(45):1803334. doi: [10.1002/adma.v30.45](https://doi.org/10.1002/adma.v30.45)
- [195] Zhang X, Li Q, Holesinger TG, et al. Ultrastrong, stiff, and lightweight carbon-nanotube fibers. *Adv Mater.* 2007;19(23):4198–4201. doi: [10.1002/adma.v19.23](https://doi.org/10.1002/adma.v19.23)
- [196] Kawachi T, Kimoto N, Tsunemi Y. Stiffness increase and weight reduction based on stiffness evaluation techniques. *Nippon Steel Tech Rep.* 2019;122:93–98.
- [197] Al-Shammary MA, Abdullah SE. Stiffness to weight ratio of various mechanical and thermal loaded hyper

- composite plate structures. IOP Conf Ser Mater Sci Eng. **2018**;433:012051. doi: [10.1088/1757-899X/433/1/012051](https://doi.org/10.1088/1757-899X/433/1/012051)
- [198] Patton R, Li F, Edwards M. Causes of weight reduction effects of material substitution on constant stiffness components. *Thin-Walled Struct.* **2004**;42(4):613–637. doi: [10.1016/j.tws.2003.08.001](https://doi.org/10.1016/j.tws.2003.08.001)
- [199] Yang J-S, Ma L, Schmidt R, et al. Hybrid lightweight composite pyramidal truss sandwich panels with high damping and stiffness efficiency. *Compos Struct.* **2016**;148:85–96. doi: [10.1016/j.compstruct.2016.03.056](https://doi.org/10.1016/j.compstruct.2016.03.056)
- [200] Gibson LJ, Ashby MF. *Cellular Solids: Structure and Properties*. 2nd ed. Cambridge: Cambridge University Press; **1999**. Chapter 3, Material Properties; p. 52–92.
- [201] Ashby MF. Overview no. 80: on the engineering properties of materials. *Acta Metall.* **1989**;37(5):1273–1293. doi: [10.1016/0001-6160\(89\)90158-2](https://doi.org/10.1016/0001-6160(89)90158-2)
- [202] Ashby MF, Gibson LJ. Cellular solids: structure and properties. Cambridge, UK: Press Syndicate of the University of Cambridge; **1997**. p. 175–231.
- [203] Ashby MF. Materials selection in mechanical design. 5th ed. Oxford: Butterworth-Heinemann; **2016**.
- [204] Abdel-Malek K, Paul B. Criteria for the design of manipulator arms for a high stiffness-to-weight ratio. *J Manuf Syst.* **1998**;17(3):209–220. doi: [10.1016/S0278-6125\(98\)80062-9](https://doi.org/10.1016/S0278-6125(98)80062-9)
- [205] Zhang Z, Keppens V, Liaw PK, et al. Elastic properties of Zr-based bulk metallic glasses studied by resonant ultrasound spectroscopy. *J Mater Res.* **2007**;22(2):364–367. doi: [10.1557/jmr.2007.0040](https://doi.org/10.1557/jmr.2007.0040)
- [206] Bauer J, Meza LR, Schaedler TA, et al. Nanolattices: an emerging class of mechanical metamaterials. *Adv Mater.* **2017**;29(40):1701850. doi: [10.1002/adma.v29.40](https://doi.org/10.1002/adma.v29.40)
- [207] Schaedler TA, Jacobsen AJ, Torrents A, et al. Ultralight metallic microlattices. *Science.* **2011**;334(6058):962–965. doi: [10.1126/science.1211649](https://doi.org/10.1126/science.1211649)
- [208] Crook C, Bauer J, Guell Izard A, et al. Plate-nanolattices at the theoretical limit of stiffness and strength. *Nat Commun.* **2020**;11(1):1579. doi: [10.1038/s41467-020-15434-2](https://doi.org/10.1038/s41467-020-15434-2)
- [209] Karathanasopoulos N, Dos Reis F. Extending the elastic and plastic design space of metamaterials through load-specific, multiscale inner material architectures. *Int J Mech Sci.* **2020**;175:105523. doi: [10.1016/j.ijmecsci.2020.105523](https://doi.org/10.1016/j.ijmecsci.2020.105523)
- [210] Zhang Z, Fu X, Sheng Q, et al. Experimental and numerical simulations on the mechanical characteristics of soil–rock mixture in uniaxial compression. *Appl Sci.* **2024**;14(22):10485. doi: [10.3390/app142210485](https://doi.org/10.3390/app142210485)
- [211] Idris MI, Vodenitcharova T, Hoffman M. Mechanical behaviour and energy absorption of closed-cell aluminium foam panels in uniaxial compression. *Mater Sci Eng A.* **2009**;517(1–2):37–45. doi: [10.1016/j.msea.2009.03.067](https://doi.org/10.1016/j.msea.2009.03.067)
- [212] Saeidi K, Gao X, Zhong Y, et al. Transformation of austenite to duplex austenite-ferrite assembly in annealed 316L stainless steel fabricated by selective laser melting. *J Alloys Compd.* **2019**;766:1–14.
- [213] Laskowska D, Szatkiewicz T, Bałasz B, et al. Mechanical properties and energy absorption abilities of diamond TPMS cylindrical structures fabricated by selective laser melting with 316l stainless steel. *Materials.* **2023**;16(8):3196. doi: [10.3390/ma16083196](https://doi.org/10.3390/ma16083196)
- [214] Ravichander BB, Jagdale SH, Kumar G. Surface morphology, compressive behavior, and energy absorption of graded triply periodic minimal surface 316l steel cellular structures fabricated by laser powder bed fusion. *Materials.* **2022**;15(23):8294. doi: [10.3390/ma15238294](https://doi.org/10.3390/ma15238294)
- [215] Wang L, Shi Y, Zhang Y, et al. High tensile ductility and strength in a gradient structured Zr. *Mater Lett.* **2018**;228:500–503. doi: [10.1016/j.matlet.2018.06.084](https://doi.org/10.1016/j.matlet.2018.06.084)
- [216] Easton M, Song WQ, Abbott T. A comparison of the deformation of magnesium alloys with aluminium and steel in tension, bending and buckling. *Mater Des.* **2006**;27(10):935–946. doi: [10.1016/j.matdes.2005.03.005](https://doi.org/10.1016/j.matdes.2005.03.005)
- [217] Zhang C, Zhang H, Sun Q, et al. Mechanical properties of $Zr_{41.2}Ti_{13.8}Ni_{10}Cu_{12.5}Be_{22.5}$ bulk metallic glass with different geometric confinements. *Results Phys.* **2018**;8:1–6. doi: [10.1016/j.rinp.2017.09.059](https://doi.org/10.1016/j.rinp.2017.09.059)
- [218] Mahuof AA, Ateya AM. Energy absorption mechanisms in thin-walled tubes made of traditional materials: 304 stainless steel and 5005-H32 aluminum alloys. In: AIP Conference Proceedings, Vol. 3009. AIP Publishing; **2024**.
- [219] Zhang X, Wang R, Li X, et al. Effects of aluminum foam filling on compressive strength and energy absorption of sandwich panels. *Metals.* **2020**;10(12):1670. doi: [10.3390/met10121691](https://doi.org/10.3390/met10121691)
- [220] Zhang X, Wang R, Li X, et al. Energy absorption performance of open-cell aluminum foam and its application in landing buffer system. *J Mater Eng Perform.* **2021**;30:6132–6145. doi: [10.1007/s11665-021-05823-z](https://doi.org/10.1007/s11665-021-05823-z)
- [221] Patel N, Mittal G, Agrawal M, et al. Aluminum foam production, properties, and applications: a review. *Int J Metalcast.* **2024**;18:2181–2198. doi: [10.1007/s40962-023-01174-8](https://doi.org/10.1007/s40962-023-01174-8)
- [222] Bernhart G, Davies P. Comparison of the impact resistance of carbon/epoxy and carbon/peek composite laminates. *Appl Compos Mater.* **2009**;16:153–164.
- [223] Balaganesan G, Kumar VA, Khan VC, et al. Energy-absorbing capacity of polyurethane/sic/glass-epoxy laminates under impact loading. *J Eng Mater Technol.* **2017**;139(2):021008. doi: [10.1115/1.4035617](https://doi.org/10.1115/1.4035617)
- [224] Wegner L, Gibson L. The fracture toughness behaviour of interpenetrating phase composites. *Int J Mech Sci.* **2001**;43(8):1771–1791. doi: [10.1016/S0020-7403\(01\)00016-9](https://doi.org/10.1016/S0020-7403(01)00016-9)
- [225] Karimi HR, Khedri E, Mousavi A, et al. Mode I/II cracking behavior of additively manufactured interpenetrating phase composites (IPC), an experimental and theoretical study. *Theor Appl Fract Mech.* **2024**;131:104396. doi: [10.1016/j.tafmec.2024.104396](https://doi.org/10.1016/j.tafmec.2024.104396)
- [226] Fu J, Haeri H, Labuz JF, et al. Determination of mode I fracture toughness of brittle materials with a new method. *Acta Mech Sin.* **2024**;40(2):423236. doi: [10.1007/s10409-023-23236-x](https://doi.org/10.1007/s10409-023-23236-x)
- [227] Xiao L, Mu K, Liu S, et al. Experimental study on the fracture behavior of 3D printed interpenetrating phase composites with triply periodic minimal surface architectures. *Thin-Walled Struct.* **2025**;208:112847. doi: [10.1016/j.tws.2024.112847](https://doi.org/10.1016/j.tws.2024.112847)

- [228] Li T, Chen Y, Wang L. Enhanced fracture toughness in architected interpenetrating phase composites by 3D printing. *Compos Sci Technol.* **2018**;167:251–259. doi: [10.1016/j.compscitech.2018.08.009](https://doi.org/10.1016/j.compscitech.2018.08.009)
- [229] Zhang M, Yu Q, Liu Z, et al. Compressive properties of 3-D printed Mg–NiTi interpenetrating-phase composite: effects of strain rate and temperature. *Composites Part B.* **2021**;215:108783. doi: [10.1016/j.compositesb.2021.108783](https://doi.org/10.1016/j.compositesb.2021.108783)
- [230] Fan Z, Zhang B, Liu Y, et al. Interpenetrating phase composite foam based on porous aluminum skeleton for high energy absorption. *Polym Test.* **2021**;93:106917. doi: [10.1016/j.polymertesting.2020.106917](https://doi.org/10.1016/j.polymertesting.2020.106917)
- [231] Raj R, Prajapati MJ, Tsai J-T, et al. Design and additive manufacturing of novel hybrid lattice metamaterial for enhanced energy absorption and structural stability. *Mater Des.* **2024**;245:113268. doi: [10.1016/j.matdes.2024.113268](https://doi.org/10.1016/j.matdes.2024.113268)
- [232] Franco-Martínez F, Grasl C, Kornfellner E, et al. Hybrid design and prototyping of metamaterials and metasurfaces. *Virtual Phys Prototyping.* **2022**;17(4):1031–1046. doi: [10.1080/17452759.2022.2101009](https://doi.org/10.1080/17452759.2022.2101009)
- [233] Everton SK, Hirsch M, Stravroulakis P, et al. Review of in-situ process monitoring and in-situ metrology for metal additive manufacturing. *Mater Des.* **2016**;95:431–445. doi: [10.1016/j.matdes.2016.01.099](https://doi.org/10.1016/j.matdes.2016.01.099)
- [234] Mosallanejad MH, Niroumand B, Aversa A, et al. In-situ alloying in laser-based additive manufacturing processes: a critical review. *J Alloys Compd.* **2021**;872:159567. doi: [10.1016/j.jallcom.2021.159567](https://doi.org/10.1016/j.jallcom.2021.159567)
- [235] Schmitz T, Corson G, Olvera D, et al. A framework for hybrid manufacturing cost minimization and preform design. *CIRP Ann.* **2023**;72(1):373–376. doi: [10.1016/j.cirp.2023.04.051](https://doi.org/10.1016/j.cirp.2023.04.051)
- [236] Karathanasopoulos N, Singh A, Hadjidoukas P. Machine learning-based modelling, feature importance and Shapley additive explanations analysis of variable-stiffness composite beam structures. *Structures.* **2024**;62:106206. doi: [10.1016/j.istruc.2024.106206](https://doi.org/10.1016/j.istruc.2024.106206)
- [237] Sheini Dashtgoli D, Taghizadeh S, Macconi L, et al. Comparative analysis of machine learning models for predicting the mechanical behavior of bio-based cellular composite sandwich structures. *Materials.* **2024**;17(14):3493. doi: [10.3390/ma17143493](https://doi.org/10.3390/ma17143493)
- [238] Deng C, Wang Y, Qin C, et al. Self-directed online machine learning for topology optimization. *Nat Commun.* **2022**;13(1):388. doi: [10.1038/s41467-021-27713-7](https://doi.org/10.1038/s41467-021-27713-7)
- [239] Xu X, Zhang Y. A gaussian process regression machine learning model for forecasting retail property prices with Bayesian optimizations and cross-validation. *Decis Anal J.* **2023**;8:100267. doi: [10.1016/j.dajour.2023.100267](https://doi.org/10.1016/j.dajour.2023.100267)
- [240] Shin S, Shin D, Kang N. Topology optimization via machine learning and deep learning: a review. *J Comput Des Eng.* **2023**;10(4):1736–1766.
- [241] Li Z, Zeng K, Guo Z, et al. All-in-one: an interwoven dual-phase strategy for acousto-mechanical multifunctionality in microlattice metamaterials. *Adv Funct Mater.* **2024**;34(5):2420207. doi: [10.1002/adfm.202420207](https://doi.org/10.1002/adfm.202420207)
- [242] Li Z, Wang X, Zeng K, et al. Unprecedented mechanical wave energy absorption observed in multifunctional bioinspired architected metamaterials. *NPG Asia Mater.* **2024**;16(1):45. doi: [10.1038/s41427-024-00565-5](https://doi.org/10.1038/s41427-024-00565-5)
- [243] Farman M, Surendra , Prajesh R, et al. All-polydimethylsiloxane-based highly flexible and stable capacitive pressure sensors with engineered interfaces for conformable electronic skin. *ACS Appl Mater Interfaces.* **2023**;15(28):34195–34205. doi: [10.1021/acsami.3c04227](https://doi.org/10.1021/acsami.3c04227)